University Hospital of Ulm

Internal Medicine II

Medical Director Prof. Dr. med. Wolfgang Rottbauer

Dental MRI for Identification and Quantification of Initial Caries Lesions

Dissertation to Obtain the

Doctoral Degree of Human Biology

of the Faculty of Medicine

University of Ulm

presented by

Anna-Katinka Bracher

from Ulm

2016

Acting Dean: **Prof. Dr. rer. nat. Thomas Wirth**

1st Reviewer: **Prof. Dr. rer. nat. Volker Rasche**

2nd Reviewer: **Prof. Dr. med. dent. Margrit-Ann Geibel**

Day of Graduation: 12. February 2016

Dedicated to

Felix

Contents

List of Abbreviations ix

List of Symbols xi

1. Introduction 1

2. Theory 4

2.1. Magnetic Resonance Imaging 4

2.1.1. NMR Experiment 5

2.1.2. Signal Localization 14

2.1.3. MRI Pulse Sequences 20

2.1.4. Contrast Mechanisms 23

2.2. Signal Processing 28

2.2.1. Modulation Transfer Function (MTF) and Point Spread Function (PSF) 28

2.2.2. Fourier Transformation for Centrosymmetric Functions 31

2.3. Magnetic Field Distortions 33

2.3.1. Time-Independent Field Variations – Off-resonances 33

2.3.2. Time-dependent Field Variations – Eddy Currents 35

2.4. Dental Tissues and Caries Lesions 37

3. Methodological Issues **41**

3.1. MRI System 41

3.2. Reconstruction Framework 44

3.3. Simulation Framework 47

3.4. Signal-to-Noise Ratio 49

4. Dedicated MRI Techniques for Ultra-Short Echo Time Imaging **53**

4.1. Sequence Requirements 53

4.2. Imaging Sequences 55

4.2.1. SPRITE 55

4.2.2. ZTE 57

4.2.3. UTE 60

4.2.4. SWIFT 62

4.3. Discussion 64

5. Ultra-Short Echo Time Imaging for Identification of Initial Caries Lesions **67**

5.1. Imaging Sequence 67

5.1.1. RF Pulse 69

5.1.2. Signal Encoding 72

5.1.3. Signal Spoiling 78

5.1.4. Impact of Signal Imperfections 79

5.2. Signal Corrections 92

5.2.1. Trajectory Mapping 93

5.2.2. Image Reconstruction using the Trajectory Mapping Approach 107

5.3. UTE for Identification of Caries Lesions 113

5.4. UTE-T_2^* for Quantification of Caries Lesions 119

5.5. Discussion 126

6. Center-Acquisition at Partial Ramp Imaging (CAPRI) 129

6.1. Imaging Sequence 129

6.1.1. Impact of T_2^* Relaxation During Acquisition 137

6.1.2. Impact of Off-Resonances During Acquisition 147

6.1.3. SNR Considerations 156

6.2. Automatic Delay Correction using CAPRI 157

6.3. CAPRI for Identification of Caries Lesions 168

6.4. Discussion 172

7. Conclusion 178

8. Bibliography 183

A. CAPRI PSF 189

A.1. PSF Related to T_2^* Relaxation During Acquisition 190

A.1.1. Pure Flattop Sampling 190

A.1.2. Pure Ramp Sampling 194

A.2. PSF Related to Off-Center Frequency 199

A.2.1. Pure Flattop Sampling 199

A.2.2. Pure Ramp Sampling 203

List of Figures

1. Spin precession in the presence of B_0 6
2. Spin excitation 9
3. Spin-lattice (T_1) relaxation 12
4. Spin-spin (T_2) relaxation 13
5. Slice selection 16
6. K-space encoding 19
7. Spin-echo 22
8. Spin-echo (SE) imaging sequence 22
9. Gradient echo (GE) imaging sequence 24
10. PD contrast 25
11. T_1 contrast 27
12. T_2 contrast 27
13. Representation of the tooth in different image modalities 39
14. MRI hardware. 43
15. Flowchart of the TIGER-RECON reconstruction software. 45
16. Single–Point Imaging (SPI / SPRITE): pulse sequence schemes 57
17. Zero Echo Time (ZTE): pulse sequence scheme 59
18. Ultra-short Echo Time (UTE): pulse sequence scheme 61
19. SWeep Imaging with Fourier Transform (SWIFT): pulse sequence scheme . 63

20. UTE: imaging sequence 68
21. UTE: RF excitation optimization 71
22. UTE: sampling distribution 75
23. UTE: kooshball sampling scheme 75
24. UTE: sampling density compensation 77
25. UTE: impact of gradient delay on sampling grid 80
26. UTE: impact of gradient delay on reconstructed images 81
27. UTE: impact of eddy currencts on the gradient and the trajectory 83
28. UTE: PSF related to T2* relaxation during acquisition 88
29. UTE: impact of T2* relaxation during acquisition on reconstructed images 88
30. UTE: PSF related to zero order off-resonances during acquisition 91
31. UTE: impact of offset frequency during acquisition on recosntructed images 92
32. Trajectory mapping: sequence 94
33. Trajectory mapping: base line drift correction 97
34. Trajectory mapping: phase evolution for different slice locations 98
35. Trajectory mapping: phase evolution for different slice thicknesses 99
36. Trajectory mapping: impact of a zero order off-resonance on the slice distance102
37. Trajectory mapping: impact of biased slice locations caused by a zero order off-resonance on the trajectory 102
38. Trajectory mapping: impact of a first order off-resonance on the slice distance104
39. Trajectory mapping: impact of biased slice locations caused by a first order off-resonance on the trajectory 106
40. Trajectory mapping: image reconstruction using the mapped trajectory . . 108
41. Trajectory mapping: compensation for deviation in k-space area. 109
42. Trajectory mapping: gradient waveform model to characterize non-idealities112
43. Trajectory mapping: image reconstruction using modeled trajectory 113
44. Dental UTE: MRI and x-ray images for different classes of caries lesions . . 117

45. Dental UTE: definition of the measured lesion extensions in MRI 118
46. Dental UTE: in-situ evaluation of caries lesion extend 119
47. UTE-T_2^*: sequence timing for T_2^* mapping 121
48. UTE-T_2^*: T_2^* relaxation depending on the progress of caries lesions 122
49. UTE-T_2^*: in-vivo data of T_2^* relaxation in dental tissues 125
50. CAPRI: imaging sequence 130
51. CAPRI: gradient amplifier output 134
52. CAPRI: minimal echo time related to the CAPRI factor 135
53. CAPRI: time as a function of k-space for constant and ramp-only gradient . 136
54. CAPRI: MTF and PSF for flattop and ramp sampling (T_2^* decay) 139
55. CAPRI: PSF amplitude and FWHM for flattop and ramp sampling (T_2^* decay) 140
56. CAPRI: MTF and PSF for CAPRI sampling (T_2^* decay) 141
57. CAPRI: PSF amplitude and FWHM for CAPRI sampling (T_2^* decay) 142
58. CAPRI: effect of increased echo time on the initial signal amplitude 144
59. CAPRI: effect of T_2^* decay on image quality 145
60. CAPRI: profiles of T_2^* affected objects 146
61. CAPRI: MTF and PSF for flattop and ramp sampling (B_0 off-resonance) . . 149
62. CAPRI: PSF amplitude, FWHM and FWTM for flattop and ramp sampling (B_0 off-resonance) 150
63. CAPRI: PSF amplitude, FWHM and FWTM for CAPRI sampling (B_0 off-resonance) 151
64. CAPRI: effect of off-resonances on image quality 153
65. CAPRI: profiles of off-resonance affected objects 154
66. CAPRI: off-resonance measurements 155
67. CAPRI: signal-to-noise consideration 157
68. CAPRI delay correction: imaging sequence considering gradient delay . . . 159

69. CAPRI delay correction: impact of linear off-resonances on echo position . 160
70. CAPRI delay correction: restrictions of delay calcualtion 164
71. CAPRI delay correction: determined delays along a kooshball interleave . 166
72. CAPRI delay correction: reconstructed images using calculated delays . . . 167
73. dental CAPRI: MRI and x-ray images of approximal caries lesions 170
74. dental CAPRI: MRI images for different CAPRI factors 171

List of Tables

1. UTE: sequence parameters for dental scans 115
2. UTE: sequence parameters for T_2^* mapping 124
3. UTE: T_2^* values for dentin and caries lesions 124
4. CAPRI: sequence parameters for dental scans 169
5. CAPRI: caries lesion extend and CNR 170

List of Abbreviations

CAPRI . . . . . Center-Acquisition at Partial Ramp Imaging

CNR . . . . . Contrast-to-Noise Ratio

EC . . . . . Eddy Current

ECC . . . . . Eddy Current Compensation

FID . . . . . Free Induction Decay

FOV . . . . . Field Of View

FT . . . . . Fourier Transform

FWHM . . . . . Full Width Half Maximum

FWTM . . . . . Full Width Tenth Maximum

GCD . . . . . Gradient Channel Delay

GE . . . . . Gradient Echo

GPE . . . . . Gradient waveform Pre-Emphasis

MRI . . . . . Magnetic Resonance Imaging

MTF . . . . . Mean Transfer Function

NMR . . . . . Nuclear Magnetic Resonance

PSF . . . . . Point Spread Function

RF . . . . . Radio Frequency

RX . . . . . Receive mode

SE . . . . . Spin Echo

SNR . . . . . Signal-to-Noise Ratio

TSE . . . . . Turbo Spin Echo

TX . . . . . Transmit mode

UTE . . . . . Ultra-short Echo Time

XR . . . . . Radiography

List of Symbols

The major symbols used throughout this thesis are defined in this list. Additional symbols are defined in the individual sections.

$\boldsymbol{B_0}$ . . . . . Main magnetic field strength $[T]$

$\boldsymbol{B_1}$ . . . . . Radiofrequency magentic field $[\mu T]$

$\boldsymbol{BW_{read}}$ . . . . . Receiver bandwidth [Hz]

$\boldsymbol{D_r}$ . . . . . Distance of selected slice from isocenter (equal to z_{sl}) $[mm]$

$\boldsymbol{f_0}$ . . . . . Larmor frequency $[Hz]$

$\boldsymbol{f_{off}}$ . . . . . Off-resonance frequency $[Hz]$

$\boldsymbol{f_{sl}}$ . . . . . RF pulse center frequency $[Hz]$

$\boldsymbol{\Delta f}$ . . . . . RF pulse bandwidth $[Hz]$

$\boldsymbol{f_{CAPRI}}$ . . . . . CAPRI factor

$\boldsymbol{G}$ . . . . . Generic magnetic field gradient $[mT/m]$

$\boldsymbol{G_{max}}$ . . . . . Maximum gradient amplitude $[mT/m]$

$\boldsymbol{G_{RO}}$ . . . . . Readout magnetic field gradient $[mT/m]$

$\boldsymbol{G_{PRE}}$ . . . . . Prephasing magentic field gradient $[mT/m]$

$\boldsymbol{G_{sl}}$ . . . . . Slice selection magnetic field gradient $[mT/m]$

$\boldsymbol{k}$ . . . . . k-space variable, spatial frequency $[1/mm]$

$\boldsymbol{\Delta k}$ . . . . . k-space interval (determines FOV) $[1/mm]$

$\boldsymbol{k_{max}}$ . . . . . Maximum spatial frequency (determines spatial resolution) $[1/mm]$

$\boldsymbol{k_{slope}}$ . . . . . k-space covered during ramp up of the gradient $[1/mm]$

$\boldsymbol{M_0}$ . . . . . Equilibrium magnetization

$\boldsymbol{M_{\parallel}}$ . . . . . Longitudinal magnetization: M_z

$\boldsymbol{M_{\perp}}$ . . . . . Transverse magnetization: $M_{xy} = M_x + \mathrm{i}M_y$

$\boldsymbol{r}$ . . . . . Spatial variable $[mm]$

$\boldsymbol{S_{max}}$ . . . . . Maximum system slewrate $[mT/ms]$

$\boldsymbol{S_{RO}}$ . . . . . Slewrate of the readout gradient $[mT/ms]$

$\boldsymbol{T_1}$ . . . . . Spin-lattice relaxation time $[ms]$

$\boldsymbol{T_2}$ . . . . . Spin-spin relaxation time $[\mu s$ or $ms]$

$\boldsymbol{T_2^*}$ . . . . . Effective spin-spin relaxation time $[\mu s$ or $ms]$

TE . . . . . Echo time $[ms]$

TR . . . . . Repetition time $[ms]$

$\boldsymbol{t}$ . . . . . Time $[ms]$

$\boldsymbol{\Delta t}$ . . . . . Sampling interval $[\mu s]$

$\boldsymbol{T_{ACQ}}$ . . . . . Acquisition duration $[ms]$

$\boldsymbol{T_{slope}}$ . . . . . Slope duration $[ms]$

$\boldsymbol{T_D}$ . . . . . Gradient delay $[\mu s]$

$\boldsymbol{\Delta z}$ . . . . . Slice thickness $[mm]$

$\boldsymbol{\Delta r}$ . . . . . Image resolution (3D: Δx,Δy,Δz) $[mm]$

$\boldsymbol{\alpha}$ . . . . . Flip angle $[^\circ]$

$\boldsymbol{\gamma}$ . . . . . Gyromagnetic ratio $[rad/s/sT]$

$\boldsymbol{\omega_0}$ . . . . . Larmor frequency $[rad/s]$

1. Introduction

Magnetic resonance imaging (MRI) is a powerful imaging modality to visualize soft tissues and organs of the human body non-invasively and without any use of ionizing radiation. MRI is based on the phenomena of nuclear magnetic resonance (NMR) which was discovered in the 1950s by Bloch [4] and Purcell [35,36]. The fundamental inventions regarding imaging applications based on NMR took place in the 1970s and underwent an enormous development during the last decades. The excellent soft tissue contrast and the ability of contrast modifications, as well as the ability of creating high spatial resolution images and three-dimensional images, make MRI to the nowadays leading modality for diagnostic imaging of numerous common diseases.

Although MRI is used in various medical fields, the primary clinical applications of MRI in dentistry are the assessment of extracranial tumours and the diagnosis of internal derangement of the temporomandibular joint. Besides the current clinical applications of MRI in dentistry there also exist investigations of the applicability of MRI in implant planning, in the assessment of dental and periapical anatomy and pathology, in the localization of impacted teeth, and the indirect imaging of caries lesions. Its limited capability in assessing mineralized tissues and the rising artefacts caused by dental fillings have so far restricted the wide application of MRI in diagnosis of caries disease. Over the last decade a diversity of dedicated imaging sequences were introduced to detect the signal of mineralised tissues and enable the direct visualization of dental tissues and initial caries lesions. Therefore

MRI has attracted more and more attention in the field of research in caries imaging over the last few years.

In this thesis it is shown that dedicated MRI sequences have the feasibility to visualize even initial caries lesions and estimate the process of caries. The visualization of caries lesions is based on the change of mineralized structure over time. The signal intensity as well as the signal decay over time are affected differently at different stages of caries progress. While conventional classification of caries lesion progression is restricted due to still difficult delineation of the mineralized tissues of the teeth, the process of caries lesion can be assessed using MRI as a quantitative tool, where the tissue specific signal behaviour is observed over time. The ability of MRI to visualize the anatomy in three dimensions facilitates the localization of the lesion and the detection of caries lesions located under fillings and crowns (secondary or hidden caries) which are often superimposed in conventional radiography projection images. Therefore the introduced imaging sequences can serve as an alternative technique to the used ionizing radiation based imaging techniques, which are the gold standard in nowadays dental investigations.

The thesis is structured as follows: Chapter 2 provides the physical background of MR imaging as well as the theoretical fundamentals of caries process and imaging based diagnosis. The general methodological aspects used throughout this thesis are presented in chapter 3. Chapter 4 introduces different kind of MRI pulse sequences which enable much shorter echo times (TEs) than conventional MRI sequences and thus can be considered for the visualization of mineralized tissues. The general advantages and disadvantages of these techniques are analyses and discussed. A detailed understanding of the selected MR imaging sequence and the application of MRI in dental analysis and quantification of caries lesions is given in chapter 5. The impact of system imperfections on image quality and appropriate correction methods are also discussed. In chapter 6 a new imaging sequence called CAPRI is introduced, which enables automatic correction of timing inconsistencies

during acquisition. The impact of tissue dependent signal modifications on image quality as well as the application of CAPRI for dental MR imaging are described and evaluated. Finally the general conclusion and clinical implications are provided in chapter 7.

2. Theory

This chapter gives a brief overview of the basic concepts of magnetic resonance imaging – including signal excitation, signal encoding and contrast behaviour – of the system performance, of the origin of magnetic field distortions, and at last of the composition of the teeth, the process of caries disease and the related representation in different image modalities.

2.1. Magnetic Resonance Imaging

Magnetic Resonance Imaging (MRI) is based on the interaction of nuclear spins with an external magnetic field $\vec{B}_0$, which forces the spin to precess around the field direction. So the nuclear magnetic resonance (NMR) is the basic principle for this imaging modality. In human imaging the dominant nucleus is the proton in hydrogen atoms. In this chapter the basics of MR signal formation, encoding and detection, as well as the mechanism of contrast defining nucleus properties are introduced. This section is based on the textbooks of Haacke et al. [19], Bernstein. et al. [3] and Rinck et al. [40] unless otherwise stated. Please refer to these textbooks for more comprehensive information.

2.1.1. NMR Experiment

The effect of nuclear magnetic resonance (NMR) can be observed for nuclei with non-zero spin quantum number I. For a nucleus with non-zero quantum number the rotating mass of the nucleus results in an angular momentum J (spin) and the rotating electrical charge results in a magnetic moment μ.

In the presence of an external magnetic field $\vec{B}_{ext}$ the magnetic moments align with its direction and start to precesses at a frequency ω_0 around its axes (fig. 1). It is assumed that the external static Magnetic field $\vec{B}_{ext}$ appears only in z-direction and has a field strength of B_0:

$$\vec{B}_{ext} = \vec{B_0} = B_0\hat{z}, \tag{2.1}$$

with the unit vector $\hat{z} = (0,0,1)^T$. The precession frequency of the nucleus is then given by the Larmor equation:

$$\omega_0 = \gamma B_0 \tag{2.2}$$

where γ is the gyromagnetic ratio, which describes the ratio of its magnetic dipole moment to its angular momentum.

Clinical magnetic resonance imaging is usually based on the nucleus of the hydrogen atom ^1H ($\mathrm{I} = 1/2$) which possess a single positive charged proton. The spin quantum number of the proton determines the number of discrete energy levels (Zeeman effect) which exist for the given nucleus in the presence of an external magnetic field B_0. Therefore two possible energy levels exist which correspond to the principal quantized states of the proton and describe the orientation of the magnetic moment related to the main magnetic field. In the classical picture the nucleus will either align parallel (spin-up) or anti-parallel (spin-

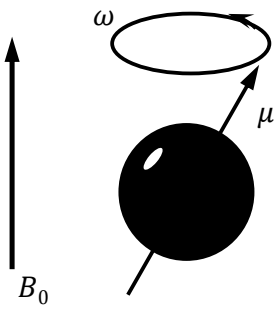

Figure 1.: Precession of a nucleus with non-zero spin in the presence of an external magnetic field B_0. The nucleus possesses a magnetic moment μ and precesses at frequency ω_0.

down) to the main magnetic field. The distribution of the number of spins in the high energy level N_{high} and low energy state N_{low} are given by:

$$\frac{N_{high}}{N_{low}} = e^{\Delta E/k_B T}$$

where $\Delta E = \hbar\gamma B_0$ describes the difference between the two energy levels, k_B is the Boltzmann constant and T the absolute temperature in Kelvin. Since the difference in energy levels in NMR is proportional to the field strength of the main magnetic field, the difference of the number of spins for the two energy levels increases with increasing B_0.

For hydrogen atoms, the gyromagnetic ratio γ result in $\gamma_H = 267.51310^{6\,rad/sT}$ or as often quoted $\frac{\gamma}{2\pi} = 42.6\,^{MHz/T}$ in units of hertz.

2.1.1.1. Magnetization Vector

To understand the mechanism of signal behaviour in magnetic resonance imaging the macroscopic model is used for further considerations instead of the microscopic model. Therefore a set of spins within a volume V is treated as one entity where the external

field can be estimated as constant over the volume element (voxel). This set of spins will further be referred as 'isochromat'. The resulting macroscopic magnetic moment – the magnetization vector $\vec{M}$ – results as the sum over all microscopic magnetic moments in the volume [19]:

$$\vec{M} = \frac{1}{V}\sum_{i=1}^{N}\vec{\mu}_i \tag{2.3}$$

The motion of the magnetization vector can be achieved by the sum over the motion of the individual spins, neglecting the proton interactions with the surroundings:

$$\frac{1}{V}\sum_{i=1}^{N}\frac{\mathrm{d}\vec{\mu}_i}{\mathrm{d}t} = \frac{\gamma}{V}\sum_{i=1}^{N}\vec{\mu}_i \times B_0\hat{z} \tag{2.4}$$

$$\frac{\mathrm{d}\vec{M}}{\mathrm{d}t} = \gamma\vec{M} \times B_0\hat{z} \tag{2.5}$$

To simplify the description of RF excitation and the relaxation mechanisms, the system is no longer described from a stationary point of view like in the laboratory reference frame, which is defined with respect to the magnet. Therefore a rotating frame coordinate system is introduced for further description of the system, which rotates at the Larmor frequency. For further analysis of the net-magnetization $\vec{M}$ and the differential equation the magnetization is separated in two components $\vec{M}_{\parallel}$ – parallel to the static magnetic field – and $\vec{M}_{\perp}$ – perpendicular to $\vec{B}_0$.

Since the external static magnetic field exists per definition only in z-direction, the parallel – or also called longitudinal magnetization – consists only of the z component of the magnetization vector and experiences no motion due to spin precession.

$$\vec{M}_{\parallel} = M_z\hat{z} \tag{2.6}$$

$$\frac{\mathrm{d}\vec{M}_{\parallel}}{\mathrm{d}t} = 0 \tag{2.7}$$

The perpendicular magnetization describes the magnetization in the transverse plane of the main magnetic field and is composed of the magnetization components in x and y direction:

$$\vec{M}_{\perp} = M_x\hat{x} + M_y\hat{y} \tag{2.8}$$

$$\frac{\mathrm{d}\vec{M}_{\perp}}{\mathrm{d}t} = \gamma\vec{M}_{\perp} \times \vec{B}_0 = \gamma B_0(M_y\hat{x} - M_x\hat{y}), \tag{2.9}$$

with the unit vectors $\hat{x} = (1,0,0)^T$ and $\hat{y} = (0,1,0)^T$.

As seen from the equations above the longitudinal and transversal components of the magnetization can be treated independently.

2.1.1.2. Signal Excitation

In equilibrium the phase of the protons are randomly distributed and the net-magnetization $\vec{M}$ is aligned with the main magnetic field. Since the absolute value of the net-magnetization is very small compared to B_0 it is virtually impossible to measure it. To detect the net-magnetization a magnetic component has to be generated in the xy-plane and a coil is used measuring only the transversal component of the magnetization vector, which is not superposed by B_0. Therefore a radiofrequency (RF) wave pulse with a frequency equal to the Larmor frequency of the nuclei is used, which then creates a time varying magnetic field $\vec{B}_1$ in the transversal plane. The energy transferred by the RF pulse promotes spins to exchange from low to high energy state and increases the magnitude of the net-magnetization. Additionally, resonance phenomena lead to a synchronization of the precessing spins and therefore there exists no loss of magnetization due to phase incoherence.

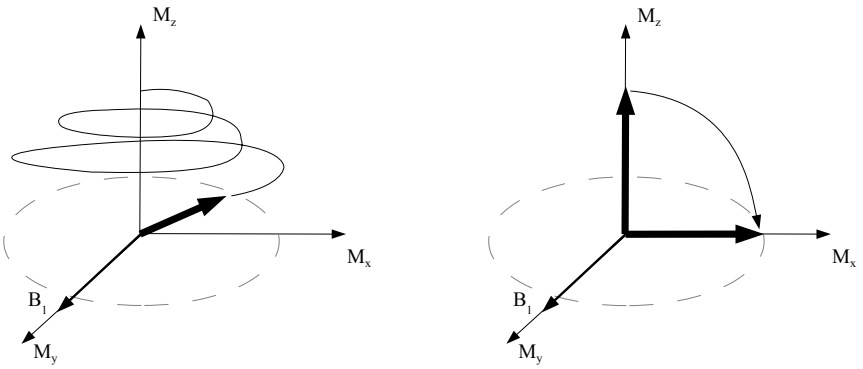

(a) **(b)**

Figure 2.: Behaviour of the macroscopic magnetization during RF excitation (a) within a fixed coordinate system and (b) within a coordinate sytstem rotating at the Larmor frequency ω_0.

During excitation the spins start to precess about the additionally applied field B_1 which leads to an additional rotation orthogonal to z-axis (fig. 2a). To simplify the description of RF excitation, the MR signal is described in the rotating frame coordinate system which rotates at the Larmor frequency. Therefore the only field the spins experience is those generated by the RF pulse and the spin isochromats and therefore $\vec{M}$ rotates no longer about the z-axes. The excitation can than be described by a simple rotation into the transversal plane (fig. 2b).

The rotation angle α is defined as the excitation or flip angle. Special excitation pulses are the 90°-pulse where the complete longitudinal magnetization is transferred into the transversal plane and the 180°-pulse which completely inverts the magnetization.

At the end of the RF excitation a part of the macroscopic magnetization vector is transferred into the transversal plane. The quantity of transferred magnetization depends on the applied excitation angle.

In the laboratory frame the transversal component $\vec{M}_\perp$ rotates around the axes of the external field. This causes an induction of voltage in the receive coil and the MR signal can be detected. The initial amplitude M_0 of the signal is determined by the portion of the magnetization vector that has been tipped onto the transversal plane. The induced signal is called Free Induction Decay (FID) of the system and is strongly influenced by the reduction of the transversal magnetization. After the excitation the spins instantaneously start to return to their equilibrium state. The change in time of the magnetization vector, regarding relaxation of magnetization due to interaction of the proton spins with the environment, can be described by the following equations:

$$\frac{\mathrm{d}M_z}{\mathrm{d}t} = \frac{(M_0 - M_z)}{T_1}, \tag{2.10}$$

$$\frac{\mathrm{d}M_x}{\mathrm{d}t} = \omega_0 M_y - \frac{M_x}{T_2}, \tag{2.11}$$

$$\frac{\mathrm{d}M_y}{\mathrm{d}t} = -\omega_0 M_x - \frac{M_y}{T_2}, \tag{2.12}$$

where T_1 describes the time dependent return of longitudinal magnetization to its equilibrium state and T_2 the loss in phase coherence over time of the transversal magnetization. The processes of signal relaxation are described in the following section.

2.1.1.3. Relaxation

The generated magnetization M starts to decay rapidly after the RF excitation. The relaxation of the magnetization M is caused by two concurrent processes: the spin-lattice interaction and the interaction among the spins themselves.

Spin-Lattice Interaction

The spin-lattice – also called longitudinal, or T_1 – relaxation describes the realignment of the macroscopic magnetization with the external magnetic field $\vec{B}_0$ and therefore the return of the spin system to the state of thermal equilibrium. After the excitation of the spin system the nuclei are transferring energy into the surrounding environment (lattice) and revert to a lower energy state, their equilibrium position. This leads to a build up of longitudinal magnetization. The temporal process of recovery of the longitudinal magnetization is illustrated in figure 3 and can be described by the equation 2.13 in case of $\alpha = 90$.

$$M_z(t) = M_0 \left(1 - e^{-\frac{t}{T_1}} \right), \tag{2.13}$$

where M_0 represents the magnetization value in equilibrium and the time constant T_1 is referred as the spin-lattice time. The value of T_1 is defined as the time that M_z takes to recover to approximately 63% of its initial value and ranges from few hundred milliseconds to seconds depending, on the structure and composition of the tissue.

Spin-Spin Interaction

The spin-spin – also called transversal or T_2 – relaxation describes the loss in transversal magnetization $\vec{M}_{xy} = M_x\hat{x} + M_y\hat{y}$ due to phase incoherence caused by the interaction between the spins. After the excitation of the spin system all spins are in-phase and the maximal possible transversal magnetization is available. The influence of local magnetic field fluctuations causes the spins to precess with slightly different frequencies and therefore causes a loss of phase coherence. Since the bulk magnetization averages over all moments in the volume the loss in phase coherence – and the resulting cancellation of

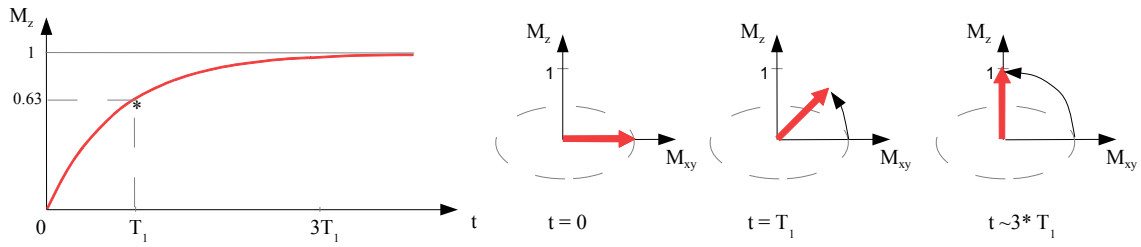

(a) **(b)**

Figure 3.: Recovery of the longitudinal magnetization caused by the return of the spin system to its equilibrium state (a) as a function of time and (b) as a illustration of the macroscopic magnetization at specified time-points.

the signal from inversely phased spins – results in a reduction of the available transversal magnetization.

Local field fluctuations are caused by the constantly moving hydrogen atoms and the related magnetic moments of the spins. Since each magnetic moment represents a small magnetic field – superimposed by the static main magnetic field – the movement of the atoms leads to a rapid fluctuation of the magnetic field changes, which are caused by adjacent spins. The fluctuating field variations result in local fluctuations of the Larmor frequencies and therefore causes the spins to precess with changing velocity. The temporal process of decay of the transversal magnetization due to local field fluctuations is described by equation 2.14 and is illustrated in figure 4, assuming the complete transfer of the longitudinal magnetization into the transversal plane ($\alpha = 90$).

$$M_{xy}(t) = M_0 \cdot e^{-\frac{t}{T_2}}, \tag{2.14}$$

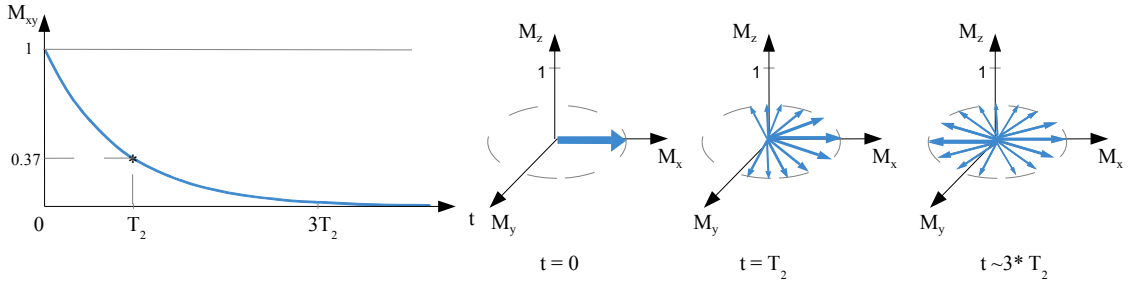

(a) **(b)**

Figure 4.: Relaxation of the transversal magnetization caused by increasing phase incoherence between the spins (a) as a function of time and (b) as a illustration of the macroscopic magnetization at specific time-points.

where M_0 represents the magnetization value in equilibrium and the time constant T_2 is referred as the spin-spin time. The value of T_2 is defined as the time that M_{xy} takes to decay to approximately 37% of its initial value and is in the order of a few microseconds to milliseconds, depending on the structure and composition of the tissue.

The static field variations depended signal decay is caused by susceptibility differences between neighbouring tissues and therefore depends on the structure and composition of the object under investigation. The susceptibility of a tissue describes its degree of magnetization in the presence of a magnetic field and thus the magnetic field changes at the boundaries of tissues with different susceptibility (e.g. air / tissue and bone / tissue). These changes of magnetic field are forcing the spins to precess at different Larmor frequencies and thus cause dephasing.

While the thermodynamic effects – which cause the random movement of the atoms (T_2) – are not reversible, the distortions introduced by static field distortions can be reversed using a spin-echo experiment (sec. 2.1.3).

The *effective* transverse relaxation time T_2^* describes the relaxation due to local magnetic field fluctuations (T_2) and static magnetic field inhomogeneities (T_2') and yield an additional exponential signal decay:

$$M_{xy}(t) = M_0 \cdot e^{-\frac{t}{T_2^*}}. \tag{2.15}$$

The relationship of T_2^* and the relaxation times T_2 and T_2' is given by the following equation:

$$\frac{1}{T_2^*} = \frac{1}{T_2} + \frac{1}{T_2'} = \frac{1}{T_2} + \frac{\gamma}{2\pi}\Delta B_0 \tag{2.16}$$

For most tissues the transversal relaxation progresses much faster than the longitudinal relaxation, so the decrease of transversal magnetization due to T_1 relaxation is negligible.

2.1.2. Signal Localization

The basic NMR experiment in the presence of a main static magnetic field B_0 causes all spins to precess with the same frequency ω_0 and therefore it is not possible to spatially assign the signal to the individual nuclei. To obtain spatial information from the received MR signal additional time variant gradient fields G are used. The superposition of these time-varying magnetic fields and the static magnetic field leads to a linear scaling of the field strength with increasing distance to the isocenter.

$$B(\vec{r}) = B_0 + \vec{G}\,\vec{r} = B_0 + G_x\hat{x} + G_y\hat{y} + G_z\hat{z}, \tag{2.17}$$

where $\vec{r} = (x,y,z)^T$ describes the coordinates of a position with its origin at the isocenter of the magnet and $\vec{G} = (G_x,G_y,G_z)^T$ describing the strength of the gradient field for the respective directions in $\left[{}^{mT}/_{m}\right]$. Note that the orientation of gradient field stays in direction of the static magnetic field and the gradients only change the strength of the magnetic field at a position $\vec{r}$. Since the precession frequency is a function of the field strength (eq. 2.2) it becomes spatially dependent in the presence of additionally applied gradients.

Slice Selection

To excite the protons, the frequency of the RF pulse has to match the resonance condition $\omega = \gamma B$. A spatially limited excitation can be obtained by applying an additional gradient field and an RF pulse with a sinc-amplitude-function which creates a rectangular frequency distribution. Assuming a slice selection in z-direction – where only the gradient in z-direction G_z is switched on – only protons are excited which fulfil the following resonance condition:

$$\omega(z) = \gamma(B_0 + G_z z) \tag{2.18}$$

Figure 5 illustrates the influence of the RF pulse and of the applied slice selection gradient on the slice selection process. The thickness Δz of the slice can be varied by the bandwidth Δf of the RF pulse or by variation of the gradient strength. Since the position z_{sl} of the slice is also depended on the gradient strength the final slice position can be changed by shifting the frequency spectrum to a center frequency f_{sl} while maintaining RF bandwidth.

The gradient enforces the protons to precess at a range of Larmor frequencies over the slice thickness and causes a dephasing of transversal magnetization. Therefore the spins possess a diverging but fixed phase along the slice profile after an unipolar gradient pulse. To compensate for the phase dispersion across the slice, a rephasing gradient pulse is applied

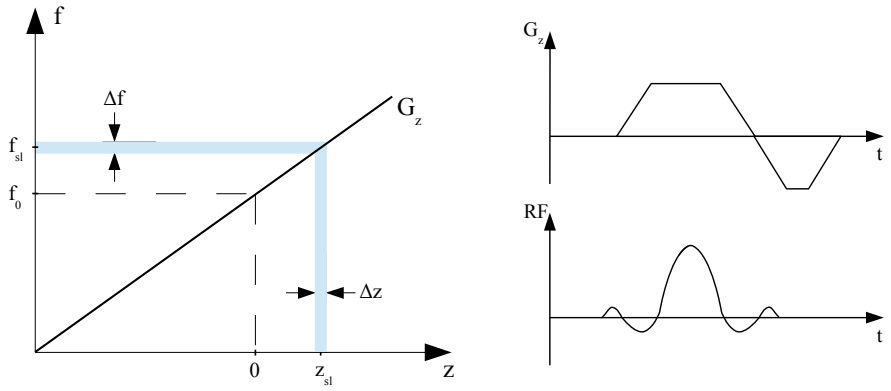

(a) **(b)**

Figure 5.: (a) Pulse sequence and (b) diagramm of a slice selection process with a gradient field G_z and an applied RF pulse with center frequency f_{sl} and bandwidth Δf.

after RF excitation to create a homogeneous transversal magnetization. The area of the slice-rephasing gradient is determined by the area of the slice selection gradient covered from the center of the RF pulse to the end of the slice selection gradient.

Spatial Encoding

Spatial encoding is based on the fact that the phase of a single spin at a given point in time depends on its precession frequency. To localize the signal within the excited volume, gradient fields are applied after RF excitation. The protons experience a change of the field strength and therefore precess at specific frequencies according to their spatial position. Therefore the phase can be described as a function of time and location. In conventional MR sequences the encoding of the signal is split up in a frequency and a phase encoding part. It is assumed that the frequency encoding is applied along the x-direction and phase encoding along the y-direction.

Frequency encoding uses superposition of a gradient field in x-direction simultaneously to the data acquisition. The spatial information is encoded in the precession frequency of the transversal magnetization. Since the signal is recorded as a function of time the frequency and phase evolutions as a function of x are obtained.

$$\omega(x,t) = \gamma(B_0 + G_x(t)x) \tag{2.19}$$

Phase encoding is performed to assign a specific initial phase to the spins depending on their location in y-direction. Therefore a gradient in y-direction is applied before the start of signal acquisition to change the precession frequencies of the spins. After the gradient is switched off, the spins continue to precess at the same frequency ω_0, with their phase depending linearly to their spatial coordinate in y-direction:

$$\phi(y) = \gamma G_y y T_{PE} \tag{2.20}$$

For signal encoding of N voxels in y-direction the phase encoding gradient is switched on for a constant time T_{PE} and the gradient strength increases stepwise by $G_y = n \cdot \Delta G_y$ between $n = {}^{-N}/_2 : {}^{N}/_2$ subsequent frequency encoding steps.

k-space formalism

The k-space is an extension of the concept of Fourier domain and therefore simply another name for the frequency domain. Instead of temporal frequencies the k-space represents the n-dimensional information of spatial frequencies. The k-space represents the matrix were the achieved MR signal is stored that is covered by multiple phase and/or frequency encoded data sets. The relation between the k-space coordinate and the applied encoding

gradient is given by:

$$\vec{k}(t) = \frac{\gamma}{2\pi} \int \vec{G}(t)\,\mathrm{d}t \tag{2.21}$$

The data at k-space center represents the low spatial frequencies and therefore the shape of huge objects and the contrast of the image. High frequencies are represented by the values in the peripheries of the k-space and determine the edge definition (sharpness) and the representation of very small objects. Therefore the resolution Δr of the image depends on the highest frequency k_{max} covered in the MR experiment:

$$\Delta r = \frac{1}{2k_{max}}. \tag{2.22}$$

Since the region of interest – commonly known as the field of view (FOV) – is determined by the number of voxels N and the desired image resolution, it depends (in the presence of a constant readout gradient) on the step-size in k-space Δk:

$$FOV = N \cdot \Delta r = \frac{N}{2k_{max}} = \frac{1}{\Delta k}. \tag{2.23}$$

Since there exist many combinations of encoding gradients there are many different ways to fill the k-space matrix. The path traced by $k(t)$ is known as the k-space trajectory.

In conventional clinical imaging the most popular k-space sampling scheme is a cartesian raster. In a cartesian sampling scheme the covering of the k-space is realized by a combination of phase encoding and frequency encoding gradients (fig. 6a). The phase encoding gradient is always applied at the same axis (here: y-axes) and leads to a coding of the

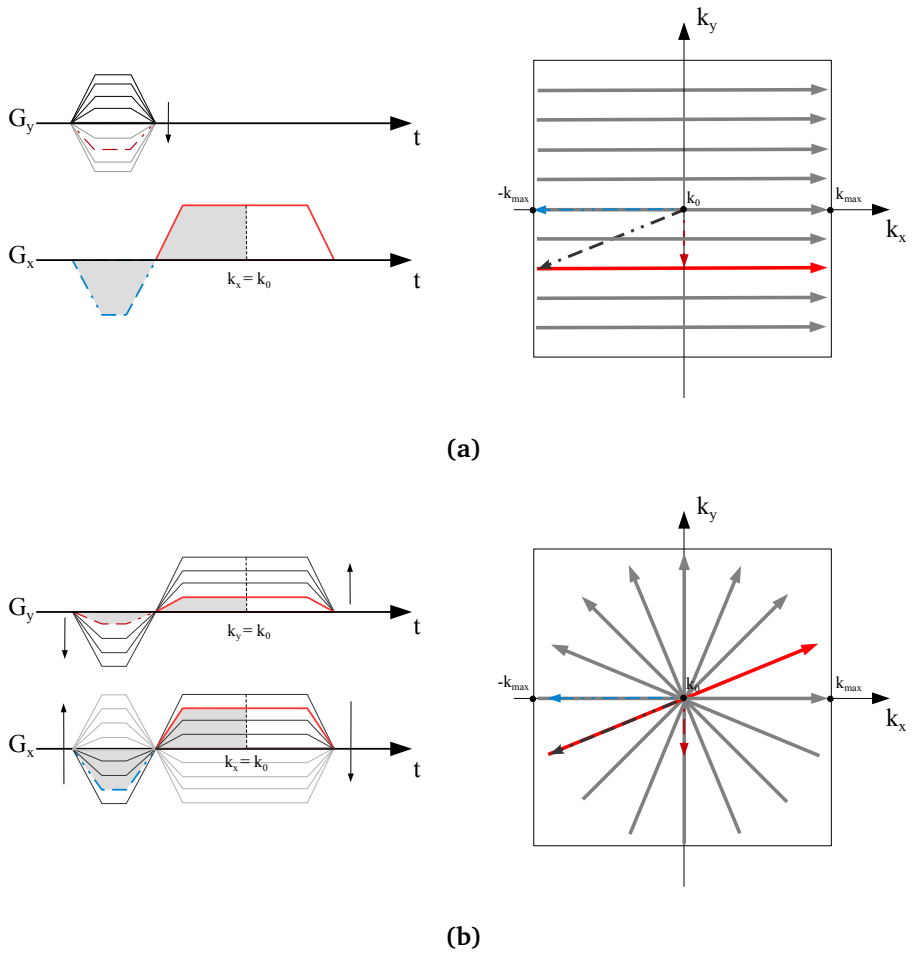

Figure 6.: Encoding gradients (left) and related k-space trajectories (right) of (a) a cartesian sampling scheme and (b) a radial projection acquisition scheme. Dashed-dotted indicates the manipulation of k-space position before start of acquisition. Red solid line represents the k-space position acquired during a single readout experiment.

k-space raster lines:

$$k_y = \frac{\gamma}{2\pi} n \, \Delta G_y \, T_{PE}. \tag{2.24}$$

The prephasing gradient in the frequency encoded direction (here: x-axes) shifts the start of the k-space trajectory to the start of the k-space line. During data acquisition (red line) the k-space is traversed from $k_x = -k_{max}$ to $k_x = -k_{max}$:

$$k_x = \frac{\gamma}{2\pi} \int G_x(t) \, \mathrm{d}t. \tag{2.25}$$

and one line in k-space along the x-axes is filled with the received MR signal. To start the next encoding step in the center of k-space, some pulse sequences return the trajectory using a rephasing gradient at the end of the readout gradient.

Another k-space trajectory can be obtained by covering the k-space in a radial manner (fig. 6b). In radial k-space sampling the encoding is realized solely by frequency encoding gradients. The prephasing gradients shift the start of the k-space trajectory to the start of the k-space line like in cartesian imaging. During the data sampling a single spoke is acquired, which crosses the k-space center. The radial encoding scheme is also known as projection acquisition (PA) since each readout line crosses the center of k-space and therefore the 1D Fourier transformation of this line represents a projection of the image.

2.1.3. MRI Pulse Sequences

Pulse sequences are used for the manipulation of the magnetization to produce a desired signal. A pulse sequence consists of a series of incidents, including RF pulses, gradient waveforms and data acquisition. Although there exist a variety of imaging sequences most

of them are based on the two basic types of sequences: the gradient echo (GE) and the spin-echo (SE) imaging sequence. The echo time TE is defined as time between the center of the excitation pulse and sampling of the k-space center. The repetition time TR is defined as the time between two subsequent RF signal excitations.

Spin-Echo

The basic spin-echo pulse sequence consists of a 90° RF pulse for signal excitation and a single 180° refocusing pulse to form a single RF SE per repetition interval. In the absence of any imaging gradients the temporal location of the echo peak depends on the timing interval between the RF pulses (fig. 7). After the excitation with a 90° pulse the complete available magnetization is flipped in the transversal plane. As described in section 2.1.1.3 static field inhomogeneities cause the spins to dephase immediately after excitation. The tissue dependent relaxation due to spin fluctuations is neglected since their behaviour is not influenced by the experiment. The refocusing pulse at $t = {}^{\mathrm{TE}}/_{2}$ rotates the spins around the x-axis and therefore causes an inversion of the rotating direction of the magnetic moments. Since the spins continue to move in the same direction they start to rephase and all magnetic moments are in phase after another $t = {}^{\mathrm{TE}}/_{2}$ period at $t = \mathrm{TE}$. In the presence of gradients applied for signal encoding, the temporal location of the echo peak is determined by the net-area of the frequency encoding gradient. The echo peak occurs when the readout gradient balances the area of the prephasing gradient. For a single echo SE sequence the time of the temporal location of the echo top caused by RF excitation and those caused by gradient area nulling are synchronised to minimization the effect of T_2^* relaxation. Therefore the center of the refocusing pulse is placed at half the distance between the center of the excitation pulse and the point of gradient balance. A typical 2D SE sequence is shown in figure 8. For both RF pulses usually spatially selective pulses are used

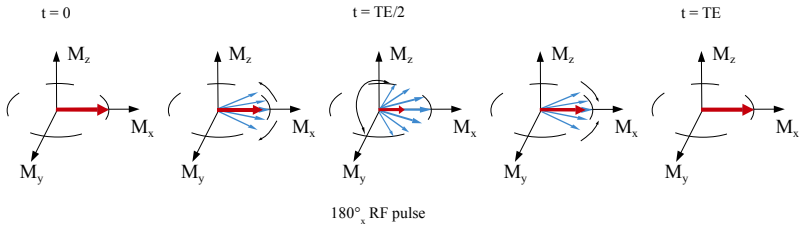

Figure 7.: The spin-echo: evolution of magnetization in the rotating frame due to field inhomogeneities (neglecting spin-spin relaxation). A 180° pulse along the x-axis is applied after a time interval $t = {}^{\mathrm{TE}}/_{2}$ which inverts the rotating direction of the magnetic moments. The magnetisation continues to evolve under the field inhomogeneities and is refocused at time point $t = \mathrm{TE}$.

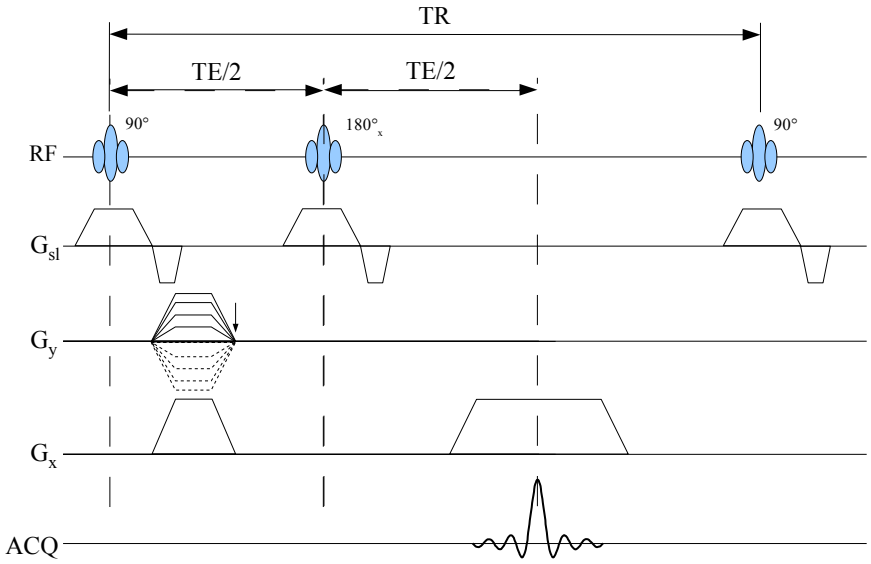

Figure 8.: The spin-echo sequence is based on a spin preparation in front of data acquisition. The temporal location of readout gradient area nulling is chosen as twice the time between the centres of the RF pulses ($^{\mathrm{TE}}/_{2}$) and therefore the time where the spin-echo occurs.

with closely matched slice excitation profiles. To obtain the k-space in two dimensions, the sequence is based on phase as well as on frequency-encoding.

Gradient Echo

The gradient echo is formed by the reversal of the frequency encoded axis. Therefore a prephasing gradient is used to cause an initial dephasing of the spin isochromates. During data acquisition the spins are rephased by applying a readout gradient with opposite sign of the gradient amplitude which leads to a subsequent encoding of the k-space. An echo is formed by reaching the k-space center in readout direction which is equal to the temporal location when the readout gradient compensates the effect of the rephasing gradient. The basic GE sequence is shown in figure 9. While the readout gradient enables the encoding of a single k-space line in x-direction, the stepped phase encoding gradient leads to subsequent sampling of the lines in y-direction. In a GE experiment the effect of phase shifts induced by static off-resonance can not be compensated for and the MR signal decays with T_2^* instead of T_2. GE sequences use no additional inversion pulse to build an echo and hence provide much shorter echo times and repetition times compared to the SE approach.

2.1.4. Contrast Mechanisms

Theory of contrast in MRI is based on the physical aspects of nucleus relaxation after the excitation by an RF pulse. Tissue dependent relaxation of the nucleus starts immediately after RF excitation and is based on the effect of return to equilibrium distribution. Most commonly MR images are weighted by T_2 (transversal relaxation), T_1 (longitudinal relaxation) and PD (proton density). The following items discuss the basic concepts of different contrast weightings.

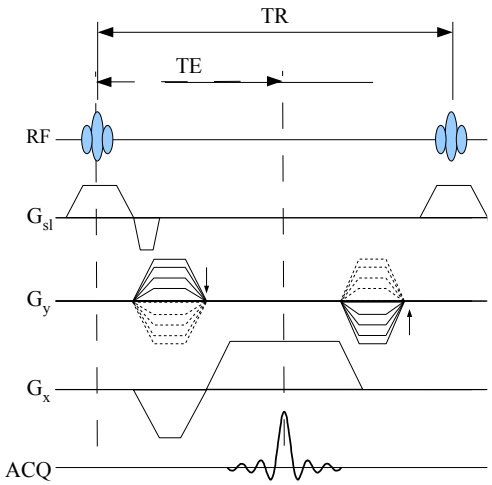

Figure 9.: Pulse sequence used for gradient echo imaging. The signal echo occurs at the temporal location when the area of the readout gradient balances the area of the prephasing gradient.

PD Contrast

The excited magnetization is proportional to the amount of protons at a specific location. Therefore regions with low proton density induce only weak signal while regions with high density induce a strong signal. Due to this fact every MR image yield a basic proton density weighting which is mainly described by a tissues content of hydrogen atoms. To achieve a nearly pure PD weighted image, the tissue dependent effect due to signal relaxation has to be minimized. To minimize the effect of T_1 relaxation a rather long repetition time is used, to ensure nearly complete recovering of the longitudinal relaxation. Since it is highly inefficient to wait for a complete return of longitudinal magnetization, the shortened repetition time leads to a slight T_1 weighting which particularly affects regions with long T_1 relaxation times. The effect of T_2 relaxation is reduced by minimizing the time between RF excitation and acquisition of k-space center. While the minimal achievable echo time in conventional MR imaging techniques is in the order of milliseconds, a slight T_2 weighting can not be avoided. Due to these timing restrictions the proton density can

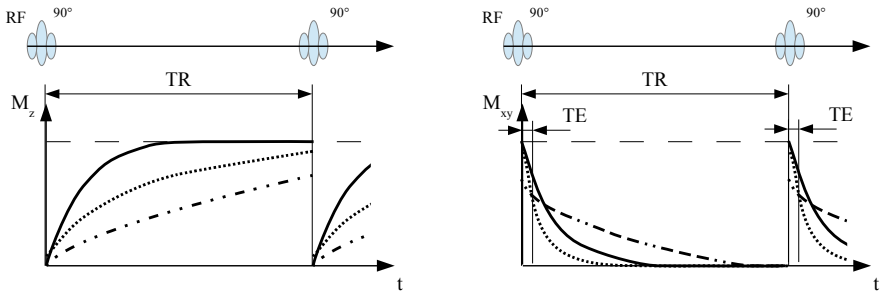

(a) **(b)**

Figure 10.: (a) Transversal and (b) longitudinal relaxation curves for a proton density weighted spin-echo pulse sequence for three different tissues (180° pulse not shown). A long sequence repetition minimizes T_1 weighting due to different amounts of recovery of the longitudinal magnetization. A short echo time is used to minimize the effect of additional T_2 weighting due to differences in transversal relaxation times.

only be approximately obtained in a PD weighted image. The signal behaviour during the imaging sequence is represented in figure 10.

T_1 Contrast

Images with T_1 related contrast can be achieved by using either spin-echo or gradient-echo sequences. To enhance the T_1 related differences between tissues both short TR and short TE times are used as imaging parameters (fig. 11). Performing fast repetitive excitations with incomplete recovery of the longitudinal relaxation, makes the acquired signal dependent on the T_1 relaxation time. Since the transversal relaxation of the signal is much faster than the recovery of the longitudinal relaxation, T_2 weighting can not be eliminated and depends on the chosen echo time. For tissues with long longitudinal relaxation times only a small amount of M_z is recovered at beginning of the next RF excitation and therefore available for next signal generation. These tissues generate only weak signal. Tissues with short T_1 values are almost completely recovered at the end of the sequence. The

high amount of available longitudinal magnetization at the next excitation pulse induces a strong signal. The modulation of image contrast for the given timing parameters results in a representation of fluids as very dark intensity values while water-based tissues appear mid grey and fat-based very bright. Due to the short repetition time, the longitudinal magnetization can not completely recover during the first excitation. To avoid a PD weighting the longitudinal magnetization has to be driven into a so called steady state, where the amount of transferred longitudinal magnetization during RF excitation corresponds to the amount of recovered M_z during the time period TR. This is done by the application of several preparation excitations before the real imaging sequence starts.

T_2 Contrast

To generate an image contrast related on the transversal magnetization both timing parameters TR and TE are long (fig. 12). Like in PD-weighted imaging, the effect of longitudinal relaxation is reduced by using long repetition times and therefore ensure nearly complete recovering of M_z, but a slight impact of T_1 weighting can not be avoided. The increased echo time leads to a progressed relaxation of the transversal magnetization and therefore yield high impact of the different T_2 relaxation times of the tissues. As mentioned in section 2.1.1.3 the effective relaxation time T_2^* is a combination of the dephasing caused by spin-spin interactions as well as caused by static field inhomogeneities. SE sequences can correct for the static inhomogeneity effects and yield a T_2 weighted image contrast. Weighting in GE sequences depends on the effective spin-spin relaxation time T_2^*. While in T_1 weighted images tissues with long T_1 values are darker than those with short T_1 values, in T_2 weighted images the tissues with long T_2 values appear brighter than those with short T_2. Therefore fluids show the highest intensity whilst water or fat based tissues are mid grey.

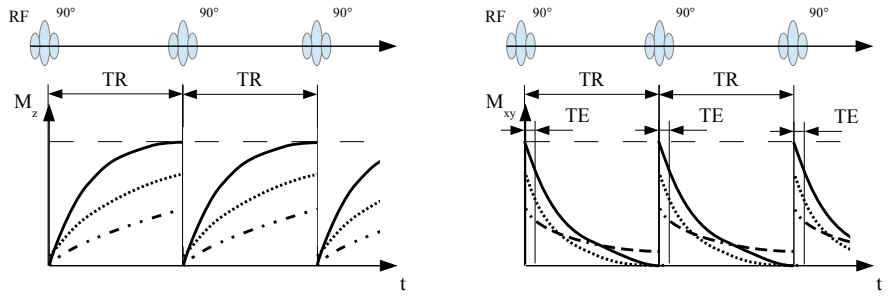

(a) **(b)**

Figure 11.: (a) Transversal and (b) longitudinal relaxation curves for a T_1 weighted spin-echo pulse sequence for three different tissues (180° pulse not shown). A short sequence repetition leads to a high impact of T_1 weighting due to different amounts of recovery of the longitudinal magnetization. A short echo time is used to minimize the effect of additional T_2 weighting due to differences in transversal relaxation times.

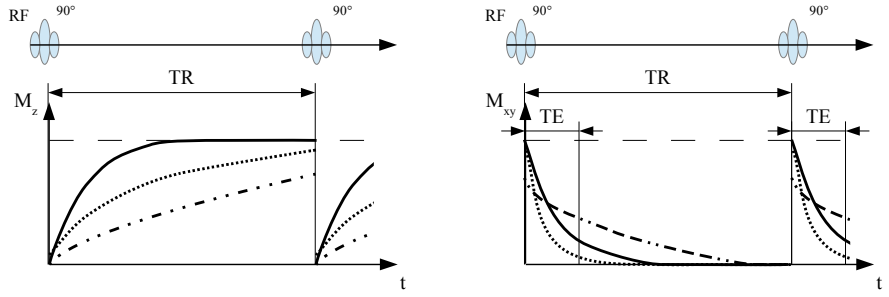

(a) **(b)**

Figure 12.: (a) Transversal and (b) longitudinal relaxation curves for a T_2 weighted spin-echo pulse sequence for three different tissues (180° pulse not shown). A long sequence repetition time minimizes the impact of T_1 weighting due to different amounts of recovered longitudinal magnetization. An increased echo time leads to a high impact of T_2 weighting due to differences in transversal relaxation times.

2.2. Signal Processing

2.2.1. Modulation Transfer Function (MTF) and Point Spread Function (PSF)

The performance of the MR system can be measured either in the frequency domain by the modulation transfer function (MTF) or in the spatial domain by the point spread function (PSF). The two functions are related by the Fourier transform:

$$MTF = F(PSF)$$
$$PSF = F^{-1}(MTF)$$

The MTF can be seen as a k-space filter which is multiplied with the k-space data. The MTF curve typically expresses normalized signal intensity as a function of spatial frequency. In the case of a complex transfer function the magnitude portion is usually referred to as MTF. The point spread function describes the system response of the MRI to a point source which is commonly known as impulse response. The image of a point source is blurred and degraded due to the systems imperfections like noise and signal decay / attenuation. According to the Fourier theorem the reconstructed image can be found by convolution of the PSF with the object.

Point Spread due to Truncation

In a non-ideal system the k-space is not sampled till infinity. This effect can be observed as the k-space signal $S(k)$ is filtered by a rect function. The collected k-space data is windowed by the filter

$$H_w(k) = \text{rect}\left(\frac{k + \frac{1}{2}\Delta k}{W}\right),$$

where Δk is the sampling interval in units of k-space distance and W the size of the window. The image of this data can be obtained by

$$\tilde{I}(x) = F^{-1}[H_w(k) \cdot S(k)]$$

$$= I(x) * h_w(x),$$

with

$$h_w(x) = W \cdot \text{sinc}(\pi W x) \cdot \exp(-i\pi\Delta k x).$$

Point Spread due to truncation and discrete sampling

To model both, the effect of truncated k-space and of discrete sampling, the MTF is a product of a rect-function describing the truncation and the sampling function.

$$H_{ws}(k) = \text{rect}\left(\frac{k + \frac{1}{2}\Delta k}{W}\right) \Delta k \sum_{p=-\infty}^{\infty} \delta(k - p\Delta k)$$

$$= \Delta k \sum_{p=-n}^{n-1} \delta(k - p\Delta k).$$

The related PSF can be calculated by the finite-Fourier inversion:

$$h_{ws}(x) = \Delta k \sum_{p=-n}^{n-1} \exp\left(-i2\pi p \Delta k x\right)$$

and the following simplified expression can be obtained [19]:

$$h_{ws}(x) = W \frac{\operatorname{sinc}(\pi W x)}{\operatorname{sinc}(\pi \Delta k x)} \cdot \exp\left(-i\pi \Delta k x\right)$$

The spatial resolution is defined as the smallest resolvable distance between two different objects. It is generally admitted that the point spread function can be used to quantify the impact of the chosen reconstruction method by the blur of the object. For discrete Fourier transformed object the spatial resolution of the windowed and sampled image can be defined in terms of area within the given FOV:

$$\begin{aligned}
\Delta x_{filter} &= \frac{1}{h_{ws,filter}(0)} \int_{-L/2}^{L/2} h_{ws,filter}(x)\,\mathrm{d}x \\
&= \frac{1}{\Delta k} \frac{H_{filter}(0)}{\sum_{p=-n}^{n-1} H_{filter}(p\Delta k)} \\
h_{ws,filter}(x) &= h_{ws}(x) * h_{filter} \\
&= \Delta k \sum_{p=-n}^{n-1} H_{filter}(p\Delta k) e^{\mathrm{i}2\pi p \Delta k x};
\end{aligned}$$

Another way to express the resolution of a given system, is to express it in terms of the width of the applied filter. This is only true if the filter has a symmetric behaviour and if its absolute maxima is at its center. It is a common convention to measure the Full Width at Half of the Maximum (FWHM), with the full width defined as twice the distance from

the center to the point where the filters amplitude has fallen to half of its maximum. A more demanding criterion follows from the use of the full width at tenth maximum.

2.2.2. Fourier Transformation for Centrosymmetric Functions

The Fourier transform for multidimensional objects is defined as a sequence of Fourier transforms for every single dimension:

$$F(u,v,w) = \int_{-\infty}^{\infty}\int_{-\infty}^{\infty}\int_{-\infty}^{\infty} f(x,y,z)e^{-i2\pi(ux+vy+wz)}\mathrm{d}x\mathrm{d}y\mathrm{d}z. \tag{2.26}$$

The variables x,y, and z may stand for some physical quantity such as time or frequency where u,v, and w represent the variables in the spatial domain.

For centrosymmetric functions the Fourier transform can be simplified to the real part (cosine) of the transformation kernel $\mathrm{e}^{i2\pi ux} = \cos(2\pi ux)+i\sin(2\pi rt)$. For an one-dimensional even function $f(x)$, the Fourier transformation can be simplified to the cosine transformation hence the integral for a sine-function over a symmetric interval around the center will be zero. The cosine transform takes no account of the function to the left of the origin and is defined only to the right of the origin:

$$F(s) = 2\int_{0}^{\infty} f(r)\cos(2\pi sr)\,\mathrm{d}x, \tag{2.27}$$

$$f(r) = 2\int_{0}^{\infty} F(s)\cos(2\pi sr)\,\mathrm{d}s. \tag{2.28}$$

The variable x therefore is replaced by the radial variable r, where $F(s)$ represents the cosine transformation of $f(x)$. The cosine transformation and the reverse transformation are identical.

A two-dimensional function $f(x,y)$ with circular symmetry can be described by a single radial variable r which replaces the independent variables x and y:

$$r^2 = x^2 + y^2$$

The related transformation $F(u,v)$ of $f(r)$ results also in a radial symmetric function $F(s)$ with $s^2 = u^2+v^2$. The Fourier transformation can than be expressed as an one-dimensional transform with Bessel function kernel:

$$F(s) = 2\pi \int_0^\infty f(r) J_0(2\pi s r)\,\mathrm{d}r \tag{2.29}$$

$$f(r) = 2\pi \int_0^\infty F(s) J_0(2\pi s r)\,\mathrm{d}s \tag{2.30}$$

The three-dimensional representation of Fourier transformation in case of symmetrical functions can be simplified by expressing the functions $f(x,y,z)$ and $F(u,v,w)$ as functions of single radial variables and the transformation for spherical symmetrical functions results to [6]:

$$F(s) = 4\pi \int_0^\infty f(r)\ \mathrm{sinc}(2\pi s r)\, r^2\,\mathrm{d}r \tag{2.31}$$

$$f(r) = 4\pi \int_0^\infty F(s)\ \mathrm{sinc}(2\pi s r) s^2 \nu \mathrm{d}s \tag{2.32}$$

The transformations for centrosymmetric functions are strictly reciprocal. For two- and three-dimensional functions the $F(s)$ are referred as the Hankel transformation of zero and first order.

2.3. Magnetic Field Distortions

Any field variation – except of the applied linear gradient – causes a deviation of the local magnetic fields from the expected one and therefore causes the spins to be spatially encoded at a wrong position. Usually one distinguishes between time-invariant and time-dependent field distortions. Time-invariant field variations can be caused by differences in material susceptibility, differences in resonance frequency (chemical shift) and main field inhomogeneities. Time variant field variations are caused by eddy currents, which are induced by the applied spatial gradient.

2.3.1. Time-Independent Field Variations – Off-resonances

Off-resonance are mainly classified into zero order off-resonance $B_{0,off}$ which are spatially invariant – like the main static field – and causing unwanted phase accumulation and first order off-resonance G_{off} which are spatial dependent like gradient fields. Since the k-space location is calculated according to the cumulative area of the applied gradient waveform (eq. 2.21) off-resonance of linear order shift the k-space trajectory relative to its ideal location. A linear gradient model can be used to express external background variations which are considered to be accurate over the entire field of view and local field variations which are considered to be accurate on the order of a voxel. The spatial dependence of static off-resonance can be described by a Taylor expansion:

$$B_{off}(\vec{r},\vec{r}_0) = B_{0,off}(\vec{r}_0) + \vec{G_{off}}(\vec{r}_0) \cdot (\vec{r} - \vec{r}_0) + \cdots , \tag{2.33}$$

where $\vec{r}_0$ describes the position of the field distortion relative to the center in the case of local field variations. These local variations may be generated by differences in internal magnetic susceptibilities of small structures (e.g. water air surface) which affect the surrounding magnetic field. Global gradient inhomogeneities, which exist over the whole FOV, can usually be corrected by using the first order shim to adjust the main magnetic field.

In the presence of global zero and first order time invariant field distortions the acquired MR signal can be rewritten as:

$$S(t) = \int_V \vec{\rho}(r)\, e^{-j2\pi\left(\vec{k}(t)+\vec{k}_{off}(t)\right)\vec{r}}\, e^{-j\Phi_{off}(t)}\, e^{-j\Phi_{off,TE}}\, \mathrm{d}^3 r, \tag{2.34}$$

with

$$\begin{aligned}
\Phi_{off}(t) &= \gamma B_{0,off}\, t \\
\vec{k}_{off}(t) &= \frac{\gamma}{2\pi}\vec{G}_{off}\, t + \vec{k}_{off,TE} \\
\Phi_{off,TE}(\vec{r}_0) &= \gamma B_{0,off}\, T_{start} \\
\vec{k}_{off,TE} &= \frac{\gamma}{2\pi}\vec{G}_{off}\, T_{start}
\end{aligned}$$

where $\Phi_{off}(t)$ is the additional phase accumulation during acquisition caused by zero order off-resonances, $k_{off}(t)$ is the accumulated k-space trajectory during acquisition resulting from linear order off-resonances, and $\Phi_{off,TE}$ and $k_{off,TE}$ are the respective accumulated phase and k-space trajectory offset at the start of acquisition T_{start}.

2.3.2. Time-dependent Field Variations – Eddy Currents

The use of pulsed magnetic field gradients in MRI result in the change of magnetic flux, which generates electrical fields according to Farraday's law. Eddy currents are build up during the time varying parts of the gradient waveform (e.g. ramp up of trapezoidal gradient) and decay during the constant parts of the gradient. According to Lenz's law the magnetic field produced by eddy currents is always opposed to the field change it was caused by (positive ramp up leads to negative eddy current). Eddy currents can be accurately modelled by exponential functions [3] and therefore can be characterized by a small number of time constants τ_n and of coefficients α_n for the initial amplitudes. The time constant describes the rate of exponential buildup of the eddy currents during ramp up and decay afterwards. The spatial dependence of time variant eddy current fields induced by an gradient pulse $G(t)$ can be described by a Taylor expansion:

$$B_{ec}(\vec{r},t) = B_{0,ec}(t) + \vec{G_{ec}}(t)\vec{r} + \cdots, \tag{2.35}$$

where $B_{0,ec}$ describes the spatial invariant zero order eddy current and G_{ec} the spatial dependent first order eddy current, also called linear eddy current. Eddy current terms of higher order are addressed by the proper shielding of the MR system and therefore are usually not considered. Assuming a linear gradient behaviour, the applied gradient waveform $G(t)$ can be considered as input and $B_{0,ec}$ and G_{ec} as outputs of a linear system. The terms of the eddy current field can then be calculated by the following equations:

$$B_{0,ec}(t) = -\frac{\mathrm{d}G_x}{\mathrm{d}t} * e_{B_{0,ec},x}(t) - \frac{\mathrm{d}G_y}{\mathrm{d}t} * e_{B_{0,ec},y}(t) - \frac{\mathrm{d}G_z}{\mathrm{d}t} * e_{B_{0,ec},z}(t), \tag{2.36}$$

and

$$G_{ec,x}(t) = -\frac{\mathrm{d}G_x}{\mathrm{d}t} * e_{G_{ec},xx}(t) - \frac{\mathrm{d}G_y}{\mathrm{d}t} * e_{G_{ec},xy}(t) - \frac{\mathrm{d}G_z}{\mathrm{d}t} * e_{G_{ec},xz}(t) \tag{2.37}$$

$$G_{ec,y}(t) = -\frac{\mathrm{d}G_x}{\mathrm{d}t} * e_{G_{ec},yx}(t) - \frac{\mathrm{d}G_y}{\mathrm{d}t} * e_{G_{ec},yy}(t) - \frac{\mathrm{d}G_z}{\mathrm{d}t} * e_{G_{ec},yz}(t)$$

$$G_{ec,z}(t) = -\frac{\mathrm{d}G_x}{\mathrm{d}t} * e_{G_{ec},zx}(t) - \frac{\mathrm{d}G_y}{\mathrm{d}t} * e_{G_{ec},zy}(t) - \frac{\mathrm{d}G_z}{\mathrm{d}t} * e_{G_{ec},zz}(t)$$

where $e_{G_{ec},xx}$, $e_{G_{ec},yy}$, and $e_{G_{ec},zz}$ are the direct linear terms representing the eddy current gradient in the direction of the applied gradient ($e_{G_{ec},xx}$: eddy current gradient in x-direction caused by applied gradient on the x-axis), while all other terms are cross terms which are much smaller than the direct terms.

The impulse responses of the system $e_{B_{0,ec}}$ and $e_{G_{ec}}$ are given by a sum of decaying exponentials:

$$e_{B_{0,ec}}(t) = \sum_n \alpha_n^{(0)} e^{-t/\tau_n^0} \tag{2.38}$$

$$e_{G_{ec}}(t) = \sum_n \alpha_n^{(L)} e^{-t/\tau_n^L} \tag{2.39}$$

In the presence of eddy currents the MR signal can be rewritten as:

$$S(t) = \int_V \vec{\rho}(r)\, e^{-j2\pi\left(\vec{k}(t)+\vec{k}_{ec}\right)\vec{r}}\, e^{-j\Phi_{ec}(t)} \mathrm{d}^3 r, \tag{2.40}$$

with

$$\Phi_{ec}(t) = \frac{\gamma}{2\pi} \int_0^t B_{0,ec}(\tau)\, \mathrm{d}\tau$$

$$\vec{k}_{ec}(t) = \gamma \int_0^t \vec{G}_{ec}(\tau)\,\mathrm{d}\tau,$$

where ρ is the proton density, Φ_{ec} the additional phase caused by zero order eddy currents and k_{ec} is the accumulated k-space trajectory resulting from linear order eddy currents.

2.4. Dental Tissues and Caries Lesions

This section describes the basic anatomy of the tooth, the process of caries formation and the related representation in the different image modalities used in this thesis. More details on development, structure, and function of oral histology can be found in [45].

The tooth consists of the hard tissues enamel, dentin, and cementum and the pulp, which is the soft tissue of the tooth. The representation of the different tissues of a tooth as well as an initial caries lesion are shown in a schematic view of tooth in figure 13b. Enamel forms the outer surface of the crown and consist of up to 96% mineral [45] and is therefore the hardest tissue in the body. Enamel is formed by ambeloblasts and has the ability to remineralize areas experiencing early demineralization (loss of minerals) and stop the caries process. The main portion of the tooth is dentin which consits of about 70% mineral hydroxylapatite, 20% organic material, and 10% water [45] and therefore is softer than enamel but still harder than bone. The whole dentin is infiltrated by microsopic canals also called dentinal tubules which contain fibers that transmit pain stimuli and nutrition throughout the tissues. Dentin is formed by odontoblasts and in contrast to enamel has the ability for further growth. The dentin which is build in the first formation of the tooth is called primary dentin. Secondary dentin is build throughout the lifetime and is formed inside the primary dentin. The third type of dentin (tertiary dentin) is also known as reparative dentin and is formed as a response to erosion and dental caries. The root of the

tooth is covered by a very thin layer, called cementum, which contains attachment fibres to anchor the tooth within the bone. Cementum consits of about 45% inorganic material and 55% organic material and water. It is therefore softer than enamel or dentin but still harder than bone. The pulp - composed of blood vessels, lymph vessels, connective tissue, nerve tissue, and cells which are able to produce dentin - is located in the center of the tooth and is completly surrounded by dentin. The cavity of the pulp is divided in the pulp chamber which is located in the crown of the tooth and the pulp canals which are located in the roots of the teeth. The function of the root is to nourishes the tooth and repair dentin. The nerve supply in the pulp transmits the signals of sensitivity and pain through a small foramen (hole) in the apex of the root.

Dental Caries is an irreversible microbial sugar-dependent infectious disease of the calcified tissues of the teeth [28]. The development starts within transparent (soft, non-mineralised) plaque film consisting of micro-organism which produces organic acids by fermentation of carohydrates. The acid production on the plaque - tooth interface results in a drop in pH at the tooths surface and causes calcium and phosphate ions to diffuse out of the enamel. This results in demineralization of the inorganic and destruction of the organic substance of the teeth.

Figure 13a shows the representation of the different tissues of a tooth and an initial caries lesion in a conventional used radiography. The contrast in a radiography is related to the amount of absorbed x-rays by the object which depends on the particular density and composition of the tissue. Since tissues with high mineral content have a much higher absorption rate compared to tissues with low mineral content, the radiography film behind tissues like enamel and dentin will be less exposed and thus look brighter than the other tissues. Since enamel has the highest mineral content of all dental tissues it has the lightest color in the x-ray, while the dentin layer is less calcified and therefore appears slightly darker. In case of decay of the tooth structures the location of demineralized tissue appears

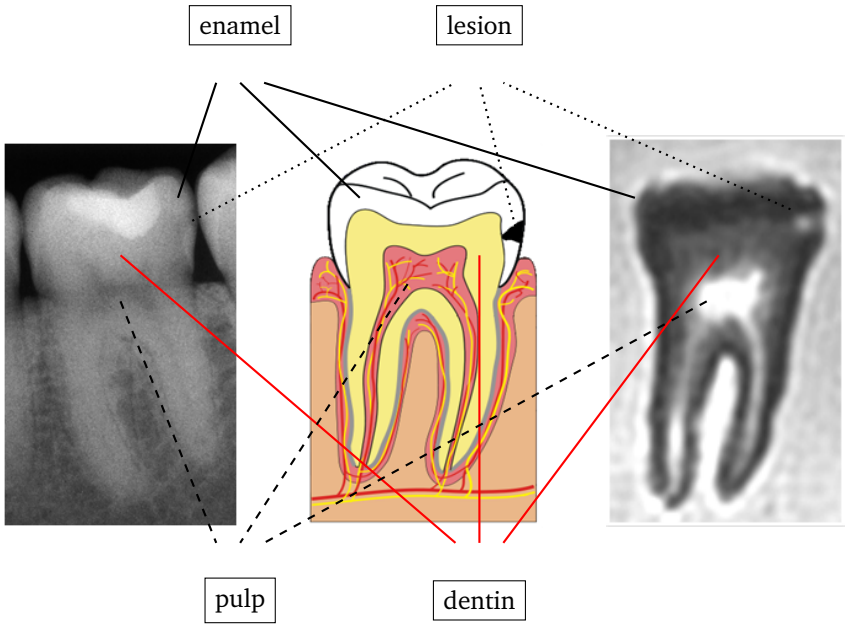

Figure 13.: The dental anatomy: (a) conventional dental radiography, (b) schematic structure, and (c) MRI image, received from dedicated UTE sequence.

as a darkened area in the x-ray images. Due to the decrease in tissue density the x-rays can penetrate that portion of the tooth more easily and the radiography in this area is exposed to a greater extent. The pulp has a very low absorption rate due to its high organic content and therefore appears dark on the radiography.

The representation of the tooth and a caries lesion in a dedicated MRI sequence is given in figure 13c. The contrast in MRI is related to the amount of free protons and the tissue specific signal decay which depends on the relaxation times (sec. 2.1.1.3). Therefore tissues with high organic content like the dental pulp appear bright and mineralized tissues with high content of bound protons and related high relaxation times appear darker. Enamel consits almost exclusively of hydroxyapatite, which is a naturally occurring mineral form of calcium apatite. Protons embedded in calcium apatite crystal structure have T_2 relax-

ation times below 150μs [5,22]. The most solid layer of the tooth therefore appears almost black in the MRI image. In dentin, with mineral content of about 70%, the water content is still low and the water is bound by the crystal lattice structure of the mineralized tissue. While the content of organic material and water is higher compared to enamel, dentin appears slightly brighter. In case of local demineralization of the tooth the decomposition of crystal lattice structure leads to a decrease in T_2 relaxation and the accumulation of acids and saliva in the caries lesion provoke an increase in proton density. Both effects lead to a local increase in signal intensity and cause the lesion to appear bright.

3. Methodological Issues

This chapter gives an overview of the main signal processing steps which are consistently used in this thesis, considering data acquisition, data reconstruction and data analysis. The technical details of the used MRI hardware, the software framework for reconstruction and simulation of the image data, and image analysis methods are introduced.

3.1. MRI System

All measurements were performed on a clinical whole-body MRI system (Achieva, Philips Healthcare) which is shown in figure 14a. The system operates at a field strength $B_0 = 3T$ and is equipped with gradient hardware capable of a maximum gradient amplitude of $40mT/m$ per gradient channel, with a maximum slewrate of $200mT/ms$. The bore has a diameter of $60cm$ and a length of $130cm$ including the casing. The maximum achievable FOV results in $50cm$ in x (right $\longleftrightarrow$ left) and y (posterior $\longleftrightarrow$ anterior) direction and $45cm$ in z (feet $\longleftrightarrow$ head) direction. For imaging, separate coils were used for the RF excitation and the signal acquisition. Excitation was done with the integrated body coil, which is mounted to the casing of the bore. For receiving the resonance signal, special surface coils were used, which provide a high signal-to-noise ratio and much faster switching times to receive state after RF excitation than the body coil. This fast switching of the coil is essential for the acquisition of the MR signal of tissues with very short T_2^* relaxation times and is

in the range of a few ten microseconds for the coils used for the presented applications. Instead of the body coil the surface coil has a limited view over the FOV which modulates over the object. Surface coils are often composed of more than a single coil element with each element having an individual modulated view of the object. This specific modulation of the individual receiver element is called sensitivity profile which describes the spatial sensitivity $S(\vec{x})$ of the coil:

$$I(\vec{x})_{surface-coil} = S(\vec{x}) \cdot I(\vec{x})$$

To get a homogeneous signal distribution over the image a reference scan has to be performed. This scan consists of a set of images including images received with each individual coil element and one image received with the body coil. A combined image is obtained by either calculating the sum of square of the individual intensities from the single coil elements or the sum of all coils divided by the intensity of the homogeneous intensity image of the body coil. To achieve a homogeneous signal in the reconstructed images, the sensitivity maps can now be used to scale the signal intensity variations caused by the surface coils. In regions where none of the surface coil elements receives a signal the resulting image stays noisy.

For the trajectory mapping the same coil was used for transmission and reception (fig. 14b) to achieve a homogeneous signal over a large FOV. The birdcage design enables homogeneous coverage over the region of interest.

The in-vitro measurements for analysing T_2^* effects and comparing SNR between the acquisition strategies were acquired with an one element prototype solenoid mouse coil (Philips Research Europe, Hamburg, Germany), which is shown in figure 14c. The bore of the cylindrical small animal coil measures $40mm$. This coil is suitable to acquire signals from very short T_2 tissues (rapid switching) with a very high signal-to-noise-ratio.

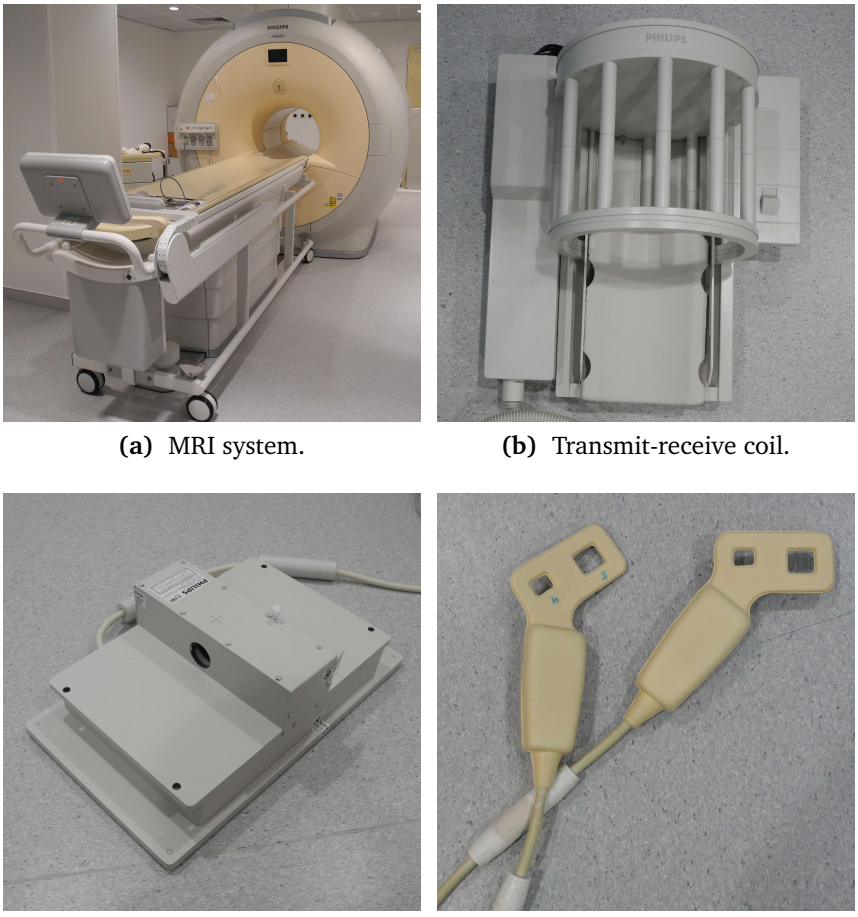

(a) MRI system. **(b)** Transmit-receive coil.

(c) Mouse coil. **(d)** Carotid coil.

Figure 14.: MRI hardware.

The in-vivo data for the clinical studies were acquired with a prototype two times two-element carotid artery coil (fig. 14d) sized $70mm \times 50mm$ each (Philips Research Europe, Hamburg, Germany). The two segments were located on either side of the jaw aligned with the central line between upper and lower jaw. The coil was fixated with a Vac-Lok neck cushion (Medtec, USA), which also immobilized the head of the patient to a great extent.

All sequences were implemented in Goal-C language using the puls-programming environment from Philips. Sequence modules are executed on a real-time unit which runs the operating system and therefore takes control of RF pulse generation, signal acquisition and gradient switching. For image reconstruction the raw data (k-space data) and the specific scan parameters collected by ReconFrame [18] were reconstructed off-line with an in-house developed reconstruction framework.

3.2. Reconstruction Framework

To perform image reconstruction for the proposed techniques the MATLAB [32] based in-house build software framework [27, p. 49ff.] had to be extended and rewritten to a system independent module-based framework called TIGER-RECON (Tiger Iterative Gridding Reconstruction). This allows the integration of new imaging and reconstruction techniques as encapsulated modules while the main image processing steps are provided by the framework. TIGER-RECON is split into four main modules (Fig. 15): the import of the raw data and of the specific sequence and scan parameters, the calculation of the k-space trajectory and of the sampling density, the calculation of the coil sensitivity maps and as final step the reconstruction from the k-space data into an image.

- Module I: This module is the only one which has to be adapted for using the TIGER-RECON framework with other data and parameter formats. Thus the whole framework can be used system independent. It imports the preprocessed raw data and sequence specific scan parameters from ReconFrame and adapts them to the requirements of the reconstruction framework. The basic corrections provided by ReconFrame which are applied to the exported raw data, are:
  - Direct current (DC) offset correction: compensation for signal offset in the raw data by subtracting the average signal of the noise, which is equally distributed

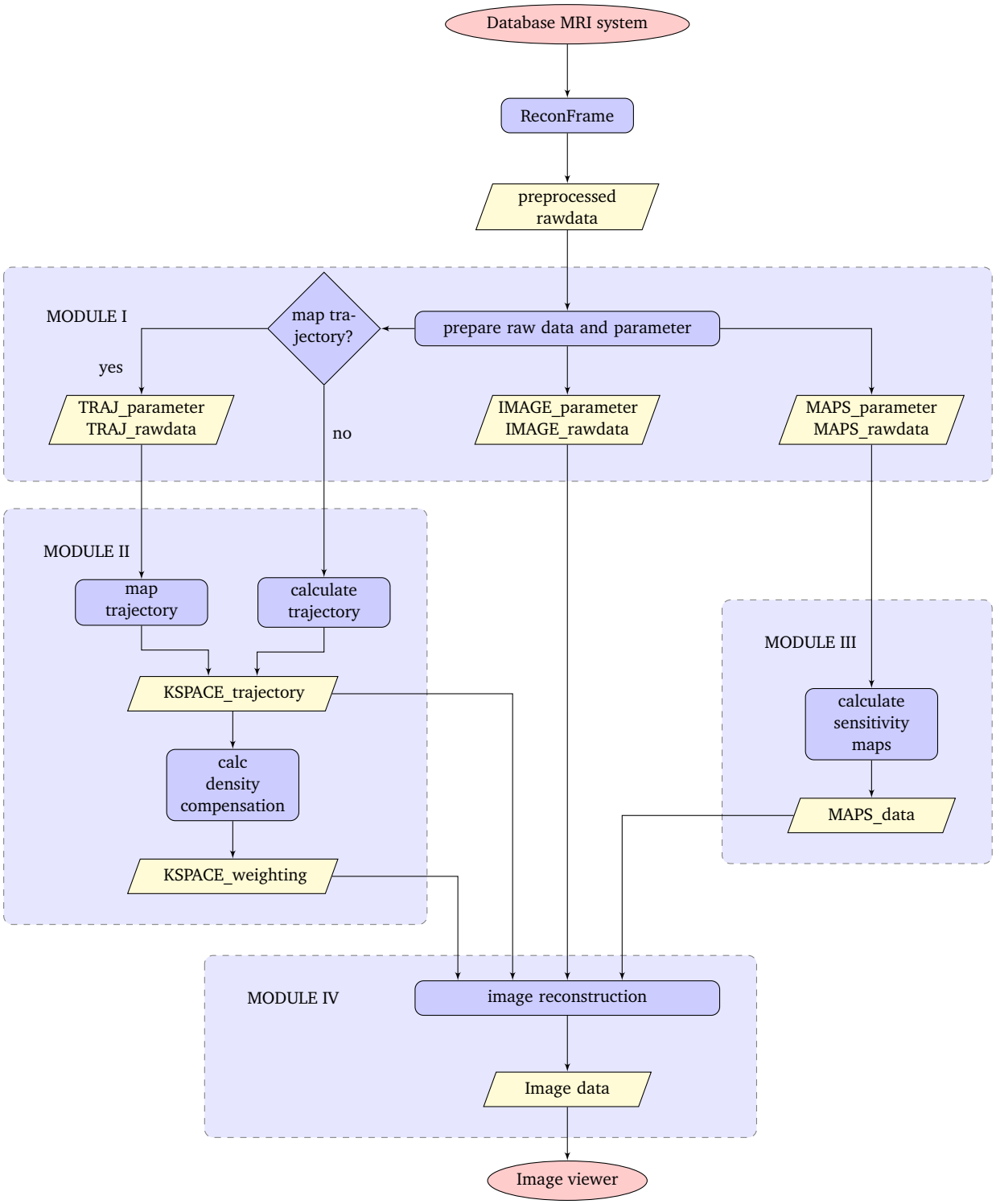

Figure 15.: Flowchart of the TIGER-RECON reconstruction software.

and therefore should be zero. Instead of optional noise data, the outer k-space regions are used with the assumption that these regions behave noise-like.

- Profile dependent amplification (PDA) correction: compensation of the scaling of different k-space profiles depending on their k-space location added by the receiver.
- Random phase correction: correction of the random phase added by the receiver to every measured k-space profile.
- Measurement phase correction: compensation of the relative phase offset between multiple acquisitions of the same k-space profiles (e.g. profiles from different averages).

The parameter file includes scan specific parameters like the scan mode (3D/2D), the acquisition mode (cartesian/radial), the scan geometry (offset and angulation) and contrast defining time settings like the echo time TE, the inversion time TI and the repetitions time TR. Sequence object dependent parameters like the gradient strength and timing, and the length and timing of the acquisition object are available for the calculation of the k-space trajectory. For the reconstruction algorithm, the encoding parameters like acquisition samples per profile and number of profiles, the size of the reconstruction matrix and therefore the resolution of the reconstructed image, and the parameters for iterative reconstruction are provided by this module.

- Module II: This part of the reconstruction framework calculates the k-space trajectory and the weighting of the k-space values. There are two different methods for calculating the k-space trajectory. The first is based on the calculation of a single trajectory profile by integrating over all gradients in readout direction. Optionally a gradient waveform and timing correction can be prepended. The k-space coordinates related to the measured signal can be achieved by determination of the values

of $k(t)$ at the exact time of the sampling points. The second approach calculates the trajectory by using an additional preparation scan for trajectory mapping based on the approach of Duyn [13]. The values for k-space sampling density compensation can be determined by calculation of the Voronoi cells, which is very time consuming, or for equally distributed radial acquisition schemes by taking the distance to the k-space center into account [15].

- Module III: This module is optional and is used for iterative reconstruction methods and for the correction of the coils sensitivities by calculating the coil sensitivity maps. After calculation of the maps' values, the geometry of the imaging sequence and the geometry of the coil reference scan have to be adapted. The coil sensitivity maps are forwarded to the image reconstruction algorithm.
- Modul IV: It provides the image reconstruction including gridding of the raw data, sampled at arbitrary k-space values, optional coil sensitivity compensation and inverse Fourier transformation into the spatial domain.

3.3. Simulation Framework

The TIGER-SIM framework is used to simulate system non-idealities resulting from field imperfections as well as tissue dependent attributes like relaxation and precession frequency. TIGER-SIM consist of five modules. One for trajectory calculation, two to provide each phantoms raw data and coils sensitivity maps, one for simulating of timing and signal imperfections and finally the image reconstruction module. The gridding algorithm and the trajectory calculation use the same source code than in the TIGER-RECON framework to ensure that artefacts observed in the experimental images are not due to implementation differences. The simulation is based on the fact that the MRI signal corresponds to the Fourier transformation of the object in image space and vice versa. For the simulation

the k-space data of an arbitrary phantom could be achieved by Fourier transformation of the object and regridding the k-space data to the chosen k-space pattern. To avoid the influence/inaccuracy of regridding on the phantom data, a phantom with an analytical solution for the Fourier transformation can be obtained by calculating the k-space value of each k-space coordinate. Based on the linearity and shift property of the Fourier transformation various phantoms could be created by superposition of objects with different sizes, amplitudes and offcenter values.

$$\sum_i a_i f(x) \quad \circ\!\!-\!\!\bullet \quad \sum_i a_i F(f) \tag{3.1}$$

$$f(x - x_0) \quad \circ\!\!-\!\!\bullet \quad F(f) \cdot e^{-2\pi f x_0} \tag{3.2}$$

The used analytical Fourier transformation formulas for different image dimensions are:

$$F_{rect}(k_x) = 2r \, \frac{\sin\left(2\pi r|\vec{k}|\right)}{2\pi r|\vec{k}|} = 2r \, \mathrm{sinc}(2\pi r|\vec{k}|) \qquad 1D \tag{3.3}$$

$$F_{disc}(k_x,k_y) = r \, e^{-i2\pi\vec{k}\cdot\vec{x}_0} \cdot \frac{J_1(2\pi r|\vec{k}|)}{|\vec{k}|} \qquad 2D \tag{3.4}$$

$$F_{ball}(k_x,k_y,k_z) = e^{-i2\pi\vec{k}\cdot\vec{x}_0} \cdot \frac{\sin\left(2\pi r|\vec{k}|\right) - 2\pi r\,|\vec{k}| \cos\left(2\pi r|\vec{k}|\right)}{2\pi^2|\vec{k}|} \qquad 3D \tag{3.5}$$

where $\vec{x}_0$ is the displacement of the object in the spatial domain, r the radius of the object, $|\vec{k}|$ the distance from the k-space center and J_1 the Bessel function of first order.

The simulation tool provides different simulation properties depending on user defined system imperfections, k-space acquisition schemes and image reconstruction techniques.

Simulations can be done in 1D, 2D and 3D. First step is the calculation of the k-space trajectory based on sequence parameters like acquisition timing, gradient strength and slewrate and sampling interval. The parameter file for trajectory calculation is either provided by a real measured imaging sequence or parameters could be defined manually. Based on the calculated trajectory and user defined parameters like size, number of objects and initial magnetization M_0, the k-space data of the phantom is generated. The next module simulates the effect of signal imperfections like off-resonances and contrast manipulating relaxation mechanisms. For multi-component phantoms different T_2^* decay values and off-resonance frequency can be chosen. Local field deviation can be simulated by causing phase drift of the signal from single object in the phantom. If required the MTF and PSF – depending on k-space sampling scheme and time depended imperfections – are calculated and amplitudes and FWHM are calculated for comparison. Like in TIGER-RECON software coil sensitivity maps could be optionally generated to simulate coil depended modulation over the region of interest. In a last step the manipulated raw data is regridded and the results can be inspected with an image GUI of TIGER-SIM which provides analysis functions like windowing, zooming, sliding trough 3D volume, image subtraction, profile calculation and SNR measurements.

3.4. Signal-to-Noise Ratio

The MR signal is usually degraded by noise, caused by various effects like imperfections of the MR system (e.g non-linearity of signal amplifiers, field inhomogeneities) and thermal noise from the measurement object, the RF coils and the electronics. The signal-to-noise ratio describes the impact of the background noise to the achieved signal by comparison of the signal intensity of a chosen Region Of Interest (ROI) to the level of the background noise.

The measured MR signal is the integral over the signal from all voxels in image space

$$S(\vec{k}) = \int_V \rho(\vec{x})\, e^{-i2\pi\vec{k}\vec{x}}\, \mathrm{d}^3x$$

$$= \sum_i^{voxel} \int_{V_i} \rho(\vec{x})\, e^{-i2\pi\vec{k}\vec{x}}\, \mathrm{d}^3x$$

where the overall signal of the spin density is described by the signal at $\vec{k} = 0$:

$$S(\vec{k}=0) = \sum_i^{voxel} \int_{V_i} \rho(\vec{x})\, \mathrm{d}^3x.$$

The signal at $k = 0$ induces a voltage in the RF coil which depends on the number of spins and therefore the sample volume V_s, on the precession frequency, and the degree of spin polarization. The last two are both proportional to the main magnetic field B_0 and the strength of the coupling between the spins and the coil. This coupling can be described by the principle of reciprocity [25] and is proportional to the time-varying magnetic field composed of the transversal magnetization and the component of B_1 which is perpendicular to B_0: $\frac{\mathrm{d}}{\mathrm{d}t}(M_\perp(\vec{x}_i) \cdot B_\perp(\vec{x}_i))$. Neglecting relaxation effects, considering a homogeneous sample, an uniform B_1 and an uniform B_0, and suppose that the equilibrium magnetization M_0 is uniformly rotated into the transverse plane with an on-resonant $\pi/2$ pulse the signal can be treated as independent of $\vec{x}$:

$$S(\vec{k}=0) \propto \omega_0 M_\perp B_\perp V_s. \tag{3.6}$$

The noise is an unwanted portion of signal that obscures the desired signal and degrades the accuracy of the measurement. The effect of thermal noise can be described by the input impedance of the measurement object, the RF coil and the electronics. This relationship is

indicated by the fluctuation dissipation [47]. Random electric and magnetic fields are produced due to the thermally activated motion of the charge carrier. This field disturbances can be detected as noise. The noise voltage generated by a resistance R at the absolute temperature T (K) is given by [23]:

$$\sigma^2_{therm} = \sqrt{4k_B \cdot T \cdot R \cdot BW_{read}}, \tag{3.7}$$

where k_B is the Boltzmann constant and BW_{read} the receiver bandwidth in Hertz and $R = \frac{P}{I^2}$ represents the power losses of the coil and of the biological sample by a unit current I in the coil. Since the noise is not measured in the detected signal but in image space, the variance measured in any voxel of the image space is N (where N is the overall number of covered k-space samples) times smaller. For an uniform B_1 field the noise for 3D imaging adds up to:

$$\sigma^2_{img} = \frac{\sigma^2_{meas}}{N_x N_y N_z}$$

The signal-to-noise ratio in a single voxel therefore results in:

$$SNR(\vec{x}) \propto \frac{\Delta x \Delta y \Delta z \cdot ||M_\perp B_\perp||}{\sqrt{\frac{4k \cdot T \cdot R \cdot BW_{read}}{N_x N_y N_z}}}. \tag{3.8}$$

Since the receiver bandwidth is defined over the time used for the readout $BW_{read} = {}^1/_{T_{ACQ}} = {}^1/_{(N_{RO} \cdot \Delta t_{ACQ})}$ the SNR results in:

$$SNR(\vec{x}) \propto \Delta x \Delta y \Delta z \cdot \sqrt{T_{ACQ} N_y N_z} \tag{3.9}$$

In a radial sampling approach the signal encoding is based on frequency encoding only. Therefore $N_y \cdot N_z$ depends on the number of radial profiles $N_{profiles}$. In case of center-out sampling a single k-space line is composed of two k-space profiles with opposite direction. Therefore the doubled number of profiles is necessary to cover the whole k-space. The SNR stays the same as in conventional radial sampling, neglecting the additional readout time for non-equidistant k-space coverage during ramp sampling.

The signal-to-noise ratio in images can be calculated by dividing the mean of the local signal in the region of interest and the standard deviation of the noise in a relative large ROI. The achieved signal consists of the ideal signal and the noise $S_m(k) = S(k) + N(k)$. For non-white noise the mean value is not zero and therefore the SNR has to be calculated by the difference between the mean signal and the mean noise signal, divided by the standard deviation of the noise. Important is a nearly perfect uniform background signal in the area where the noise is measured. In most scans it is very difficult to find areas where the signal is perfectly uniform and which have no impact from motion or back folding artefacts. An alternative approach to retrieve an uniform region of noise is a two-scan approach by getting one scan without RF excitation and gradients but with the same scan parameters like the imaging sequence. Since the noise measured in a modulus image, it is not Gaussian (but Rician and for very low SNR values even Rayleigh), and one has to compensate for this in absolute SNR measurements. For magnitude MR images, the standard deviation in regions without signal is given by 0.655σ [20]. For relative SNR calculation used in this thesis no compensation is necessary for comparison of the different acquisition approaches.

4. Dedicated MRI Techniques for Ultra-Short Echo Time Imaging

Standard MRI sequences have only limited sensitivity to changes in tissues with high mineral content and related high transversal T_2^* relaxation times like the main tooth components - enamel and dentine. In the 1980s a new pulse sequence was introduced by Pauly [33] which enables much shorter echo times (TEs) than in conventional MRI sequences and can detect signals from tissues with very short T_2^* values. Over the last decades a diversity of dedicated imaging sequences were introduced to detect the signal of tissues with ultra-short T_2 or T_2^* values directly or indirectly. This chapter gives a short overview of the fundamental idea of ultra-short echo time imaging and discusses the general advantages and disadvantages of the mainly used techniques to select an appropriate sequence for visualization and quantification of caries lesions.

4.1. Sequence Requirements

Since there is no convenient generally accepted definition which range of T_2 or T_2^* is covered by ultra-short echo time imaging sequences this work focus on tissues and structures in human subjects which have such short T_2 or T_2^* values that the signal of these tissues can not be observed by conventional clinical imaging techniques. According to Bydder [11] T_2 or T_2^* values in the range of 1 to 10ms are defined as short, in the range of 0.1 to 1ms as

ultra-short and below $0.1ms$ as super-short. The spin-spin relaxation time results below $1ms$ for dentine [42] and below $250\mu s$ for enamel [14], both values were measured at 1T main magnetic field strength. The mineral dental structures therefore belong to the class of ultra-short T_2^* tissues.

To image tissues with very short T_2^* values, one has to account for a number of signal behaviours that do not exist for imaging of tissues with long T_2^* times (e.g. signal relaxation during RF excitation and high signal decay during signal acquisition). Substantial signal decay can occur during the RF pulse since the relaxation times are short compared to the duration of typical used excitation pulses. Also the achieved flip angle deviates from the predicted value [46].

The fast relaxation of the signal does not only require quick RF excitation, but also the k-space and especially the samples in the k-space center have to be acquired very shortly after the excitation. Therefore conventional k-space encoding techniques like phase encoding and gradient echo are not a suitable option for these imaging techniques.

The time to sample the first data point after RF excitation is limited by the switching time of the RF front-end from transmit to receive mode, by signal build-up of the digital filter and optionally by the time the slice selective gradient needs to decay to zero. The time needed for switching the system from transmit to receive state is usually referred as *dead time* t_{Dead} of the system. There are three steps to switch the RF hardware from transmit to receive state, which are digitally controlled in modern MRI systems. First step is to stop the RF transmission which takes typically 20-30μs but can be reduced with some effort down to $10\mu s$. To start the reception of the MR signal a receiver amplifier and an A/D-converter have to be turned on which takes only a few microseconds (1-2μs). The most time consuming step in the receive path is the use of a digital filter for decimation of the incoming digital signal. It typically needs 10-30μs to stabilize the decimation algorithm and generate the first valid sample. On routinely used clinical MRI systems the minimum

switching time is about 50-200μs. A reduction of the echo time down to 8μs on a clinical system is reported using additional dedicated hardware [9]. For further signal encoding usually some form of radial acquisition is used to avoid the additional time for an phase encoding gradient.

4.2. Imaging Sequences

4.2.1. SPRITE

Single-Point Ramped Imaging with T_1 Enhancement (SPRITE) [2] is a variant of a Single Point Imaging (SPI) [16] technique. A characteristic feature of these techniques is the k-space coverage by applying phase encoding steps only. Every k-space point is sampled at a fixed encoding time t_p after the RF excitation pulse (fig. 16a) which leads to an equal T_2^* weighting for all k-space points. SPI sequences are usually encoded on a cartesian grid.

The imaging gradients are turned on prior to spin excitation. This helps to avoid encoding problems due to eddy currents which result from rapid gradient switching. To ensure uniform excitation in spite of varying gradient amplitudes during the RF pulse, the bandwidth of the block pulse must satisfy the following condition [16]:

$$BW > \frac{\gamma}{2\pi} G_{max} \cdot FOV,$$

where $G_{max} \cdot FOV$ defines the maximal spectral width. The duration of a rectangular pulse is approximately the inverse of its bandwidth:

$$t_{RF} < \frac{2\pi}{\gamma G_{max} \cdot FOV} = \frac{2t_p}{N},$$

where N represents the number of samples used to fill a single k-space line.

The k-space coordinate will be changed by the amplitude of the applied phase encoding gradients:

$$k_n = \gamma \frac{G_n t_p}{2\pi}.$$

The gradient increment is calculated in relation of the chosen field of view:

$$\Delta G = \frac{2\pi}{\gamma t_p FOV},$$

and the maximum resolution is limited by the maximal achievable gradient strength

$$\Delta r_{max} = \frac{\pi}{\gamma t_p G_{max}}.$$

Compared to basic SPI sequence SPRITE switches the gradients not on and off between two excitations but ramp them in discrete steps (fig. 16b) while a single data point is sampled during each gradient step. The gradient step length is less than $5ms$ to avoid exceeding duty cycle restrictions. The overall gradient duration is brief and mechanical forces of the gradients are minimal, which reduces the sound volume of the sequence. The ramped gradient version of SPI minimizes gradient vibrations and reduces the imaging time since ramp up and down of the encoding gradients are avoided.

SPI methods have an attenuated but constant MTF and therefore a dirac-shaped PSF. They are free from spatial distortions due to B_0 inhomogeneities, susceptibility variations and chemical shift, and thus provide the lowest degree of T_2 weighting of any imaging sequence. There are no delays due to gradient switching. SPI methods have very long scan times related to the pure phase encoding and a high number of RF pulses due to the low number

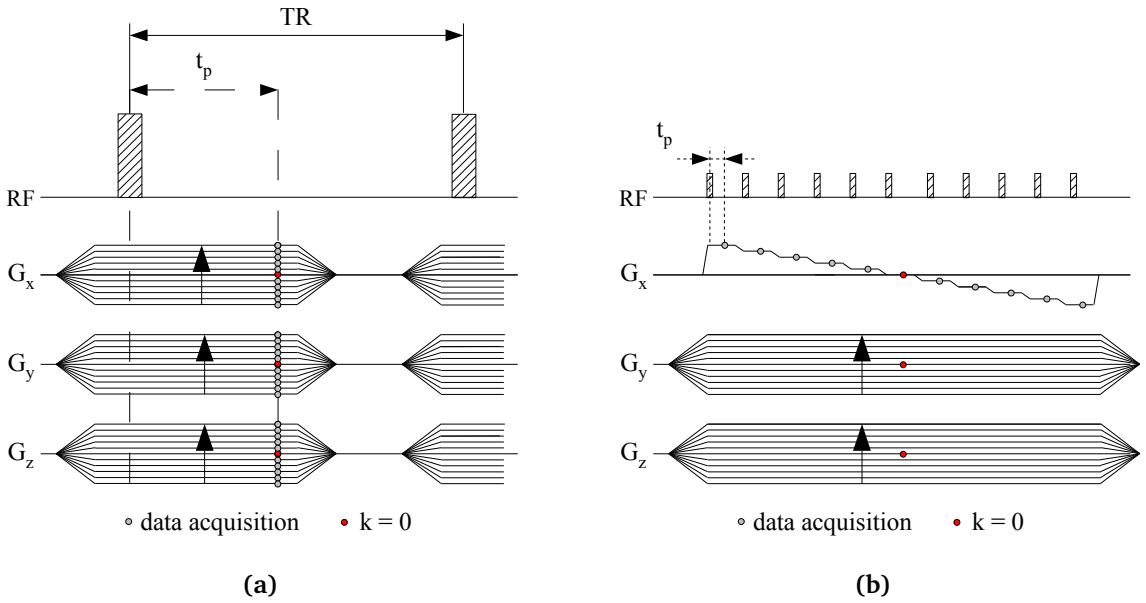

Figure 16.: (a) SPI sequence: a single k-space point is sampled at discrete phase encoding steps at a fixed time point t_p after RF excitation. A phase encoding gradient is ramped up in front of the RF pulse and is settled before excitation starts. An additional time interval between ramp down of the gradient and the next RF pulse allows the eddy current components of the gradient to decay to zero. (b) SPRITE sequence: The phase encoding gradients are ramped in discrete steps between the RF pulses instead of switching them on and off. This minimizes the mechanical forces of the gradients and the related sound of the gradient switching. The transverse magnetization is inherently spoiled by the phase encoding gradients.

of sampling points per excitation. So they find only limited use in biomedical applications but are actively used in material science.

4.2.2. ZTE

Zero echo time is not only a specific imaging sequence but it is also a epitome for a range of frequency encoded sequences which achieve zero echo time by switching the encoding

gradient before the RF pulse is applied. Since the full gradient strength is already set right after RF excitation, the full k-space speed is immediately available. Figure 17 shows the general acquisition scheme for magnetic resonance imaging with zero echo time and hard pulse excitation.

Like in the SPRITE imaging technique, the signal bandwidth induced by the readout gradient across the object must be excited uniformly by the RF pulse. Otherwise this will lead to inconsistencies between different projections. To achieve such wide band excitation a short hard RF pulse is used.

The gradient amplitude for the encoding gradient is given by the desired nominal resolution Δr

$$G = \frac{2\pi}{2\gamma T_{enc} \Delta r},$$

and the sampling interval Δt (nominal dwell time), which is given by

$$\Delta t = \frac{1}{BW} = \frac{2T_{enc}}{N}.$$

The k-space center can not be sampled because it is located inside the RF pulse since k-space encoding starts during excitation. Due to the dead time t_{Dead} of the system, certain initial k-space samples are missed.

There are several approaches addressing the initial gap to avoid baseline artefacts caused by missing data samples at k-space center. The missed k-space region in the center can be filled by either using additional measurements, like in WASPI [51] (water and fat-suppressed proton projection MRI) and PETRA [17] (pointwise encoding time reduction with radial acquisition), or dedicated reconstruction techniques like in RUFIS [31] or other ZTE approaches [48].

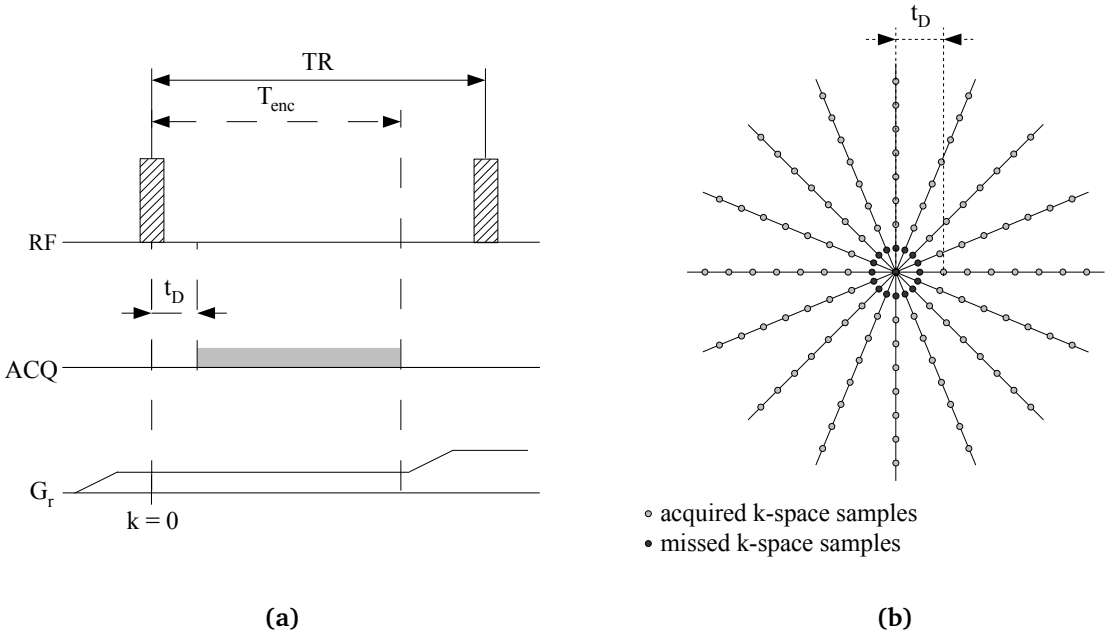

Figure 17.: (a) General ZTE sequence: the frequency encoding gradient amplitude is set in front of the RF pulse and is settled before excitation starts. Gradient amplitude is ramped in discrete steps between the RF pulses. A hard RF pulse is used to excite the full signal bandwidth. Since the encoding starts immediately after creation of transverse magnetization, the k-space center can not be sampled directly. The minimum repetition time of this sequence is related to the encoding duration, the time the gradient needs to settle after switching to the next encoding direction and the time needed for spoiling the residual transverse magnetization. (b) ZTE sampling scheme: a central plane of 3D sampling scheme is shown where all dots are required to fulfil the Nyquist criterion. White dots illustrate the acquired sampling points. Black dots illustrate missed k-space data points due to the dead time t_{Dead}.

In the WASPI imaging technique the k-space gap is filled by repeating a small number of radial acquisition at a reduced gradient amplitude and therefore decreasing the area of initial missed k-space. PETRA covers the missed k-space region by additional cartesian SPI acquisition, which facilitates zero echo time imaging even for a large system dead time. Both techniques have to deal with behaviour of k-space apodization by combining measurements with different time settings. The dedicated reconstruction based technique RUFIS is

using a least square fit algorithm of the sampled data to approximate the missed data in k-space center. Weiger [48] uses a more general algebraic reconstruction approach [34] – instead of standard gridding with subsequent Fourier transform – to avoid baseline artefacts due to missed central data samples with combined acquisition oversampling to increase the effective bandwidth of the digital filter and therefore reduce the dead time penalty due to digital filtering. For both reconstruction-based methods it is highly recommended to start sampling as close to k-space center as possible.

The contrast is less versatile in ZTE than in other imaging sequences for ultra-short T_2 or T_2^* imaging due to the fixed echo time at zero and usually is predominated by the spin density of the tissues.

4.2.3. UTE

In Ultra-short Echo Time (UTE) [21, 41, 46] imaging the encoding gradient G_r is applied after the excitation pulse. This facilitates a selection of the excited volume by applying a slice selection gradient during the RF pulse. Figure 18 shows an UTE sequence with half-sinc excitation and the trajectory for a single k-space profile. Although broadband excitation is not longer necessary, it is recommended to keep the pulse length as short as possible and thus minimize the signal decay during excitation.

For slice selection either a half-sinc or VariablE Rate Selective Excitation (VERSE [12]) pulse can be applied for spin excitation. Since only a half RF pulse is applied the measurement has to be repeated with positive and negative slice selection gradient to obtaining a full excited k-space by summing up the signals of the measurements. Unfortunately non-linearities lead to a shift in time between the measurements and therefore linear superposition is no longer given for signal summation. In half-sinc excitation the RF waveform is splited into two halves by dividing the pulse at the zero-phase point. The obtained pulse

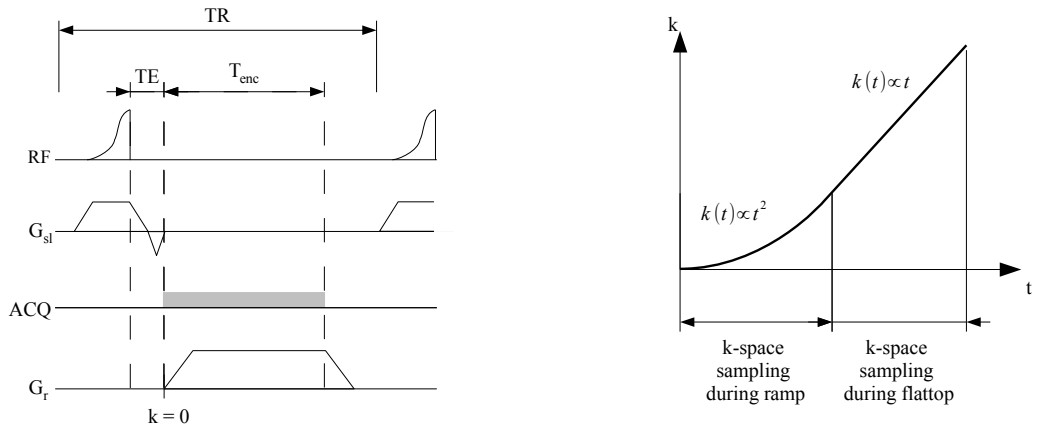

(a) **(b)**

Figure 18.: (a) General UTE sequence : Half-sinc excitation is applied for 2D slice selection to shorten the time for nulling of the slice selection gradient and thus the minimal achievable echo time. In three-dimensional UTE imaging a hard pulse can be used for excitation instead of the half-sinc pulse. The k-space center is acquired during ramp up of the encoding gradient. (b) k-space profile: sampling during the ramp of the gradient leads to a non-linear k-space encoding in the center.

shape is played out during flattop of the slice selection gradient and the gradient is ramped down after the RF excitation is switched off. A rephasing gradient is applied for gradient nulling to compensate the area under the ramp. In the VERSE approach, the slice selection gradient is ramped down during the RF excitation and no rephasing gradient is used for slice selection gradient nulling. Three-dimensional UTE imaging sequences typically use hard pulse excitation like in ZTE (sec. 4.2.2) and SPI (sec. 4.2.1) techniques.

The minimal echo time is limited by the time for ramp down and gradient nulling of the slice selection gradient for half-sinc excitation and by the dead time of the system for VERSE or hard pulse excitation. After the echo time is reached the encoding gradient is ramped up with instantaneous start of the signal acquisition to facilitate the coverage of the k-space center. Besides the typical non-linear k-space sampling in radial direction the

signal acquisition during ramp up of the encoding gradient additionally leads to varying distance of k-space samples Δk along a single readout experiment. This non-equidistant sampling in readout direction during the coverage of k-space center has to be considered during image reconstruction.

The impact of signal attenuation of short T_2 tissues during acquisition on the PSF amplitude and the linewidth of the signal, increases with [37] decreasing slewrate and related prolongation of the acquisition duration.

The separation of signal excitation and encoding in UTE imaging allows variable echo time settings and/or application of preparation pulses and therefore provides various changes in image contrast and facilitates quantitative T_2^* measurements.

4.2.4. SWIFT

SWeep Imaging with Fourier Transform (SWIFT) [24] uses a swept radiofrequency excitation of the nuclear spins instead of a hard pulse and acquires the signals in the time-domain in a time-shared manner during the pulse. The pulse covers the frequencies of a desired bandwidth in a successive manner and can achieve any flip angles also at limited B_1 by increasing the pulse length.

The general realization of a SWIFT sequence is shown in Figure 19. Encoding of the MR signal along a radial projection is realized by a segmented RF pulse which utilizes amplitude as well as frequency modulation. To miss no signal during the pulse, data acquisition must be executed simultaneously with the excitation. This can be done by switching between RF transmission and signal reception in an alternating mode. For the periodically gapping, each of the RF segments is switched on for a given time τ_p followed by a fixed delay with RF power off. During this time, data acquisition is performed at a

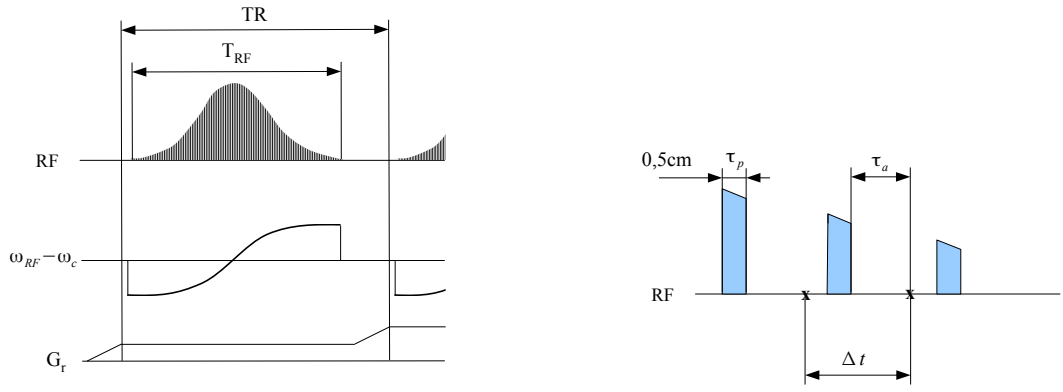

(a) **(b)**

Figure 19.: (a) SWIFT sequence: The sequence for a single projection composes a gapped RF pulse with N segments of equal duration. Signal acquisition is applied during the gap between the segments where the RF power is switched off. Three-dimensional k-space encoding is realized by additionally applying field gradients during the time-shared excitation and acquisition. (b) Detailed presentation of the pulse segments

given time τ_a after the pulse segment. The repetition time is given by the pulse duration T_{RF} and the time to switch the gradient to the next encoding direction .

The dwell time of data sampling is given by the duration of the RF pulse – which is equal to the time of data encoding – and the used pulse segments:

$$\Delta t = \frac{T_{RF}}{N}.$$

The maximum excitation bandwidth is equal to the spectral width *sw* of the pulse:

$$BW = sw = 2\pi\frac{N}{T_{RF}}.$$

In accordance with the other presented sequences, magnetic field gradients are used for changing the spatially depended Larmor frequency of the spins to achieve a full covered three-dimensional k-space. The gradients are switched on during time-shared excitation and acquisition.

During image reconstruction the evolution of magnetization during the complex excitation pulse must be considered. This can be done by using either a deconvolution [24] or an algebraic approach [49]. In the deconvolution approach, both the acquired signal and the excitation pulse are Fourier transformed to form the respective frequency domain equivalents and the projection of the object is formed by correlation of the two signals. For the algebraic approach the RF pulse is treated as a series of hard excitation pulses at different times and different complex amplitudes which create different superimposed signal contributions.

For increased spectral width – which is equal to increased dwell time – sensitivity for short T_2 and T_2^* signal decreases. Therefore the contrast in SWIFT is dominated mainly by proton density for small excitation angles and by T_1 for large flip angles. To produce the desired T_2 weighted contrast a contrast generating magnetization preparation module can be applied [30] .

4.3. Discussion

SPRITE, ZTE, UTE, and SWIFT are the mainly used sequences for imaging tissues with ultra-short T_2 and T_2^*. Although they all focus on rapid sampling of the k-space center they have strongly different behaviours regarding resolution, imaging artefacts, scan time, and hardware and software requirements.

The best image quality can be achieved by SPI due to the dirac shaped PSF and the non-sensitivity to variations of the magnetic field. But the minimum TE is governed by the requested resolution and the maximum available gradient strength and therefore high resolution images are achievable only with relative long echo times. ZTE imaging enables signal acquisition nearly at an echo time of zero independently of the image resolution and the maximum achievable gradient strength. However, like in all frequency encoded techniques the signal attenuation during signal encoding leads to a non ideal PSF and reduces resolution and increases blurring. Besides, the imaging with fixed echo time at zero increases susceptibility to artefacts for solid materials outside the FOV (e.g. present in the receiver hardware). Since UTE does not use the full available gradient strength from the beginning of acquisition, the k-space is sampled at a lower speed than in ZTE imaging which further reduces the resolution due to transverse relaxation. Blurring is increased by local susceptibility gradients and to achieve good image quality the eddy current induced changes in signal encoding must be well known or compensated. On the other hand gradient ramp up after excitation which is used in UTE imaging sequences enables the use of pre-pulses to suppress signal from materials with extremely short T_2^*s.

UTE enables variable T_2^* contrast since it enables measurements at variable TE times. The contrast in SPI techniques can also be modified by changing the fixed acquisition time point t_p and therefore the echo time. Since SWIFT images are in principle unaffected by transverse relaxation of T_2 values greater than ten times the dwell time, the provided contrast depends only on T_1 and spin density. Also ZTE has reduced contrast options due to the fixed echo time at zero and is predominated by the spin density.

In contrast to the other techniques UTE enables slice selection and therefore also 2D imaging while SWIFT, ZTE and SPI sequences are inherently 3D imaging techniques. This is related to the presence of the encoding gradient during RF excitation which prevents slice selection in another geometrical direction.

UTE, SPI and some ZTE variants like PETRA and WASPI sequences can be applied on conventional clinical scanners. ZTE, RUFIS and SWIFT require dedicated hardware for the RF system to reduce the time between RX/TX switching to a few microseconds. In case of rapid RF switching in SWIFT, even simultaneous operation of spin excitation and signal reception would be preferable.

To achieve the images from the acquired raw data different reconstruction approaches must be applied. While SPI methods and UTE technique use standard gridding with subsequent Fourier transformation for image reconstruction, SWIFT and ZTE techniques require more complex reconstruction methods like the use of Fourier transformed shape of the excitation pulse (SWIFT), adjustment of the different scan settings (PETRA/WASPI), or algebraic reconstruction of the missed k-space center (ZTE /RUFIS).

Although image blurring is increased by the ramp sampling in UTE imaging sequence, combination of the other features have intrinsic advantages for dental imaging on clinical scanners compared to the other techniques: the use of dedicated hardware is non-essential, the sequence enables generation of T_2^* contrast by adjusting the echo time and further enables the quantification of tissues with ultra-short T_2^*s, and the acquisition times are acceptable for clinical examinations.

5. Ultra-Short Echo Time Imaging for Identification of Initial Caries Lesions

This chapter gives a detailed understanding of the selected UTE imaging sequence and the application of MRI to dental analysis of caries lesions. In the first section the applied three-dimensional UTE sequence is explained in detail regarding signal excitation, acquisition and reconstruction. The impact of system imperfections on gradient waveform and timing, and therefore on the k-space trajectory, and the related consequences on image reconstruction are discussed in section 5.2. Correction methods for the distorted k-space trajectory are presented to achieve acceptable image quality. The optimized UTE sequence is then applied for dental MR imaging to prove its potential for visualization of caries lesion. Finally the ability for quantification of the caries progress is investigated.

5.1. Imaging Sequence

In the used imaging sequence (fig. 20) the free induction decay (FID) is acquired partially during ramp up of the encoding gradient, using a fast three-dimensional kooshball acquisition scheme.

For the spin excitation a non-selective block pulse is used to excite the volume. A dedicated surface coil with limited range of sensitivity is used to receive the signal only from the region of interest (ROI) – further referred to as field of view (FOV) – and to minimize

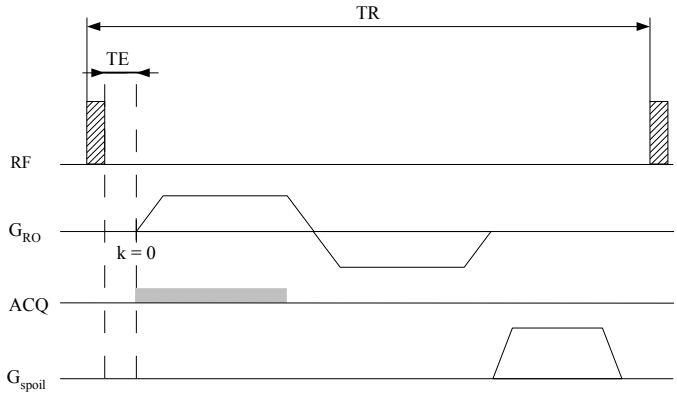

Figure 20.: 3D UTE sequence: A block pulse is used for spin stimulation to minimize signal decay during excitation. After the echo time TE – which has to be chosen at minimum to the dead time of the system – the encoding gradient is ramped up while simultaneously starting the signal acquisition. After signal reception the net-area of the encoding gradient is set to zero by a rephasing gradient and the residual transverse magnetization is destroyed by a spoiling gradient which remains on a fixed physical gradient axes for every radial profile.

oversampling artefacts. To minimize the signal decay between RF excitation and signal acquisition of k-space center the sequence uses frequency encoding only and starts acquisition in the center of k-space. This is done by simultaneously starting the signal reception and the ramp up of the encoding gradient. The echo time of the sequence is defined as the time between the end of RF excitation and ramp up of the readout gradient and is limited by the switching time of the RF system and the time the digital filter needs to build up. The time to achieve the first valid sample is defined as the dead time t_{Dead} of the system. The repetition time of the sequence consists of the echo time, the time for signal encoding, nulling of the gradient net-area and suppression of the residual transverse magnetization.

5.1.1. RF Pulse

The shape of the used block pulse – also known as rectangular or hard pulse – is simply a rect-function (fig. 21a) in the time domain. This pulse shape can be applied in MR sequences where no spatial or spectral selection is required since the bandwidth is very broad and a wide range of resonance frequencies is affected. Using block pulses, the pulse length can be kept very short and the signal decay during the pulse can be minimized. For long T_2 components the flip angle Φ is directly proportional to the width T and the amplitude B_1 of the pulse:

$$\Phi = \gamma B_1 T. \tag{5.1}$$

For tissues with short or ultra-short T_2 values the magnetization behaviour during the excitation is more complex [43, 46] and can be described considering not only the interaction of the RF pulse but also of the T_2 decay during excitation. The effect of longitudinal relaxation T_1 can be neglected due to the very high time constants compared to the pulse duration. The relaxation during excitation results in a reduction of the available transverse magnetization M_{xy} without a compensatory increase of the longitudinal magnetization M_z. The continuous excitation of spins during RF excitation compete with the dephasing of the already excited spins. The effective flip angle Φ_{eff} results in a value which is much smaller than the estimated flip angle (eq. 5.1) without consideration of T_2 decay. The behaviour of transversal and longitudinal magnetization can be described according to [43]:

$$M_{xy} = iM_0 \exp(-t/2T_2)\, \gamma B_1 t\, \operatorname{sinc}\left(\sqrt{(\gamma B_1 t)^2 - (t/2T_2)^2}\right) \tag{5.2}$$

$$M_z = M_0 \exp(-t/2T_2) \left[\cos\left(\sqrt{(\gamma B_1 t)^2 - (t/2T_2)^2} \right) + \frac{t}{2T_2} t \ \mathrm{sinc}\left(\sqrt{(\gamma B_1 t)^2 - (t/2T_2)^2} \right) \right] \tag{5.3}$$

The maximum B_1 field of the available hardware is about $13.5\mu T$.

Figure 21b shows the impact of relaxation during excitation on the magnetization for ultra-short T_2 components in the range of $50\mu s$ to $1ms$ for steps of $50\mu s$ and a long T_2 component of $100ms$ for comparison. For simulation, a $\pi/2$ RF pulse with duration of $435\mu s$ is used which should – under ideal conditions – transfer the longitudinal magnetization completely into the transverse plane. The maximum transverse signal which can be achieved for every component is marked with an '$*$' sign and is rearranged in figure 21c which shows the respective effective flip angle as a function of the related T_2 values. According to the figure the maximum signal for short T_2 tissues is obtained by using a shorter RF pulse with lower flip angle. To obtain the optimal flip angle for T_2 values observed in dental tissues the maximum transverse relaxation is simulated for different flip angles between 5° and 60°. Figure 21d illustrate the achieved transversal magnetization for a selection of flip angles between 10° and 30°. The initial transversal magnetization show conspicuous variations for the different T_2 values. The difference of the initial transversal magnetization for T_2 components in the range of 250 to $1000\mu s$ related to maximal achievable magnetization $M_{xy} = 1$ results in 1.2% ($\Phi = 10°$), 4.2% ($\Phi = 20°$),and 8.6 % ($\Phi = 30°$). Going to higher flip angle values will increase the effect of T_2 weighting due to different initial transversal magnetization while lower flip angle values decrease signal intensity without remarkable improvement of the weighting for the considered T_2 values.

In this work a flip angle value of $\Phi = 10°$ with a related pulse length of about $50\mu s$ is used as a trade-off between maximum signal intensity and minimum difference of initial transverse relaxation for different ultra-short T_2 components.

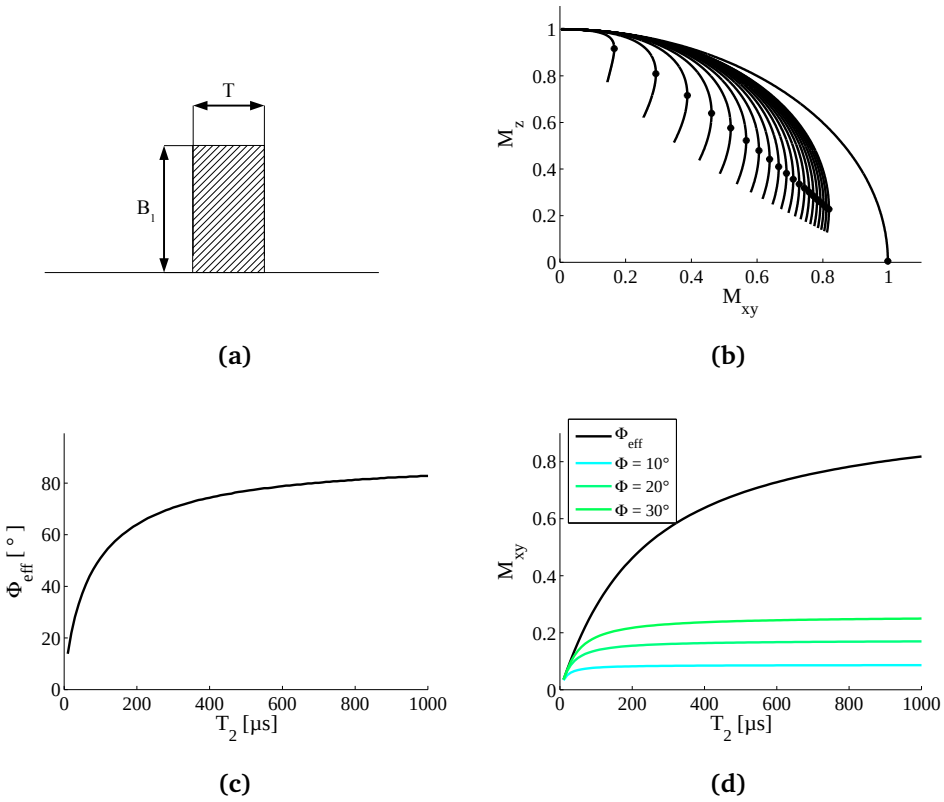

Figure 21.: Flip angle optimization for hard RF pulse excitation in ultra-short T_2^* component imaging. (a) A block or hard RF pulse. (b) Simulation of the behaviour of transverse and longitudinal magnetization during RF excitation with a 90° block pulse for components with relaxation times between 50 and $1000\mu s$ and a reference tissue with $T_2^* = 100ms$. For tissues with long T_2^* values the longitudinal magnetization is completely transformed into transversal magnetization. With decreasing T_2^* values less magnetization is rotated into the transverse plane. (c) The optimum flip angle for the different T_2^* values is achieved by calculation of the pulse duration for the maximum value of M_{xy}. (d) Initial value of transversal magnetization for different flip angles. With increasing flip angle T_2^* weighting increases due to different initial transverse magnetization.

5.1.2. Signal Encoding

A frequency encoded radial sampling scheme is implemented to cover the whole k-space. The data acquisition is started simultaneously with the rising slope of the encoding gradient and therefore the k-space is traversed from $k = 0$ outwards to the k-space peripheries. The gradient waveform for the ideal case is defined as:

$$G(t) = \begin{cases} \frac{G_{RO}}{T_{slope}} t & : 0 \leq t \leq T_{slope} \\ G_{RO} & : T_{slope} < t \end{cases} \tag{5.4}$$

with linear rising during slope duration T_{slope} at a fixed slewrate of $\frac{G_{RO}}{T_{slope}}$ and a constant gradient amplitude (flattop) afterwards.

The respective k-space trajectory can be calculated according to equation 2.21 and results in:

$$k(t) = \begin{cases} \frac{\gamma G_{RO}}{4\pi T_{slope}} t^2 & : 0 \leq t \leq T_{slope} \\ \frac{\gamma}{2\pi} G_{RO}(t - T_{slope}) + k_{slope} & : T_{slope} < t \end{cases} \tag{5.5}$$

with $k_{slope} = k(T_{slope}) = \frac{\gamma}{4\pi} G_{RO} T_{slope}$ being the k-space value at the end of the gradient ramp. The k-space trajectory has a quadratic behaviour during the gradient ramp and ends up in a linear function during constant gradient sampling.

From equation 5.5 the time dependence as a function of k-space can be expressed as followed:

$$t(k) = \begin{cases} \sqrt{\frac{4\pi k \cdot T_{slope}}{\gamma G_{RO}}} & : 0 \leq k \leq k_{slope} \\ \frac{2\pi}{\gamma G_{RO}}(k - k_{slope}) + T_{slope} & : k_{slope} < k \end{cases} \tag{5.6}$$

In case of equidistant k-space sampling the time behaves like a root function during gradient rising and results in a linear function after the linear part of the trajectory and therefore the constant gradient is reached. These notation is required for the investigation of time depended behaviours like relaxation and off-resonance effects.

Figure 22 illustrates the effect of non-equidistant sampling in the k-space center. The ramp sampling enforces the effect of inherent oversampling in radial acquisition schemes towards k_0.

The duration of the sampling window is limited by the maximum slewrate of the system $S_{max} = 200mT/ms$, the maximum executable gradient amplitude $G_{max} = 31mT/m$, and the desired image resolution, and is usually in the order of a several hundred microseconds. The sampling duration of an arbitrary set of scan parameters is given by:

$$T_{ACQ} = \frac{2\pi k_{max}}{\gamma G_{RO}} + \frac{1}{2} T_{slope} \tag{5.7}$$

where the second term represents half of the slope duration and $k_{max} = k(T_{ACQ})$ is determined by the chosen image resolution.

To cover a volume of interest the radial profiles are distributed isotropically over a sphere. If the number and distributions of the radial projections where chosen to ensure a con-

stant angular velocity sampling on the surface of the sphere, then this will lead to higher sampling density near the poles compared to the equatorial region. A sampling scheme to cover a surface of the sphere with nearly uniform distribution of the points was proposed by Wong et al [50]. The angular distribution of the proposed "kooshball" trajectory is described by the following equations:

$$\begin{aligned} x(m) &= \cos\left(\sqrt{\tfrac{M\pi}{L}}\arcsin\big(z(m)\big) + \tfrac{2l\pi}{L}\right)\sqrt{1-z^2(m)} \\ y(m) &= \sin\left(\sqrt{\tfrac{M\pi}{L}}\arcsin\big(z(m)\big) + \tfrac{2l\pi}{L}\right)\sqrt{1-z^2(m)} \\ z(m) &= \frac{2m-M-1}{M} \end{aligned} \tag{5.8}$$

where L and M are the number of sample points required to cover the surface of a sphere by using L interleaves (spirals) and l and m are the respective control variables $l = 1...L$ and $m = 1...M$. The number of interleaves in this sampling scheme must be much smaller than the number of sampling points during a single interleave. Otherwise it will lead to a hole at the two poles if L is increased while the product LM is left unattached. To ensure continuous path linking, z will be alternating its sign from one interleave to the next. An example for a koosball trajectory is illustrated in figure 23. The red dots mark the path of a single kooshball interleave. The coordinates of the overall trajectory are calculated by multiplication of the k-space profile from eq. 5.5 with the achieved rotation values from eq. 5.8.

The overall number of profiles $N = LM$ has to be chosen to cover the surface of the kooshball sphere $O = 4\pi \cdot R^2$ with $R = k_{max}$ and with a sampling distance Δk to meet the Nyquist criterion in the k-space peripherie:

$$N = \frac{O}{\Delta k} = \frac{4\pi k_{max}^2}{\Delta k^2}$$

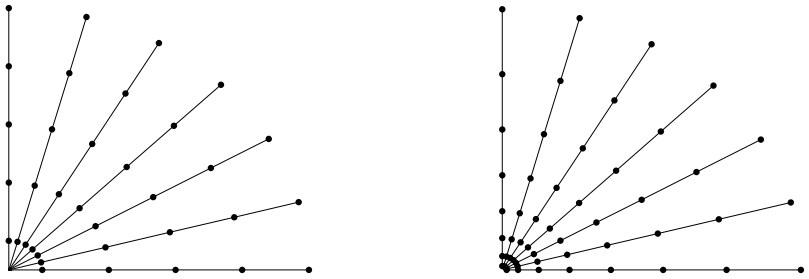

(a) $\Delta k = const$ **(b)** $\Delta k \neq const$

Figure 22.: Sampling point distribution in the center slice of k-space for (a) equidistant k-space samples achieved by sampling on the flattop of the gradient in conventional radial imaging sequences and (b) k-space intervals taking ramp sampling into account which is common in UTE imaging methods. The effect of oversampling in k-space center is increased using the ramp sampling approach.

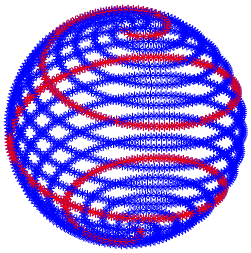

Figure 23.: Kooshball trajectory for three-dimensional uniform distribution of points on the surface of a sphere in a radial sampling scheme. The red dots mark the path of a single kooshball interleave.

Density weighting compensation: Although the sampling points on the sphere can be considered as an uniform distribution the radial sampling scheme leads to non-uniformly spaced samples in radial direction even in case of equidistant k-space sampling along the encoding direction. The distance of the samples in radial direction increases with increasing distance to the k-space center. In UTE imaging techniques this effect of non-uniform sampled k-space increases in the k-space center due to the applied ramp sampling. The weighting factors for image reconstruction compensate for this inhomogeneity in radial sampling density.

The weighting factors for the density compensation can be determined by either using a Voronoi approach [39] or estimating the impact of radial and ramp sampling to the surrounding volume of the k-space sample:

$$w_n = |\vec{k}_n|\Delta k = |\vec{k}_n|(k_n - k_{n-1}) \tag{5.9}$$

where $|\vec{k}_n|$ represents the k-space value of the n-th sampling point and describes the distance from k-space center. This part of the equation compensates for the radial profile order. Δk stands for the difference between k-space value of adjacent sampling points to compensate for non-equidistant sampling during ramp up of the readout gradient.

The sampling density weights are obtained by the volume of the Voronoi regions. Figure 24a shows the Voronoi decomposition in the center of k-space. The sampling density weights obtained by the volume of the Voronoi cells and the weighting factors achieved from equation 5.9 are represented in figure 24b. Both curves are normalized to the related maximum value of the weighting for better comparison. Since the calculation of the Voronoi volumes is very time consuming, especially for three-dimensional sampling distributions, and the results of both approaches differ barely noticeable the weighting function w is used during the image reconstruction.

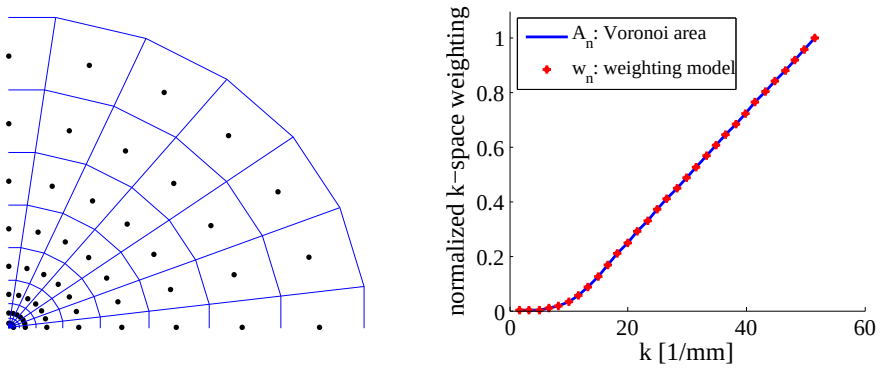

(a) **(b)**

Figure 24.: Sampling density compensation for radial ramp sampling. (a) Clipping of the sampling in the center of the k-space. Black dots represent the sampling points in k-space and the blue lines mark the borders of the Voronoi cells. (b) Weighting factors estimated by calculation of the volume of the voronoi cells (blue line) and by solving equation 5.9 (red dots).

PSF for 3D Radial Sampling Schemes

In 3D radial sampling a sphere with radius k_{max} is covered and the respective MTF can be described by

$$MTF(k) = \begin{cases} 1 & : 0 \leq |k| \leq k_{max} \\ 0 & : k_{max} < |k| \end{cases} \tag{5.10}$$

The PSF and the related impact on signal amplitude $PSF(0)$ and linewidth FWHM_{trunc} can be calculated by extending the 1D PSF of truncated k-space (section: 2.2.1) using equation 2.31 (sec. 2.2.1) to transform the centrosymmetric function:

$$PSF_{trunc}(k) = 4\pi \int_0^{k_{max}} \mathrm{sinc}(2\pi kr) k^2 \mathrm{d}r \tag{5.11}$$

$$= \frac{\sin(2\pi k_{max} r) - 2\pi k_{max} r \cos(2\pi k_{max} r)}{2\pi r^3} \tag{5.12}$$

$$PSF_{trunc}(0) = \frac{4}{3}\pi k_{max}^3 \tag{5.13}$$

$$\mathrm{FWHM}_{trunc} = 1.59\Delta r \tag{5.14}$$

For an expression in terms of voxel size Δr, the FWHM was normalized by a factor of 2π to compensate for the normalized linewidth of the sinc-function.

5.1.3. Signal Spoiling

The residual transverse magnetization at the end of a pulse sequence produces spurious signals which interfere with the desired signal in subsequent acquisitions and therefore causing image artefacts. There are two options to get rid of these undesired signals. The first one is to repeat the measurement sequence in a time interval TR which is at least four or five times higher than the maximum T_2 value available in the measuring object. During this time interval the signal decays nearly to zero and minimizes the effect of signal interference. This approach leads to a rapid increase in measurement time especially for 3D radial imaging and is therefore not applicable for dental MR. The second one is signal spoiling. Therefore a so called spoiler gradient is applied at the end of the sequence to dephase the residual transverse magnetization in the direction of the applied gradient. The area of the spoiler gradient is very large to ensure an adequate signal cancellation inside a voxel. The phase which is introduced by the spoiling gradient $\vec{G}_{sp}(t)$ is given by

$$\Psi = \gamma \int \vec{G}_{sp}(t)\vec{r}\,dt = \gamma r A_{sp}$$

where A_{sp} is the area under the spoiler gradient. A large area of the spoiler gradient considerably attenuates the transverse magnetization. In the special case when the phase dispersion across a voxel

$$\Delta\Psi = \gamma \Delta r A_{sp}$$

becomes a multiple of 2π, the total transverse magnetization becomes zero. For detailed information refer to [3].

5.1.4. Impact of Signal Imperfections

System non-idealities influence the behaviour of UTE imaging sequences differently than in conventional MR imaging techniques due to its radial acquisition scheme and the non-equidistant k-space sampling in the center region. In UTE imaging each recorded signal represents a half echo. A full projection of the image is obtained by combining two opposite profiles together. Therefore non-idealities influence the k-space data always in a radial center-out manner. This section investigates the impact on image quality due to timing imperfections of the gradient channels, gradient waveform distortions due to eddy currents and non-idealities in the gradient power supply, T_2^* relaxation during readout and the effect of zero order off-resonances.

Gradient Delays

System imperfections as channel delays cause uncertainty in echo position. In cartesian imaging techniques gradient delays lead to a shift of the whole k-space in readout direction and therefore, add according to the Fourier theorem, a linear phase to the reconstructed image. In radial imaging techniques the readout direction is subsequently changed and

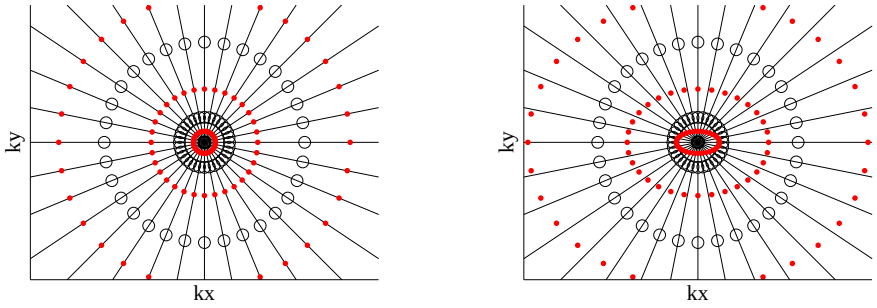

(a) $T_{D,x} = T_{D,y}$ **(b)** $T_{D,x} = 1.4 \cdot T_{D,y}$

Figure 25.: Center part of k-space trajectory for radial center-out sampling for (a) k-space shift due to identical gradient timing of the x- and y-axis and for (b) k-space shift due to different gradient timing errors for the x- and y-axis. The ideal trajectory is represented by the black circles and the delayed k-space samples are represented by the red dots.

therefore the shift of the k-space center depends on the actual readout direction. To overcome the challenge of non-uniform k-space a first order phase-correction [38] of each projection during reconstruction can be applied without any need for additional calibration scans. Other than in conventional radial imaging, UTE does not provide a full projection with a defined echo peak top. Therefore the achieved k-space center of a complete projection is shifted symmetrical along the readout direction backwards or towards the ideal k-space center.

The delay of the system can be considered rather as missmatch in gradient and acquisition timing than as a fixed delay of the gradient amplifiers. Every adjustment of the sequence settings that results in a change of the gradient amplitude, length and/or slewrate leads to an adoption of the sampling interval and/or duration of the sampling window and therefore influences the sequence timing. This dependency on the sequence timing requires an adjustment of gradient delay for every change in sequence parameters even in case of a well calibrated system.

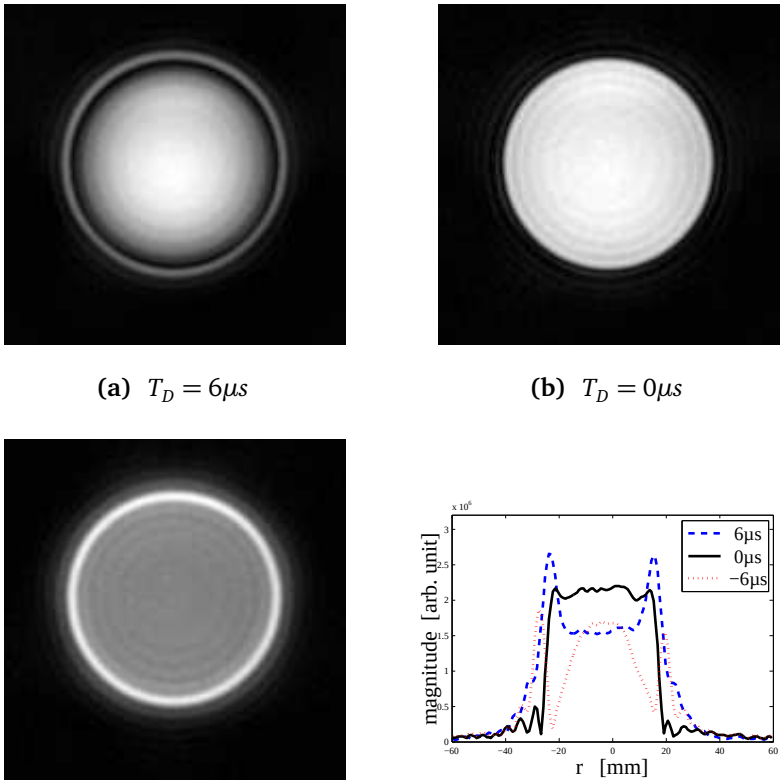

(a) $T_D = 6\mu s$ **(b)** $T_D = 0\mu s$

(c) $T_D = -6\mu s$ **(d)** profiles

Figure 26.: Impact of gradient delay on the reconstructed image for (a) positive gradient delay $T_D = 6\mu s$, (b) no gradient delay $T_D = 0\mu s$, and (c) negative gradient delay $T_D = -6\mu s$. (d) Profile of the different gradient delays through the center of the phantom. While a positive delay decreases the signal intensity inside the phantom and brights up the edge, a negative delay leads to a repetition of the edge and a smoothing of the phantom shape.

Figure 25 shows a sampling grid with equal gradient delays (fig. 25a) and with different gradient delays (fig. 25b) for the physical gradient axes in x- and y-direction. The grid for ideal gradient behaviour is represented by the black circles while the k-space samples achieved with delayed gradients are marked by the red dots.

The effect of an improper selection of gradient delay on the reconstructed image is shown in figure 26. A positive gradient delay results in a significant bright signal around the phantom and a dark center (fig. 26a). If the trajectory delay is only slightly too large, a bright rim on the phantom is visible. A negative gradient delay leads to a replication of the edges and a blurring of the inside (fig. 26c).

Since UTE acquires only one half of the echo, it is not possible to detect the echo top and correct for echo peak shift. To ensure perfect image quality the related delay for the chosen sequence has to be determined for every set of new scan parameters.

Waveform Distortion due to Eddy Currents

Gradient waveform distortions lead to a time varying shift of the k-space sampling points and cause severe degradation of image quality. The additional gradient fields due to eddy currents are build up during the ramp up of the gradient (2.3.2) and therefore highly affect the sampling of the k-space center in UTE imaging. Also the decaying gradient fields during the constant part of the gradient lead to a time dependent mismatch of the k-space samples and the estimated k-space trajectory. In the presence of eddy currents in read out direction the k-space center appears later than expected.

The effect of eddy currents can be described by long and short term time constants [3]. Since B_0 components in fact cause unwanted phase shift but do not affect the k-space trajectory, only the linear eddy current terms are considered. The rate of eddy current build up is related to the slewrate of the applied gradient which can be calculated according to 5.4:

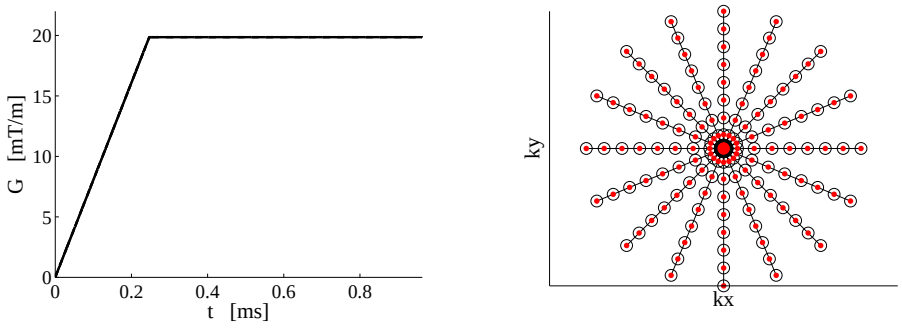

(a) $\tau_{ec} << t_{slope}$

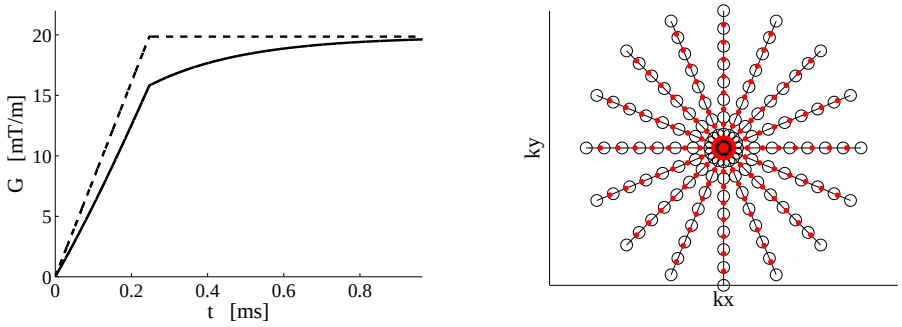

(b) $\tau_{ec} = t_{slope}$

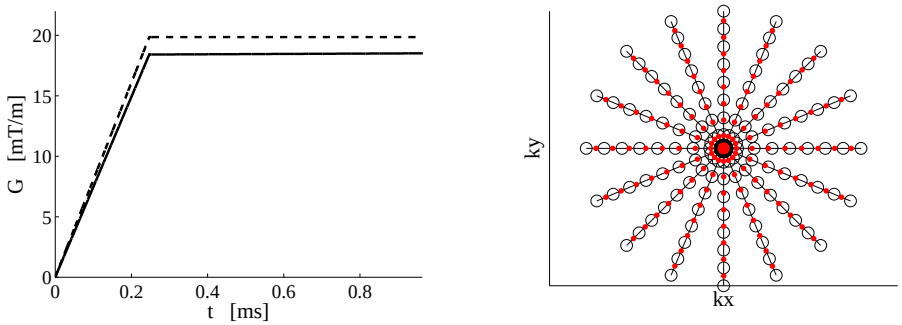

(c) $\tau_{ec} >> t_{slope}$

Figure 27.: Impact of eddy currents on the gradient waveform (left) and on the related sampling grid (right). (a) Ultra-short time constants ($\tau_{ec} << t_{slope}$) can be regarded as a delay of the gradient waveform. (b) Time constants in the order of the gradient slope ($\tau_{ec} = t_{slope}$) shift every k-space point by an time varying amount of k-space $\Delta k_{ec}(t)$. (c) Long term time constants ($\tau_{ec} >> t_{slope}$) decrease the gradient strength by the α_{ec} and can be regarded as a scaling of the k-space coordinates.

$$\frac{dG}{dt} = \begin{cases} \frac{G_{RO}}{T_{slope}} & : 0 \leq t \leq T_{slope} \\ 0 & : T_{slope} < t \end{cases} \tag{5.15}$$

The eddy current induced gradient field for a single eddy current time constant can be obtained by using equations 2.37, 2.39, and 5.15:

$$G_{ec}(t) = \begin{cases} -\frac{G_{RO}}{T_{slope}} \alpha\tau(1 - e^{-\tau/t}) & : 0 \leq t < T_{slope} \\ -\frac{G_{RO}}{T_{slope}} \alpha\tau(1 - e^{-\tau/T_{slope}}) & : t = T_{slope} \\ G_{ec}(T_{slope}) e^{-\tau/t} & : T_{slope} < t \end{cases} \tag{5.16}$$

The effect of different time constants on the gradient waveform and the related k-space grid are illustrated in figure 27. The effect of very short time constants during ramp up of the gradient results in:

$$G_{ec}(t) \approx -\frac{G_{RO}\alpha\tau}{T_{slope}}$$

Due to the usually high slewrates and the related short slope durations, ultra-short time constants are in the range of a few ten microseconds. Therefore the eddy current induced field decays really fast after the ramp up of the gradient and has nearly no effect during the flattop of the encoding gradient (fig. 27a). Hence, the effect of ultra-short eddy current time constants can be considered at a first order as a delay $T_D = \alpha\tau$ of the gradient

waveform. For long term constants (fig. 27c) the linear eddy current at the end of the ramp can be approximated to:

$$G_{ec}(t = T_{slope}) \approx -G_{RO}\alpha\,.$$

Due to the usually short readout duration compared to the time constant, the eddy current induced field can be considered as a time constant function during the flattop of the encoding gradient. Therefore the sampling distance Δk is reduced but time independent and the effect can be considered as a scaling of the whole k-space. A common approach for linear eddy current reduction is to adapt the current gradient waveform in such way that the preemphasis distortion cancels the subsequent eddy current distortion. Therefore an accurate characterization of eddy currents is mandatory and can lead to a reduction of eddy currents by one to two orders of magnitude [3].

T_2^* Induced Blurring

As described in section 2.2.1 any factors that modify the sampling data can be described by a k-space filter and therefore by the the modulation transfer function (MTF) of the system. Besides signal modulation by truncated k-space and discrete sampling also the effect of T_2^* relaxation on the change of signal amplitude can be modelled as a filter. The signal obtained by considering the additional filter is given by

$$MTF_{T_2^*} = H_{ws}(k) \cdot H_{T_2^*}(k)$$

and the overall PSF can be written as a convolution:

$$PSF_{T_2^*} = h_{ws}(r) * h_{T_2^*}(r)$$

For a center-out radial acquisition scheme the MTF filter and the related PSF result in isotropic functions and the time depended signal relaxation can be expressed by the filter function

$$H_{T_2^*}(t) = e^{-\left(\frac{|t|}{T_2^*}\right)}.$$

The corresponding k-space depended filter can be calculated from the equation above and eq. 5.6:

$$H_{T_2^*}(k) = \begin{cases} e^{-\left(\sqrt{\frac{4\pi T_{slope}}{\gamma G_{RO}}|k|}\frac{1}{T_2^*}\right)} & : 0 \leq t \leq T_{slope} \\ e^{-\left(\frac{2\pi}{\gamma G_{RO}}\frac{|k-k_{slope}|}{T_2^*}\right)} & : T_{slope} < t \end{cases} \tag{5.17}$$

where $k_{slope} = \frac{\gamma}{4\pi} G_{RO} T_{slope}$ is the k-space value at the end of the slope. In the case of pure flattop sampling, the PSF can be obtained analytical while no closed form of the Fourier transform of a square function and therefore for the gradient ramp up is known to the author. For detailed information of the effect of ramp sampling on the amplitude and the FWHM of the PSF refer to chapter 6.

For numerical simulations the slope duration was defined as a ratio of the acquisition duration:

$$T_{slope} = f_{slope} \cdot T_{ACQ}. \tag{5.18}$$

In case of $f_{slope} = 1$, the ramp up of the gradient will last over the whole acquisition time. To get a realistic comparison of different ramp durations the same gradient amplitude for the flattop region was assumed and the acquisition duration was adjusted to cover the same k-space area. For better estimation of the FWHM the k-space was zero filled by factor 4 to obtain subpixel resolution of the PSF. The acquisition duration for different slope factors results in:

$$T_{ACQ} = \frac{2\pi k_{max}}{\gamma G_{RO}} \frac{1}{(1 - 0.5 \cdot f_{slope})} \tag{5.19}$$

where the first term represent the acquisition duration for sampling during constant gradient amplitude and the second term accounts for the duration of the gradient ramp related to the chosen ramp factor. For simulations the T_2^* relaxation constant was defined as a ratio of the acquisition duration for the shortest applied gradient ramp:

$$T_2^* = f_{T_2^*} \cdot T_{ACQ,min} \tag{5.20}$$

Figure 28 shows the T_2^* dependency of the FWHM and the PSF amplitude for different settings of the slope duration. The ratios between ramp up and constant gradient are chosen to $f_{slope} = 0.125/\,0.25/\,0.5$, and 1. Both parameters are plotted as functions of the ratio between sampling duration and relaxation time, where the ratio is related to the case with the shortest acquisition duration $T_{ACQ,min}$. The increase in ramp factor f_{slope} leads to a higher loss in signal amplitude and increased blurring of the object. While the FWHM stays nearly the same for T_2^* values lower than half of the minimal acquisition duration, the PSF amplitude is also affected for T_2^* in the order of T_{ACQ} and higher. The representation of tissues with transverse relaxation times in the order of the acquisition duration and shorter are exemplarily shown in figure 29 for the relaxation factors of $f_{T_2^*} = 1/\,0.5/\,0.125$ compared to the ideal case of no signal relaxation. While the tissues with T_2^* decay for

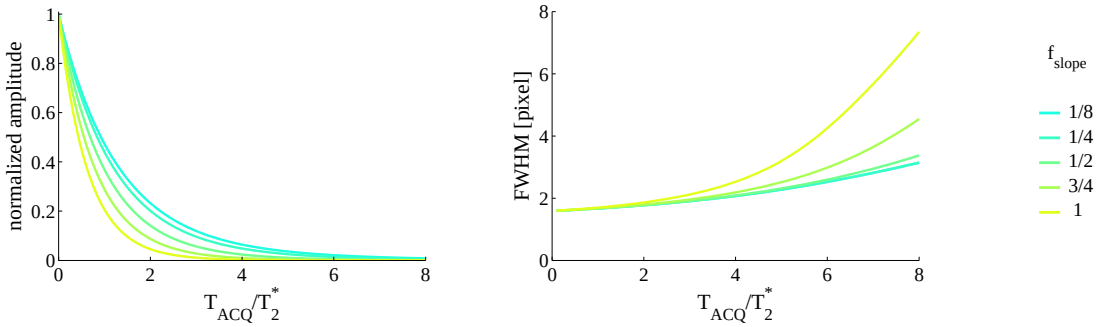

(a) PSF(0) **(b)** FWHM

Figure 28.: (a) Amplitude and (b) width of the PSF representing T_2^* relaxation and sampling window truncation. The parameters are plotted for different ratios between ramp up and constant part of the readout gradient as a function of the ratio between minimal sampling duration $T_{ACQ,min} = T_{ACQ}(f_{slope} = 0.125)$ and the relaxation times.

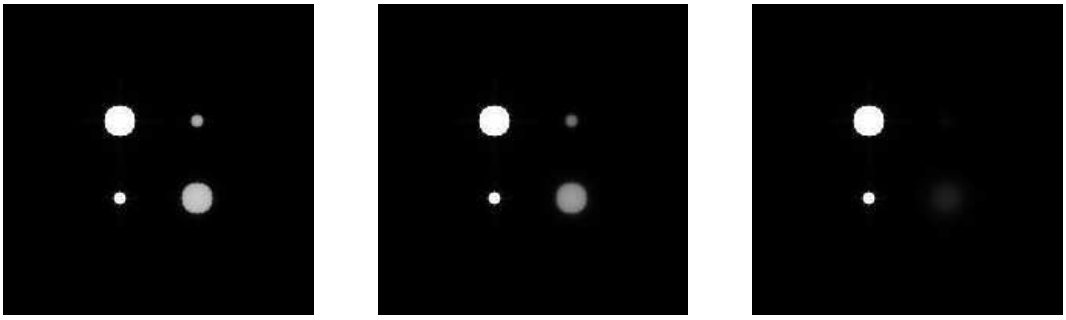

(a) $T_2^* = T_{ACQ}$ **(b)** $T_2^* = 1/2 \cdot T_{ACQ}$ **(c)** $T_2^* = 1/8 \cdot T_{ACQ}$

Figure 29.: Reconstructed images for simulated k-space data for different objects neglecting (left row) and considering (right row) T_2^* relaxation for a slope duration of $T_{slope} = 0.5T_{ACQ}$. Simulations were performed for different T_2^* values related to the corresponding acquisition duration.

the former cases can be clearly identified in the images, the signal from tissues with T_2^* in the order of $1/8$ of the acquisition duration is virtual zero. The SNR for the given scan parameters can be obtained from the total PSF amplitude weighted by the square root of the sampling duration [37]. Simulations result in better SNR for longer ramp duration in the case of $T_{ACQ} \approx T_2^*/2$ or higher. For shorter T_2^* values the SNR still shows higher values for decreasing ramp duration. Assuming an amplitude of $20mT/m$ for the constant part of the readout gradient and a desired scan resolution of $0.8mm$, the reference acquisition duration results in $T_{ACQ,min} \approx 0.8ms$ for a slope duration of $T_{slope} = 0.1ms$, which is equal to a slewrate of $200mT/ms$. For the given parameters the simulated T_2^* values are in the range of $100\mu s$ and $3.2ms$.

Off-resonance Induced Blurring

According to the filter calculation for T_2^* decay, the influence of a zero order off-resonance f_{off} during acquisition can also be expressed as a filter:

$$H_{off}(t) = e^{i\omega_{off}t}$$

with respective k-space representation:

$$H_{off}(k) = \begin{cases} e^{i\left(\omega_{off}\sqrt{\frac{4\pi T_{slope}}{\gamma G_{RO}}|k|}\right)} & : 0 \leq t \leq T_{slope} \\ e^{i\left(\frac{2\pi\omega_{off}}{\gamma G_{RO}}|k-k_{slope}|\right)} & : T_{slope} < t \end{cases} \tag{5.21}$$

Considering only off-resonance effects and neglecting the effect due to windowing and discrete sampling the MTF filter consists of a phase term only and is according to section 2.2.1 defined as a constant function over the entire time domain. For numerical simulations the same requirements are used as for T_2^* simulations regarding duration of gradient slope T_{slope} and acquisition duration T_{ACQ}. The off-resonance f_{off} is defined as a fraction $f_{f_{off}}$ of the acquisition duration for the shortest applied gradient ramp:

$$f_{off} = f_{f_{off}} \cdot \frac{1}{T_{ACQ,min}} \tag{5.22}$$

Figure 30 shows the off-resonance dependence of the FWHM, FWTM and the amplitude of the PSF for different settings of the slope duration. The ratio between ramp up and constant gradient are chosen to $f_{slope} = 0.125/\,0.25/\,0.5$, and 1. All parameters are plotted as functions of the sampling duration and offset frequency, where the factor is related to the case with the shortest acquisition duration $T_{ACQ,min}$. The FWHM and PSF amplitude for slope fraction $f_{slope} \leq 0.5$ stays nearly the same. In the case of pure ramp sampling - with acquisition duration of nearly twice $T_{ACQ,min}$ - the loss in signal amplitude in the range of $f_{f_{off}} = 0$ and $f_{f_{off}} = 1.5$ result in up to 12% compared to $f_{slope} = 0.125$. Simultaneously the linewidth of the main lobe represented by the FWHM decreases, which in principle indicates less image blur for high ramp factor. In opposition to the findings of the FWHM the spatial extend of the PSF at the tenth maximum increase with increasing ramp fraction and therefore leads to increased blurring of the object. Therefore the shape of the PSF caused by phase accumulation during acquisition is characterised by a small main lobe and high impact of the side lobes.

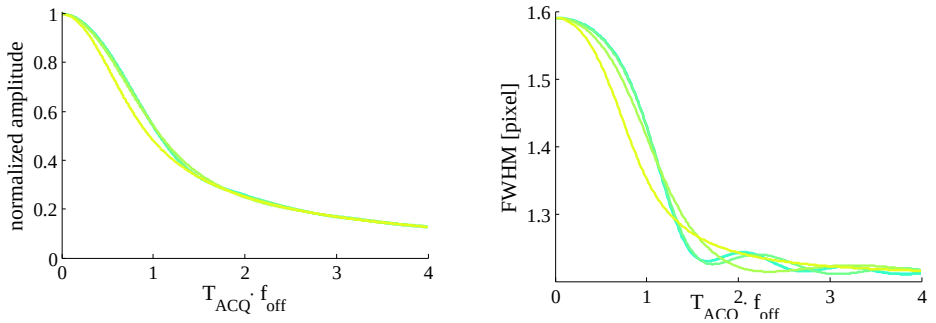

(a) PSF(0) **(b)** FWHM

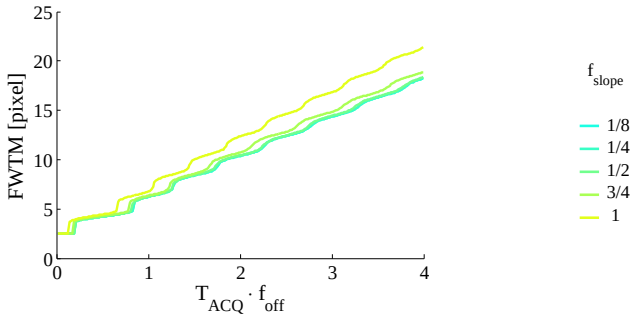

(c) FWTM

Figure 30.: (a) Amplitude, (b) full width at half maximum, and (c) full width at tenth maximum of the PSF which represents the presence of an offset frequency during acquisition and k-space sampling truncation. The parameters are plotted for different ratios between ramp up and constant part of the readout gradient as a function of the factor between minimal sampling duration $T_{ACQ,min} = T_{ACQ}(f_{slope} = 0.125)$ and the off-resonances.

Assuming same sequence settings as for the T_2^* simulations ($G_{RO} = 20mT/m$, $S_{RO} = 200mT/ms$, $\Delta\vec{r} = 0.8mm$, and $T_{ACQ,min} \approx 0.8ms$) the frequency shift between water and fat results in $f_{off} \approx 0.35/T_{ACQ,min}$ for a main magnetic field of $B_0 = 3T$, $f_{off} \approx 0.8/T_{ACQ,min}$ for $B_0 = 7T$ and $f_{off} \approx 1.1/T_{ACQ,min}$ for $B_0 = 9.4T$. The impact on image quality for different slope durations and hence different readout durations is shown in figure 31, considering a offset frequency which corresponds to the water-fat difference at $3T$. With

increasing slope factor and related longer acquisition duration a halo builds up around the off-resonant tissue.

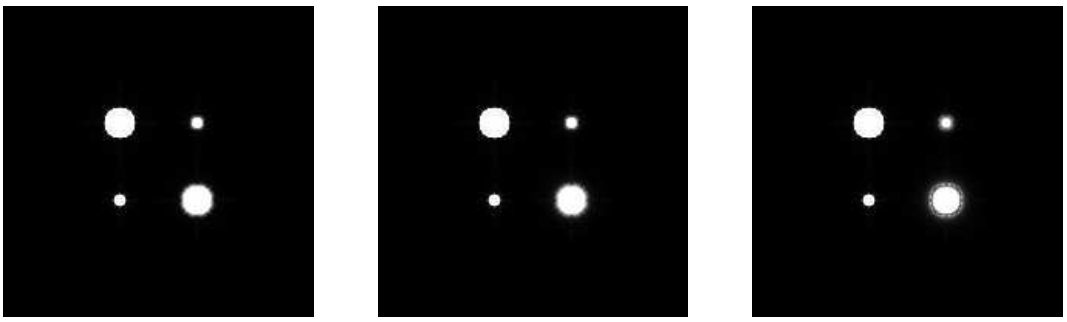

(a) $T_{slope} = 1/8 \cdot T_{ACQ}$ **(b)** $T_{slope} = 1/2 \cdot T_{ACQ}$ **(c)** $T_{slope} = T_{ACQ}$

Figure 31.: Reconstructed images of simulated k-space data for different objects neglecting (left row) and considering (right row) phase accumulation of a off-resonance factor $f_{off} = 0.35/T_{ACQ,min}$. Simulations were performed for different slope durations related to the corresponding acquisition duration.

5.2. Signal Corrections

In UTE imaging the FID signal is sampled from the central to the outer part of the k-space during ramp up of the readout gradient. Therefore the sequence is very sensitive to trajectory errors which are caused by gradient and system delays and waveform distortions due to eddy currents and gradient system imperfections. The imperfections of the gradient system translate into inconsistencies of the acquired k-space information and degrade the image quality. These k-space errors can be corrected when having a precise knowledge of the actual gradient waveform, which can be achieved by mapping the distorted k-space trajectory. This section investigates the influences of system non–idealities on the applied trajectory mapping approach due to time-varying and time-constant changes in the magnetic field. Two approaches are introduced to achieve adequate image quality by

knowing the accurate gradient waveform. The first approach doesn't use any hardware assisted correction approaches to compensate for delayed and waveform distorted gradients and uses the mapped k-space trajectory during the reconstruction process. For the second approach common gradient waveform corrections like gradient waveform pre-emphasis (GPE) and gradient channel delays (GCD) are used for instantaneous trajectory correction during the measurement and a model-based approach is applied to replicate the still present non-idealities of the system.

5.2.1. Trajectory Mapping

While a number of methods exist for measuring and correcting trajectories, the approach proposed by Duyn et al. [13] has become a popular choice for its accuracy without the need for specialized phantoms . For most sequences, the trajectory measurements can be derived using this method only along the three physical gradients while all other encoding steps are assumed to be a linear combination of these gradients [10]. This is possible because the waveforms on any given axis are scaled versions of the reference waveform.

To compensate for deviation of the theoretical gradient waveform Duyn proposed a simple method to measure the actual k-space trajectory by a slight modification of the desired imaging pulse sequence. For the trajectory mapping approach a thin slice at known distance D_r to the isocenter is excited and the spatial encoding gradient is played out orthogonal to the slice. This means that readout and slice selection gradient are applied along the same physical gradient axes. The readout gradient introduces a spatial variation in resonance frequency which leads to a phase accumulation that corresponds to the actual k-space trajectory:

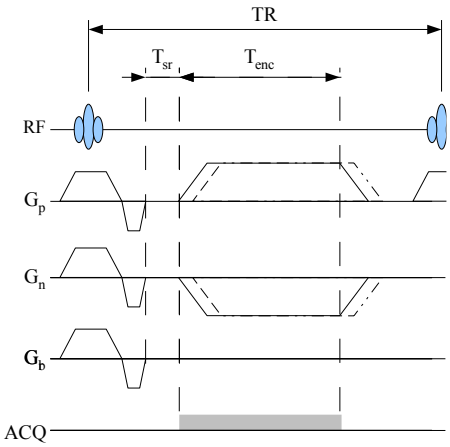

Figure 32.: Pulse sequence used to map the trajectories. Slice selection and readout gradient are performed on the same physical gradient axis. Data are acquired for positive and negative readout gradient to consider for different eddy current behaviour and without readout gradient to achieve the baseline phase caused by system imperfections. Dashed line indicates the delayed gradient waveform.

$$\Phi_r = \int_0^t \gamma G_{RO}(t)\, D_r \, \mathrm{d}t = 2\pi \, D_r \, k_{RO}(t) \tag{5.23}$$

where $G_{RO}(t)$ is the gradient under test. The trajectory $k_{RO}(t)$ can be determined by normalizing the acquired and unwrapped phase signal by D_r.

Equation 5.23 is a simplified representation of the phase accumulation during data acquisition, considering only phase evolution due to the encoding gradient without any effects of signal phase due to imperfections. A detailed expression of equation 5.23 regarding signal imperfections is given by:

$$\begin{aligned}\Phi_r =& D_r \int_0^t \gamma G_{RO,D}(t)\,\mathrm{d}t + \\ & D_r \int_0^t \gamma G_{ec}(t, G_{RO,D})\,\mathrm{d}t + \int_0^t \gamma B_{0,ec}(t, G_{RO,D})\,\mathrm{d}t + \\ & D_r\, \gamma G_{off}\, t + \gamma B_{0,off}\, t + \\ & D_r\, \gamma G_{off}\, T_{start} + \gamma B_{0,off}\, T_{start} + \\ & \Phi_{sl}(G_{sl})\end{aligned} \tag{5.24}$$

The first three terms consider for readout gradient imperfections as delayed gradient waveform (first term) and additional magnetic fields due to zero and first order eddy currents ($B_{0,ec}$,G_{ec}) caused by the readout gradient. Line three represents the impact on the phase caused by zero and linear order off-resonances during signal acquisition. The accumulated phase at the start of acquisition due to these off-resonances is given by $D_r G_{off} \cdot T_{start}$ and $B_{0,off} \cdot T_{start}$. The phase term Φ_{sl} represents the initial phase at start of acquisition caused by residual B_0 eddy currents of the slice selection gradient and by uncompensated area of the slice selection gradient due to linear order off-resonances and eddy currents.

To compensate for system imperfections which are not caused by the readout gradient an additional reference scan with encoding gradients switched off ($G_{RO,D} = 0$) is applied (fig. 32). During this scan the baseline phase is achieved:

$$\begin{aligned}\Phi_{baseline} =& D_r\, \gamma G_{off}\, t + \gamma B_{0,off}\, t + \\ & D_r\, \gamma G_{off}\, \mathrm{TE} + \gamma B_{0,off}\, \mathrm{TE} + \\ & \Phi_{sl}\end{aligned} \tag{5.25}$$

The difference of the data phase only includes effects caused by the readout gradient itself:

$$\Delta\Phi_r(D_r,G_{RO,D}) = \Phi_r - \Phi_{baseline} = \tag{5.26}$$

$$D_r \int_0^t \gamma G_{RO,D}(t)\,\mathrm{d}t +$$

$$D_r \int_0^t \gamma G_{ec}(t,G_{RO,D})\,\mathrm{d}t + \int_0^t \gamma B_{0,ec}(t,G_{RO,D})\,\mathrm{d}t$$

To achieve the trajectory along a single physical gradient channel, the sum of the repeated experiments is calculated and the phase difference with encoding gradient switched on and off is calculated to evaluate the phase progression caused by the gradient. In the next step the phase evolution is unwrapped to obtain a continuous function which is a scaled version of the k-space trajectory. The phase unwrapping algorithm from Matlab [32] was used which calculates the phase difference between adjacent sampling points and transforms values greater than π to their 2π complements. Figure 33 shows the measurement results for positive and negative readout gradient, for the baseline phase and for the baseline corrected phase accumulation.

To minimize unwanted phase wraps the choice of the distance of the slice location from the isocenter is very important. Exciting slices near the edge of the FOV leads to a phase accumulation of π between adjacent k-space sampling points. In the presence of noise this would be a challenge for the phase unwrapping algorithm. Choosing a slice near the isocenter leads to a slower phase accumulation and the phase unwrapping is much easier. Figure 34 shows the impact of slice distance to the isocenter on the velocity of phase accumulation.

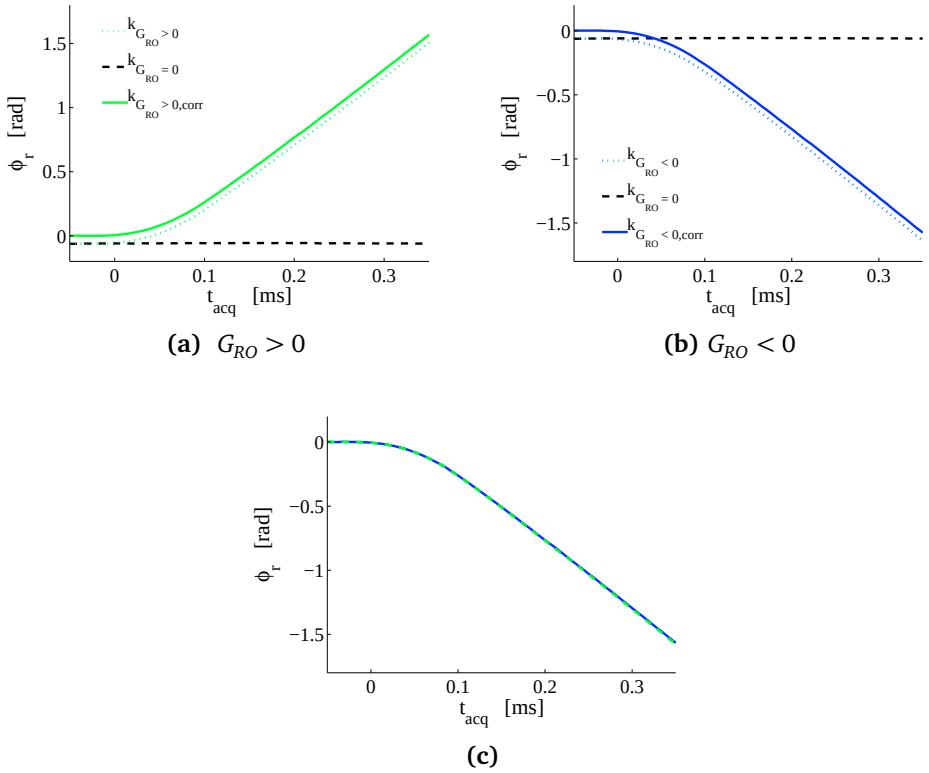

(a) $G_{RO} > 0$ **(b)** $G_{RO} < 0$

(c)

Figure 33.: Correction of the base line drift (dashed black) for (a) positive and (b) negative encoding gradient. Dotted lines represent the measured phase evolution with gradient under test switched on while coloured solid lines represent the baseline corrected signal. (c) Comparison of k-space trajectory for positive (dashed green) and negative (dashed blue) encoding gradient.

Another important scan parameter is the choice of slice thickness. Using slice thickness's much greater than the desired scan resolution leads to signal dephasing within the slice which then causes signal drop-outs. Figure 35 illustrates the impact of slice thickness on the signal cancellation due to in-slice dephasing. To avoid this effect the slice thickness is chosen to be equivalent to the desired resolution. If the choice of slice thickness leads to unacceptable SNR levels, signal averaging has to be performed.

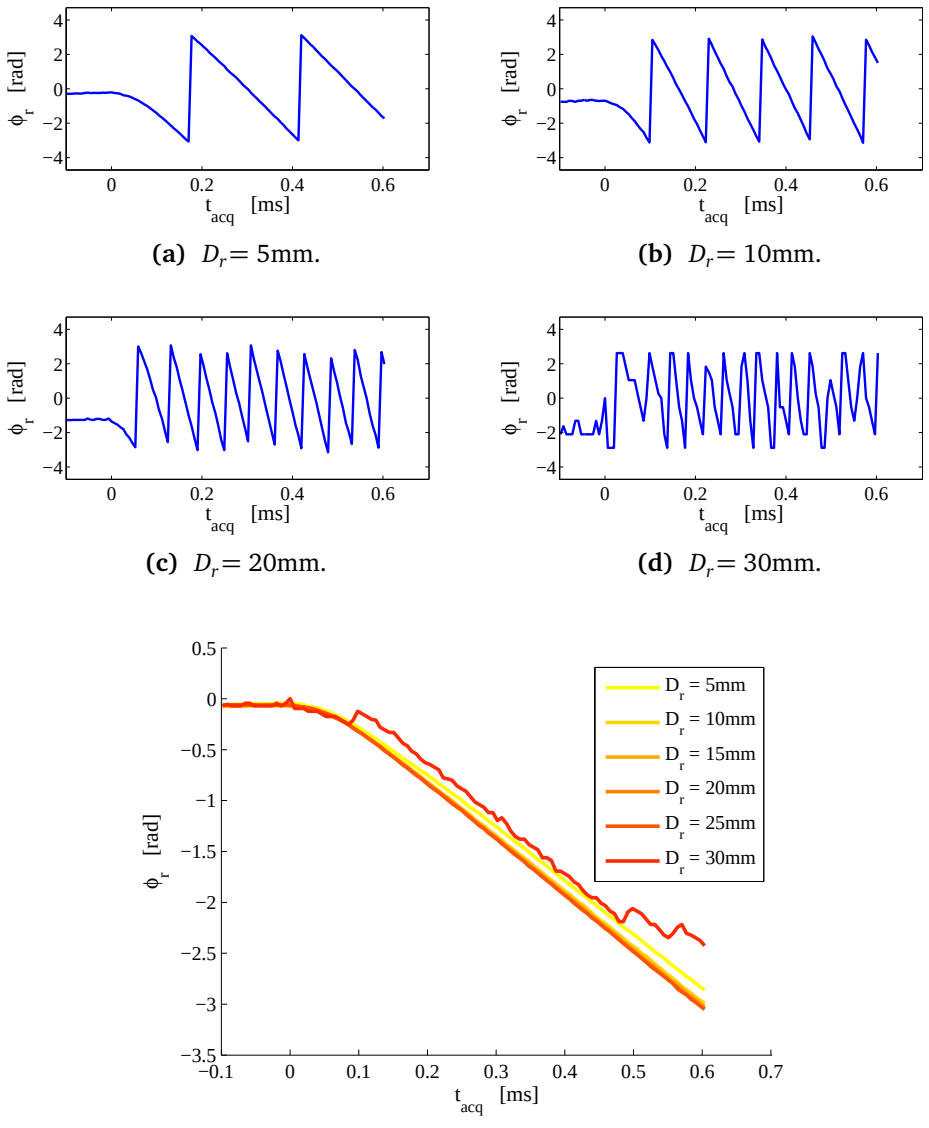

(a) D_r= 5mm. **(b)** D_r= 10mm.

(c) D_r= 20mm. **(d)** D_r= 30mm.

(e)

Figure 34.: (a) - (d) Phase evolution for different slice locations regarding phase-unwrapping. (e) Calculated trajectory for different slice locations. For a slice distance of 30mm (3/4 of FOV) to the isocenter the phase unwrapping doesn't work sufficiently any more.

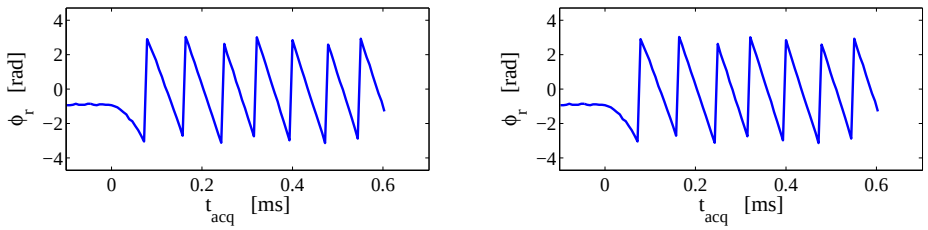

(a) Δz= 0.5mm.

(b) Δz= 1mm.

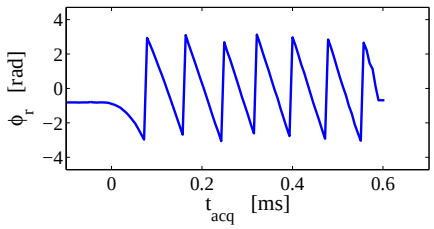

(c) Δz= 2mm.

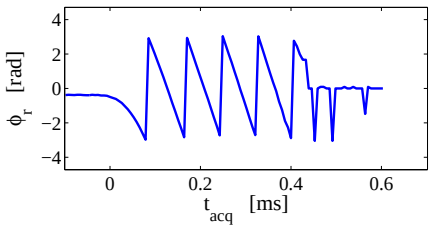

(d) Δz= 3mm.

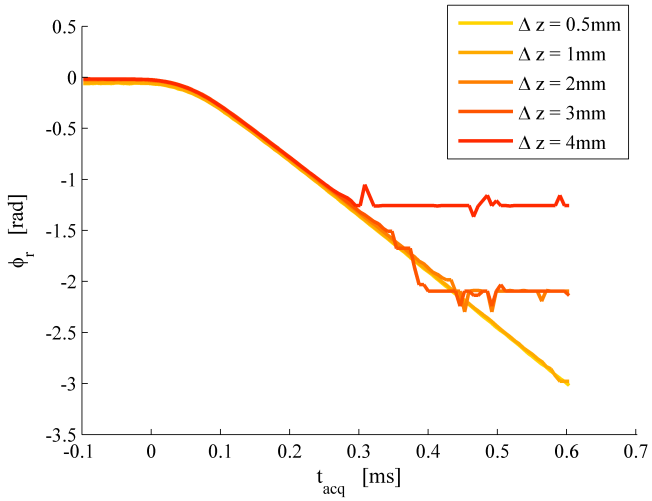

(e)

Figure 35.: (a) - (d) Phase evolution for different slice thicknesses regarding phase-unwrapping. (e) Calculated trajectory for different resolution in slice selection direction. Dephasing within the slice causes signal drop-outs if the slice thickness is much higher than the scan resolution.

The utilized trajectory mapping approach captures the overall phase evolution and does not distinguish between zero and first order effects. While in imaging sequences the linear parts of the eddy currents have an impact on the real k-space position, zero order eddy currents only affect the phase of the data. To achieve the real k-space trajectory one has to compensate the effect of zero eddy currents on the phase evolution. Since B_0 eddy currents are not spatial depended and therefore do not experience a scaling by the distance of the slice to the isocenter this can be done by measuring the phase evolution of slices with different D_r and subtracting the signals:

$$\begin{aligned}\Delta\Phi_r &= \Delta\Phi_r(D_{r,1},G_{RO,D}) - \Delta\Phi_r(D_{r,2},G_{RO,D}) \\ &= (D_{r,1}-D_{r,2})\left[\int_0^t \gamma G_{RO,D}(t)\,\mathrm{d}t + \int_0^t \gamma G_{ec}(t,G_{RO,D})\,\mathrm{d}t\right]\end{aligned} \tag{5.27}$$

To obtain the actual k-space trajectory from the measurement, the unwrapped phase signal has to be scaled by a factor $\frac{1}{D_r}$ according to equation 5.23.

Impact of Zero and First Order Off-resonances on Slice Position

In the previous section it was shown that the impact of off-resonances during signal acquisition can be compensated for by a simple baseline correction using a reference scan without applying the readout gradient. The impact of off-resonances which are present during the slice selection process is not corrected by this approach and leads to uncertainty in slice position. The effects of B_0 and linear off-resonances during excitation to the mapped trajectory are analysed in this paragraph.

When exciting a slice that does not pass through the gradient isocenter, its position is given by the offset frequency Δf_{sl} with respect to the current center frequency f_0 and by the amplitude of the simultaneous applied slice selection gradient G_{sl} (see chapter 2.1.2):

$$D_r(\Delta f_{sl}, G_{sl}) = \frac{2\pi\Delta f_{sl}}{\gamma G_{sl}} = \frac{2\pi\left(f_{sl} - f_0\right)}{\gamma G_{sl}} \tag{5.28}$$

An impreciseness in the center frequency of the amount Δf shifts the slice by a factor $x_{0,sl} = \Delta f / \Delta f_{sl}$:

$$\begin{aligned} D_r(\Delta f_{sl}, G_{sl}) &= \frac{2\pi\left(f_{sl} - (f_0 + \Delta f)\right)}{\gamma G_{sl}} \\ &= \frac{2\pi\left(\Delta f_{sl} - \Delta f\right)}{\gamma G_{sl}} = \frac{2\pi\Delta f_{sl} \cdot (1 - x_{0,sl})}{\gamma G_{sl}} \end{aligned} \tag{5.29}$$

To compensate for B_0 off-resonances a pair of opposed slices is selected with a fixed slice selection gradient and RF modulation frequencies of opposed sign (fig. 36). Therefore the absolute position of each slice is still unsettled but the spacing of the slices is two times the desired distance to the isocenter:

$$\begin{aligned} D_r &= \frac{D_r(\Delta f_{sl}, G_{sl}) - D_r(-\Delta f_{sl}, G_{sl})}{2} \\ &= \frac{2\pi\Delta f_{sl}}{\gamma G_{sl}} \end{aligned} \tag{5.30}$$

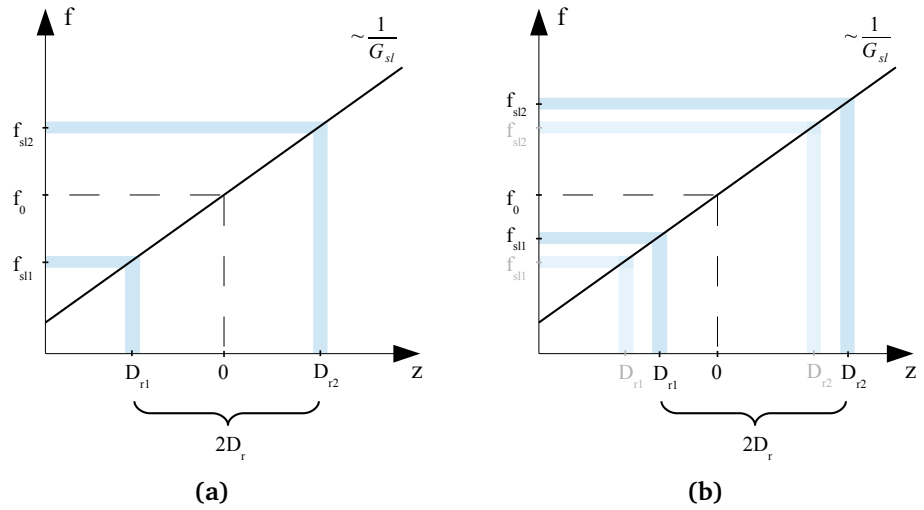

Figure 36.: Impact of zero order off-resonances on the slice selection process. The absolute position of the slice distance changes in the presence of zero order off-resonances but the distance between two slices with equal gradient amplitude and opposed slice selection frequency is precisely known.

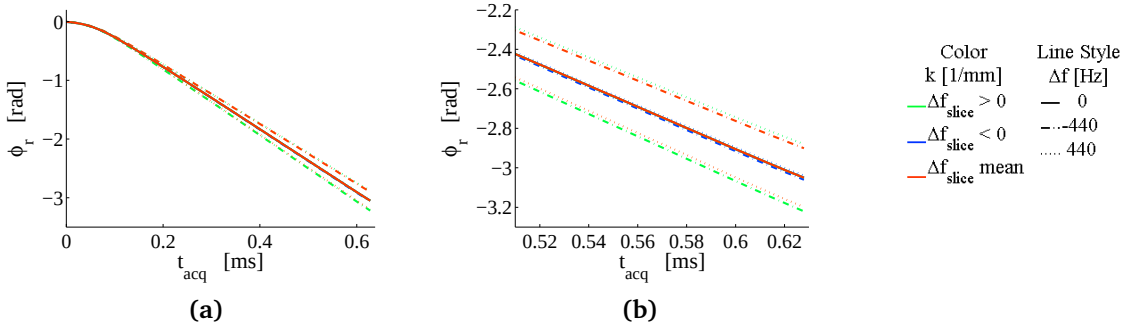

Figure 37.: Impact of biased slice locations on the mapped k-space trajectory caused by a zero order off-resonance.

If the trajectory mapping approach uses only a single slice for each axis with same settings for RF and slice selection gradient, a B_0 off-resonance compresses or stretches the k-space and decreases / increases the respective resolution of the reconstructed image in all three directions for the same amount and is not clearly visible at a first view. Using slices at different distance D_r with related different carrier frequencies of the RF pulse (e.g. for SNR improvement) leads to a k-space compression or stretching of different quantities in the three directions. The non-uniform displacement of k-space values for the different measurements axes leads to a degradation in image quality.

The influence on accuracy of the mapped trajectory by the presence of B_0 off-resonances during slice selection is shown in figure 37. Assuming an offset frequency of $\Delta f = 440Hz$ and a slice selection gradient of $G_{sl} = 20mT/m$, the mapped trajectory shows a deviation from the expected trajectory of over 5%. The deviation decreases with increasing gradient amplitude and increasing D_r. For a readout gradient amplitude of $G_{RO} = 20mT/m$ this is equal to an inaccuracy of $\pm 1mT/m$ in gradient amplitude. Applying the introduced correction scheme, the phase (solid lines) is scaled to the expected slice distance and the trajectories achieved in the presence of different off-resonances are consistent with the trajectory in the on-resonant case.

Linear off-resonances are not direct proportional to the slice distance and furthermore can be present on the actual gradient axis under test but also in the two perpendicularly gradient axes which makes a correction difficult.

A gradient amplitude in an arbitrary direction, affected by linear off-resonances, can be represented by the following equation:

$$G = \sqrt{(G_x + \Delta G_x)^2 + (G_y + \Delta G_y)^2 + (G_z + \Delta G_z)^2}$$

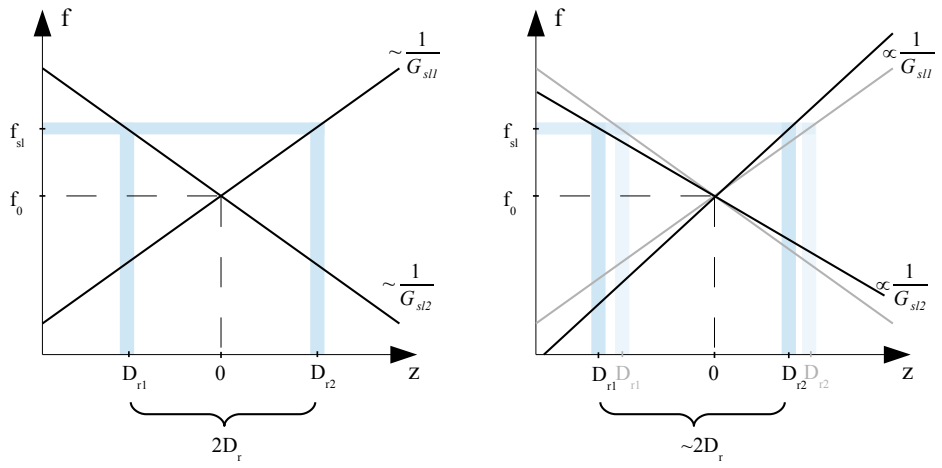

(a) $\Delta G = 0$. **(b)** $\Delta G \neq 0$.

Figure 38.: Impact of linear off-resonances on the slice selection process. The absolute position of the slice distance changes but the deviation can be minimized by using opposed slice selection gradients.

where G_x ,G_y , and G_z represent the applied readout gradient in an arbitrary direction, and ΔG_x ,ΔG_y , and ΔG_z represent the additional gradient amplitude due to related linear off-resonances on the three gradient axes. Assuming trajectory mapping on the x-axis of the physical gradient $G_{sl} = G_x$ and a linear off-resonance in the same direction ($\Delta G_y = \Delta G_z = 0$), the slice selection gradient is affected by the factor $x_{lin,sl} = \Delta G_x / G_{sl}$:

$$\tilde{G}_{sl,+} = \sqrt{(G_x + \Delta G_x)^2} \quad = G_{sl}(1 + x_{lin,sl}) \qquad G_{sl} > 0$$

$$\tilde{G}_{sl,-} = \sqrt{(-G_x + \Delta G_x)^2} = G_{sl}(-1 + x_{lin,sl}) \qquad G_{sl} < 0$$

To minimize the effect of linear off-resonances on trajectory mapping, two slices with the same RF settings and opposite slice selection gradient amplitudes were excited and the received phase signals were subtracted. Figure 38 demonstrates the impact of linear off-

resonances and the impact of the applied correction scheme on the slice selection process.

For the applied correction approach the effective distance from isocenter differs only by a factor of $x^2_{lin,sl}$:

$$D_r = \frac{D_r(\Delta f_{sl}, \tilde{G}_{sl,+}) - D_r(\Delta f_{sl}, \tilde{G}_{sl,-})}{2}$$

$$= \frac{2\pi\Delta f_{sl}}{\gamma G_{sl} \cdot (1 - x^2_{lin,sl})}$$

Therefore a linear off-resonance of 5% of the slice selection gradient ends up in a k-space deviation of 0.25% from the estimated trajectory.

Considering the same linear off-resonance but the slice selection and the gradient under test in y direction, the applied approach doesn't have any correction effect. However the effect of linear off-resonances perpendicular to the applied slice selection gradient inherently influences the applied gradient strength by $\sqrt{1 + x^2_{lin,sl}}$ and therefore impact less than the corrected off-resonance parallel to the slice selection gradient.

$$\tilde{G}_{sl,+} = \tilde{G}_{sl,-} = \sqrt{(\Delta G_x)^2 + (G_y)^2} = G_{sl}\sqrt{(1 + x^2_{lin,sl}}$$

$$D_r = \frac{D_r(\Delta f_{sl}, \tilde{G}_{sl,+}) - D_r(\Delta f_{sl}, \tilde{G}_{sl,-})}{2}$$

$$= D_r(\Delta f_{sl}, \tilde{G}_{sl,+})$$

$$= \frac{2\pi\Delta f_{sl}}{\gamma G_{sl}\sqrt{1 + x^2_{lin,sl}}}$$

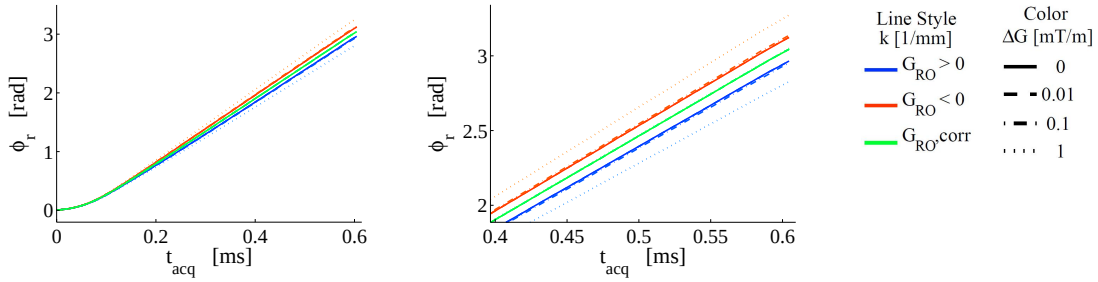

(a) **(b)**

Figure 39.: Impact of biased slice locations on the mapped k-space trajectory caused by a linear order off-resonance.

Figure 39 shows the effect of linear off-resonances for values of $1mT/m$, $0.1mT/m$, and $0.01mT/m$ related to the reference trajectory. The reference trajectory was mapped in an unshimed magnet and it is clearly visible that already a base linear off-resonance is present.

Trajectory calculation

The k-space profile for each gradient axis is achieved in five steps.

(i) Baseline correction calculating the phase deviation for readout gradient switched on and off.

(ii) Calculation of the overall phase evolution by unwrapping of the baseline corrected profile.

(iii) Correction for the impact on slice selection in the presence of zero order off-resonances using a pair of profiles achieved for RF modulation frequencies of opposed sign.

(iv) Reducing impact on slice selection in the presence of linear off-resonances using a pair of profiles achieved for slice selection gradient amplitudes of opposed sign.

(v) Normalizing the corrected phase by the expected distance to the isocenter to achieve the k-space trajectory.

All steps have to be performed for positive and negative readout gradient amplitude. Overall a number of 36 experiments (3 axes × 3 readout gradient settings × 2 RF modulation frequency setting × 2 slice selecting gradient settings) have to be applied, neglecting signal averaging for improved SNR.

5.2.2. Image Reconstruction using the Trajectory Mapping Approach

To achieve acceptable image quality, the k-space trajectory used for the image reconstruction must be precisely known. This can be ensured by either using the mapped trajectory for the reconstruction process or using hardware to modify the input of the gradient coil in such way that the applied gradient waveform and the respective non-idealities result in the estimated k-space trajectory.

Image Reconstruction using the Mapped Trajectory

The basic approach to consider for waveform distortions and inconsistent gradient channel delays is simply mapping the real k-space trajectory and use it for image reconstruction. A big advantage of this approach is that there is no need for additional hardware to correct for eddy currents and timing mismatch of the gradient channels.

To demonstrate the ability of this method the MR channel delays and pre-emphasis were switched off during data acquisition in a consecutive manner. The impact of four correction adjustments on image reconstruction were investigated by using gradient waveform pre-emphasis (GPE) and correction of gradient channel delays (GCD), using either GPE or GCD and without using any corrections. For each of the acquisitions, mapping scans were performed for all three gradient axes. The distance of the slice to the gradient isocenter was chosen $D_r = 10mm$. Intermediate profiles of the k-space trajectory were generated by superposition of the measured gradient waveforms for the three physical axes.

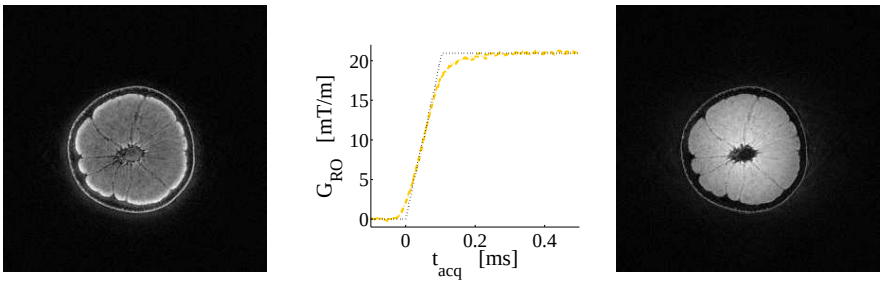

(a) GCD and GPE enabled.

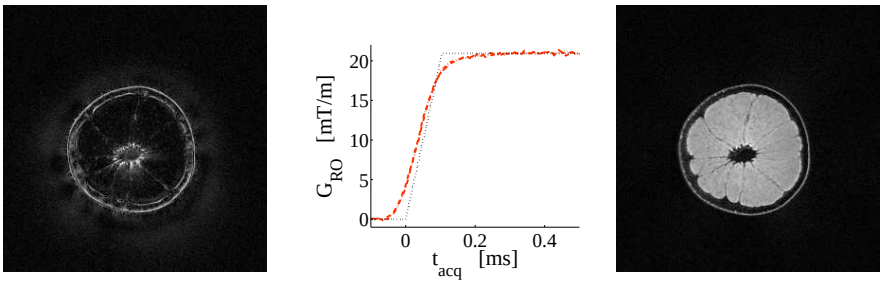

(b) GCD disabled.

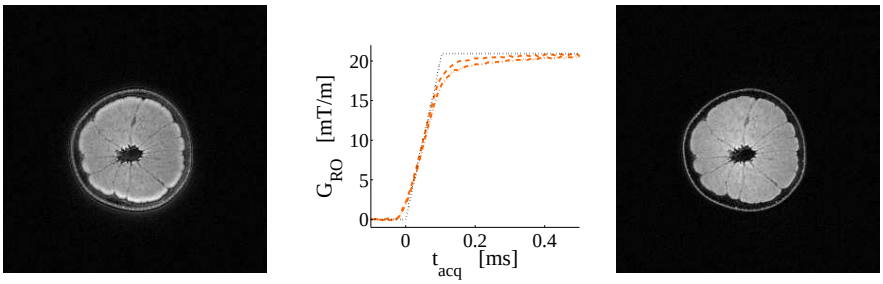

(c) GPE disabled.

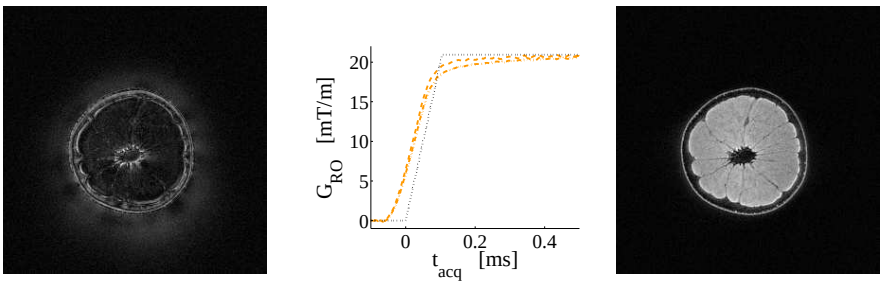

(d) GPE and GCE disabled.

Figure 40.: Reconstructed images using the ideal gradient model (left side) and the mapped trajectories (right) for compensated gradient waveform imperfections (a,b) and gradient delays (a,c) and uncompensated gradient waveform imperfections (c,d) and gradient delays (b,d). The corresponding distorted gradient waveforms calculated from the mapped trajectories are shown in the middle.

Figure 40 shows images reconstructed assuming the ideal (left) and the mapped k-space trajectories (right). The related gradient waveforms of the ideal (black) and the mapped (coloured) trajectory are shown in the middle. It can be observed that even in case of full hardware correction the ideal gradient shape differs from the real gradient waveform. Gradient imperfections as well as gradient delays can be compensated for by using the measured k-space trajectory for the image reconstruction in all four cases. Since the k-space trajectory changes for every adjustment of sequence parameters which results in a variation of the gradient strength, the gradient length, the slope duration and the acquisition timing, the mapping of the real k-space trajectory has to be performed for every new set of scan parameters.

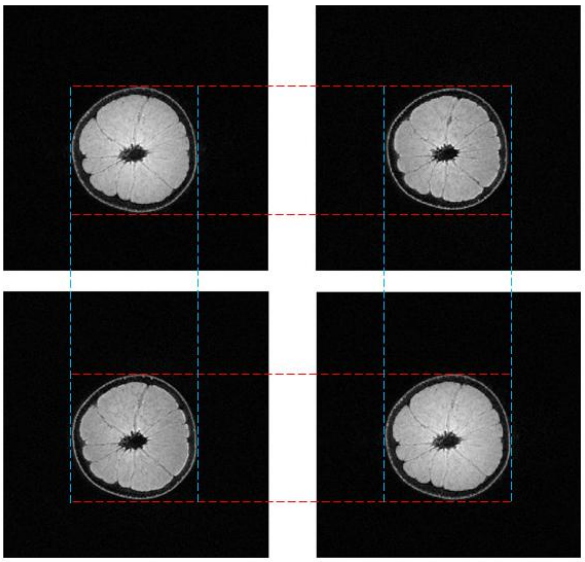

Figure 41.: Upper left and lower right show the reference image reconstructed with the ideal k-space trajectory. The upper right figure shows the reconstructed image with GPE switched off and without compensation of the missed k-space data. Since the resolution is not adjusted for the given field of view the object appears smaller than in the reference case. If the missed k-space is compensated during the image reconstruction process the object is readjusted to its original size (lower left).

To avoid the influences of eddy currents on the slice selection process in cases where GPE is switched off, the slice selection gradient should be switched on a few millisecond prior to the RF pulse. For extreme gradient settings (high slewrates) the impact of induced eddy currents on slice selection can lead to notable impact on image quality especially in z-direction. Therefore the slewrate of the slice selection should be chosen as small as possible.

Since eddy currents and gradient delays always change the area for the applied encoding gradient during signal acquisition, the resolution of the achieved image has to be adjusted during image reconstruction (fig. 41). Therefore the size of the reconstruction matrix has to be adapted by a factor $\Delta x_{ideal}/\Delta x_{meas}$ for a given field of view.

Image reconstruction using Hardware Correction for Gradient Waveform Pre-Emphasis and Gradient Channel Delays

To compensate for the above mentioned distortion in the slice selection process and to avoid permanent mapping of the k-space trajectory for every single adjustment in the parameter settings, gradient waveform corrections as gradient waveform pre-emphasis (GPE) and gradient channel delays (GCD) are used for instantaneous trajectory correction during the measurement.

Modern MRI systems have the ability to provide a time delay for each physical gradient axis to compensate for timing mismatch between the gradient and the receive coil as well as a subsystem that allows to compensate for eddy current effects. Gradient channel delays can be calculated by the phase difference between two gradient echoes with opposed gradient amplitudes. This has to be conducted for each physical gradient channel. Since the gradient time shift depends on the actual gradient and acquisition settings (sec. 5.1.4), the correction of the delay is not final and the fine tuning of the gradient delay has to

be done for every change of scan parameters and needs to be considered during image reconstruction.

For the compensation of eddy currents, waveform pre-emphasis is used to adapt the actual digital gradient waveform input to the gradient coil in such way that the pre-emphasis distortion cancels the subsequent eddy current distortion. The time constants τ_n and amplitudes α_n to model the behaviour of the eddy currents can be achieved by comparison of the quantitative model of eddy currents and the measured gradient waveform [3]. Since the eddy current behaviour changes due to changed input to the gradient coils, one has to use a slightly modified set of timing and amplitude parameters which can be derived analytically from the measured ones using the method described by Jehenson [26].

The available MRI system uses 16 pairs of timing and amplitude settings for each physical gradient channel to model the eddy current behaviour and provide adjustment of the channel delay for each of the main physical gradient channels. Although the clinical systems are well calibrated regarding delay correction and eddy current compensation there are still some imperfections left such as non-compensated eddy currents with short time constant terms and waveform distortions due to gradient system dynamic response.

To compensate for these remaining non-idealities, the real gradient waveform is determined by convolving the ideal gradient waveform from equation 5.4 with an exponential system impulse response with a single time constant τ_{sys}:

$$G_{real} = G(t) * e^{(-t/\tau_{sys})}$$

This convolution emulates the distorted edges at the beginning and end of the rising slope of the readout gradient which is used during the image reconstruction process. The system time constant τ_{sys} was determined by calculating the difference between the measured and model-based gradient waveforms for time constants between $20\mu s$ and $50\mu s$. If the

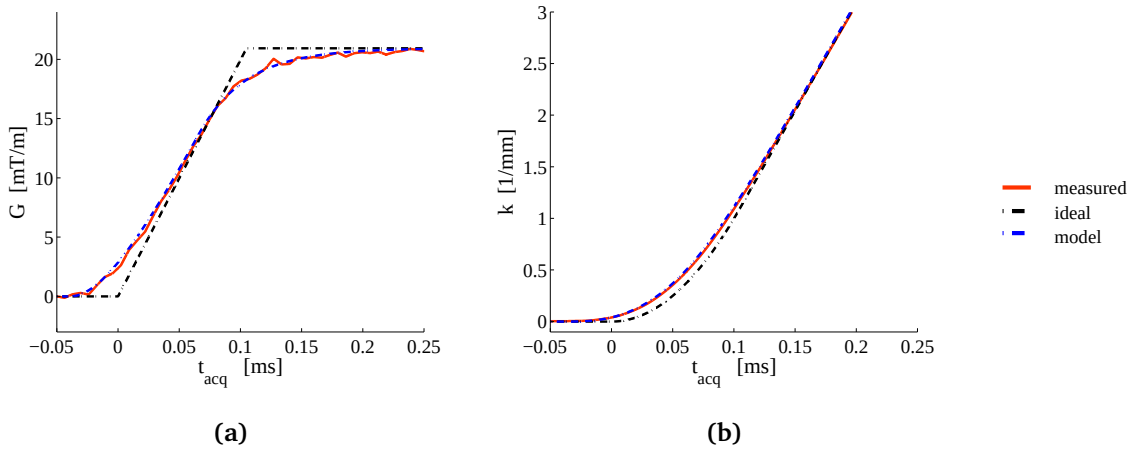

(a) **(b)**

Figure 42.: (a) Gradient waveform and (b) related k-space trajectory for the ideal (solid black), the measured (dashed red) and the modelbased (dashed blue) readout gradient. Using the ideal gradient waveform for trajectory calculation squeezes the k-space coordinates in the center of k-space.

system time constant is to low, the model of the trajectory corresponds approximately to the ideal gradient waveform and therefore squeezes the k-space values in the center while a overvalued time constant leads to a dilation of the k-space coordinates in the center. G_{real} for a value of $\tau_{sys} = 39\mu s$ was found as the waveform with minimum gradient deviations over different gradient settings and therefore is used as fixed system timing parameter in the reconstruction framework. The behaviour of the the ideal, the measured, and the modeled gradient waveforms as well as the behaviour of the respective k-space trajectories are shown in figure 42.

Figure 43 shows the images using the trajectory calculated from the ideal gradient waveform for the reconstruction process and using the trajectory calculated from the presented model for image reconstruction, to correct the applied ideal gradient waveform. Using the trajectory calculated from the ideal gradient waveform for image reconstruction, leads to a compression of the k-space coordinates in the center and therefore to degradation in image quality due to the mismatch of acquired data and estimated k-space position. Us-

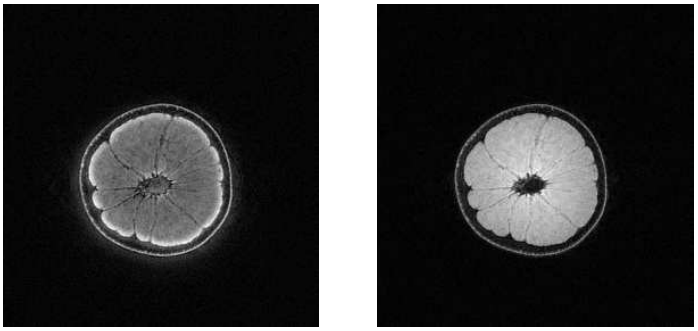

(a) (b)

Figure 43.: Reconstructed images using the ideal (left side) and the introduced (right) gradient model for compensated gradient waveform imperfections.

ing the introduced model, the calculated gradient performance is close-to actual applied gradient waveform and the reconstructed images show high image quality without visible image degradation.

5.3. UTE for Identification of Caries Lesions

The objective of this section is to evaluate the applicability of ultra-short echo time (UTE) imaging for in vivo assessment of carious lesions and early demineralization stages by means of MRI. Therefore 12 patients (average age 34+/-17 years) were enrolled in a feasibility study.

All patients underwent a conventional clinical dental investigation including optical assessment of the teeth as well as either a conventional orthopentogram or a bitewing x-ray (XR). The dental MRI examination was performed within 14 days after the initial dental assessment prior to any dental treatment. The imaging protocol was approved by the local ethic committee of the University and written informed consent was obtained before dental MRI imaging from all patients. The patients underwent a standardized MRI protocol including

multiple survey scans for different orientation, a coil sensitivity scan and two diagnostic scans. A high spatial resolution multi-slice turbo-spin-echo acquisition followed by a three-dimensional ultra-short echo time (3D-UTE) scan. Sequence parameters are summarized in table 1.

For data analysis all data were transferred to a medical workstation (ViewForum, Philips Healthcare). According to the hypothesis that early demineralizations as well as progressed caries lesions cause local formation of acid or saliva pools, conspicuous locations in the teeth were identified according to bright spots in the dentin or enamel layer, which could not be attributed to the dental pulp and which showed a signal enhancement of at least two times the standard deviation of the surrounding tissue. Initial identification was done in the 3D-UTE images. Subsequently, the appearance of the conspicuous locations was compared with the appearance in the spin-echo images and the prior acquired XR images. All images were reviewed by two experienced MRI readers and a dentist in consensus. Each lesion was classified according to its visibility in the different imaging approaches.

From the images it becomes obvious that in MRI a clear delineation between the dental pulp and the mineralized structures, but only weak (3D-UTE) to no (TSE) delineation of the dentin and enamel layer can be achieved. Only a limited delineation of the occlusal surface of the teeth can be achieved at locations where teeth from the upper and lower jaw are in direct contact. Also limited delineation of enamel and dental fillings can be observed since both materials appear dark in the MRI images. All other surfaces can be clearly delineated due to the surrounding soft tissue (tongue, cheek) or a saliva layer (inter-dental spaces, occlusal surface not in direct contact with the opposite jaw).

The patients were selected randomly and showed multiple previous dental fillings, including amalgam (n=12), composite (n=104), and gold (n=4) fillings. Two patients had gold crowns (n=2). Severe image degradation due to dental fillings was observed in two 3D-

Table 1.: Sequence parameter for the MRI measurement protocol

	TSE	UTE
Technique	Multi Spin-Echo	spoiled FID
k-space Encoding	cartesian	3D radial
Excitation	slice selective	non-selective
Flip Angle [°]	90	10
RF Pulse Duration [ms]	4.2	0.05
Echo Time [ms]	8.1	0.05
Repetition Time [ms]	625	5
Readout Duration [ms]	3	0.8
# Echoes	16	1
Acquired Resolution [mm^3]	0.4x0.4x1	0.8x0.8x0.8
Reconstructed Resolution [mm^3]	0.4x0.4x1	0.5x0.5x0.5
Field of View [mm^3]	230x230x8	120x120x120
Scan time [min]	5:32	7:49

UTE and in the respective HR-TSE scans. The artifacts were confined to a single tooth and did not show wide range image degradation as known from volume CT. Patients with retainers or brackets were excluded due to the expected severe image artifacts caused by the nickel or cobalt containing alloys.

Overall three different types of lesions could be identified. Class CI lesions (19%) are visible in the 3D-UTE as well as in TSE, and the XR images. Lesions visible in the 3D-UTE images as well as in the XR images but not visible in TSE images were categorized as class CII lesions. This class includes the majority of lesions (62%). For CI and CII lesions all lesions appear substantially larger in UTE in direct comparison to the respective lesions in XR which indicates a substantially larger degradation of the tooth than indicated by XR. Many lesions, which appeared in safe distance to the dental pulp in the XR, almost reached to its direct proximity in the UTE images. The appearance of CI lesions in the TSE images was always less enhanced with a smaller extent than in the 3D-UTE images but a still larger extent than in XR. Class CIII lesions are visible in the 3D-UTE images

and not clearly recognizable in the XR images. CIII lesions were either located in direct proximity of dental fillings or at locations of unclear situations in the XR, mainly caused by superposition of structures. There was no lesion, which was solely identified in the XR images.

Representative examples of the appearance of different kind of lesions are shown in figure 44.

For quantitative analysis the maximal width (w), height (h), depth (d) (MRI only), areal extent (A) of the lesions, and its minimal distance d_{pulp} to the dental pulp were quantified separately for all modalities. Figure 45 shows a transversal, a parasagittal and a coronal view of the jaw and the related definition of lesion extension. Measurements of w, h, A and d_{pulp} were performed in the parasagittal reformatted MRI data and directly in the respective bitewing XRs. Statistical analysis of the results was done by applying a paired student's t-test. P-values below 0.05 were considered significant. For detailed findings of the statistical analysis please refer to [7]. In summary the quantitative analysis of the geometrical properties of the lesions confirmed the qualitative findings.

Comparing the different image modalities, the width (w), height (h), and area (A) of CI lesions showed significantly smaller values in the TSE images as compared to the 3D-UTE and XR results. While the differences between 3D-UTE and XR showed only a trend to larger areal extent in UTE for CI lesion,s a highly significant difference in all assessed geometrical properties was observed between UTE and XR for CII lesions. The distance to the dental pulp resulted significantly smaller in UTE than compared to TSE and XR. Also the comparision between the different categories revealed significant larger lesion properties for CI lesions compared to CII and CIII lesions and for CII compared to CIII except of the difference in the width for CI and CII lesions which shows only a trend. The distance of the lesion to the dental pulp showed a non-significant trend to larger values with increasing category.

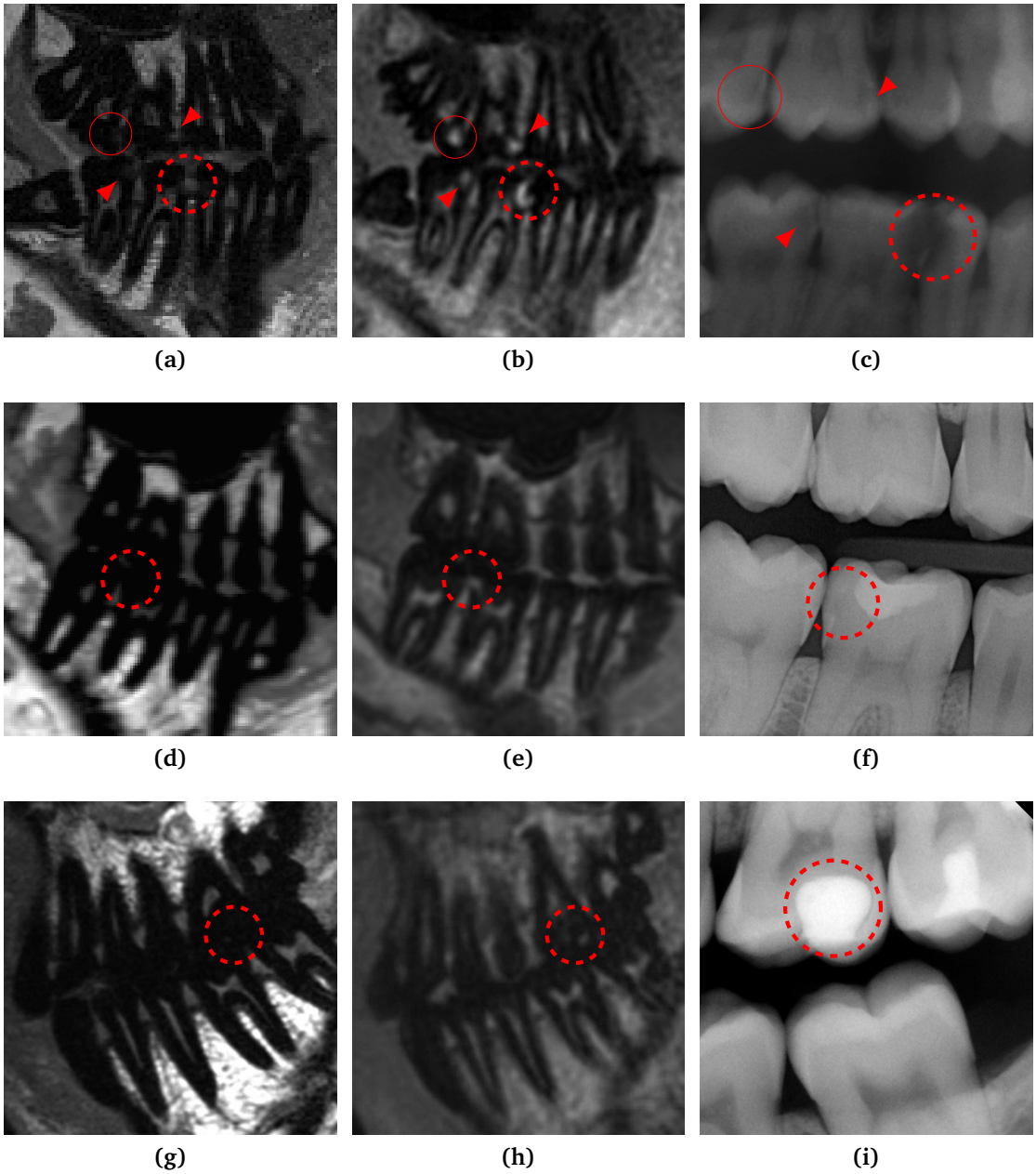

Figure 44.: Representation of different caries lesion classes in MR images using (a), (d), (g) a conventional TSE (b), (e), (h) and a dedicated UTE sequence and the representation in (c), (f), (i) x-ray images. Upper row shows multiple CI lesions which are visible in all image modalities. In the second row a lesion of category CII is shown where the portion of demineralization is not high enough to make the signal visible in conventional MR. The lesion of category CIII (third row) represents the case of a hidden caries which could not be identified in the x-ray due to its planar imaging technique.

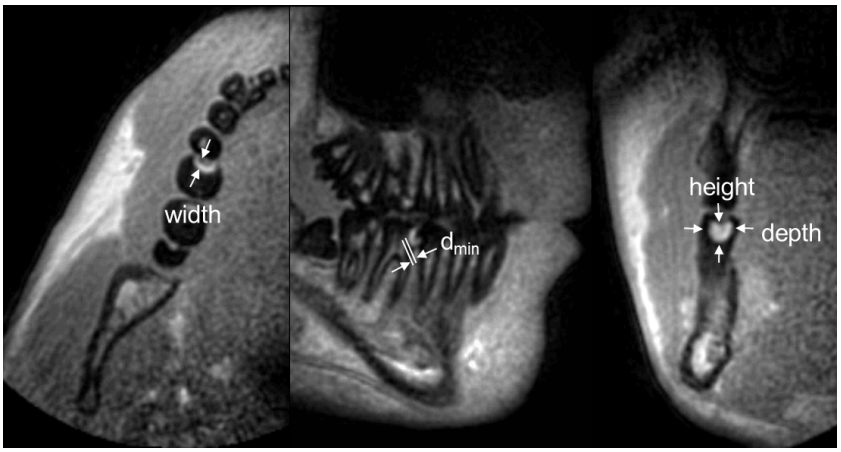

Figure 45.: Definition of the measured lesion extensions and the distance to the pulp [8, p. 5.], licensed under CC-BY-NC 3.0.

After imaging and data analysis, all patients underwent conventional dental treatment as clinically indicated. For assessment of the real lesion extension a patient with hidden caries of category CII identified in MRI was selected randomly for in-situ validation of the imaging results. For this patient, each step of the treatment was documented. The excavation was controlled by caries detector fluid (1% acid red) plus frequent manual exploration of the hardness of the dentin. Before and after excavation, impresses were taken. Figure 46 shows the intra-oral images taken prior to treatment, after fissure sealant removal, after excavation and after filling of the cavity. Only a conspicuous area before dental treatment could be identified in the intraoral image. For documentation of the lesion depth, a bitewing XR (fig. 46e) of the post-excavation imprint was acquired and the lesion extend was compared to the x-ray bitewing and the UTE and TSE MRI images. In the 3D UTE image the lesion shows a bright signal, while it is not visible in the TSE images. Comparing the lesion extend the signal in 3D UTE image ranging into the proximity of the pulp but in x-ray the identified lesion seems at safe distance to the pulp. For qualitative comparison between the x-ray image of the impression and the in-vivo MR and x-ray images the lesion shape after excavation was estimated from the radiograph of the impression and transferred to the

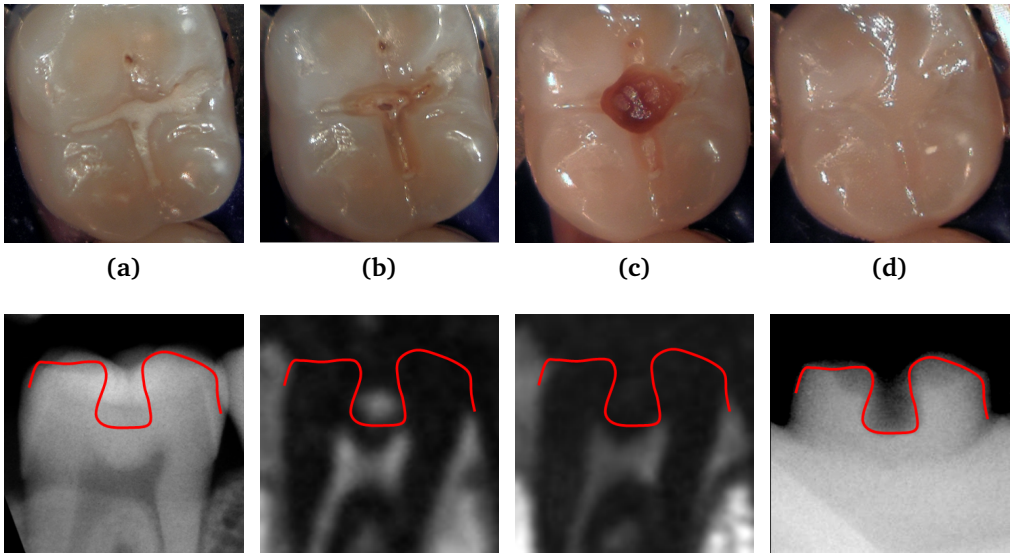

Figure 46.: In vivo validation for an occult lesion. Intraoral pictures of the lesion were taken (a) prior treatment, (b) after fissure sealant removal, (c) after excavationa and (d) after filling. Lesion extend of the (e) x-ray bitewing, (f) UTE and (g) TSE MRI were compared to the extension revealed by the (h) x-ray of the generated impression. Subfigures (e),(f),(h) are taken from [8, p. 10.] figure 8b, licensed under CC-BY-NC 3.0.

in vivo images. The lesion extensions from the impressions of the in-situ measurements confirm the lesion size in the 3D UTE images and the respective underestimation of the caries lesions in the x-ray images.

All findings could be confirmed by a clinical study with 40 patients enrolled and 4 cases of in-situ evaluation of the lesion extend [8].

5.4. UTE-T_2^* for Quantification of Caries Lesions

MRI has attracted great interest as a quantitative tool for the improvement in sensitivity and the reduction of subjectivity of visual evaluation. For the quantification so called

relaxation maps, based on relaxation properties of the different tissues, are used. These maps are usually calculated by using multiple acquisitions at different echo times and a fixed relaxation time. The maps can either be calculated from spin-echo (T_1 and T_2 map) or gradient echo sequences (T_2^* map) depending on the chosen application. Since the major contrast in caries imaging is related to the spin-spin interaction in the hard tissues and the signal decay is very fast in those tissues, none of the conventional quantification sequences can be used due to their very high echo times compared to the relaxation times. To detect changes in tissues with very short T_2^* values, a ultra-short echo time T_2^* (UTE-T_2^*) mapping approach is used as a quantitative MRI technique.

To obtain a T_2^* map for tissues with ultra-short T_2^* relaxation factors, the free induction decay is measured multiple times for UTE sequences with different echo times. Figure 47 shows the imaging sequences and the related k-space sampling distribution. For each TE the full k-space has to be acquired to avoid image distortion due to undersampling.

The T_2^* values are calculated pixel-by-pixel from the set of UTE images, using a mono-exponential model for the fitting routine:

$$S(t) = S_{offset} + S_0 e^{-\left(\frac{t}{T_2^*}\right)}. \tag{5.31}$$

Both, the proton density S_0 and the transversal relaxation T_2^*, characterise the investigated tissue while S_{offset} considers the Rician noise as a constant offset. The longitudinal relaxation of the tissue is neglected due to the very short T_2^* values and related short echo times compared to T_1 relaxation.

As mentioned before the signal enhancement in carious lesions is attributed to the increase in liquid content during the lesion formation and the local demineralization of the hard tissues. Figure 48 shows the impact of caries lesion progress on the transversal magnetization and signal sequence related to T_2^* relaxation. In the case of completely intact

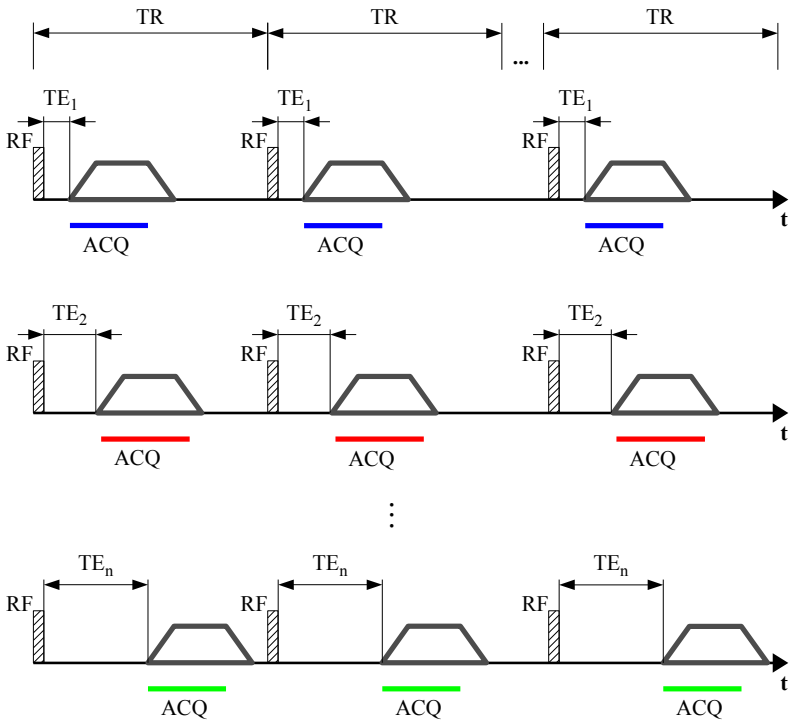

(a) UTE- T_2^* Sequence

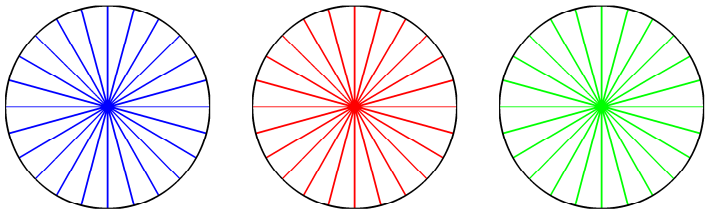

(b) k-space sampling distribution.

Figure 47.: Timing of a set of measurements to obtain T_2^* maps. Each sequence has a different but fixed echo time.

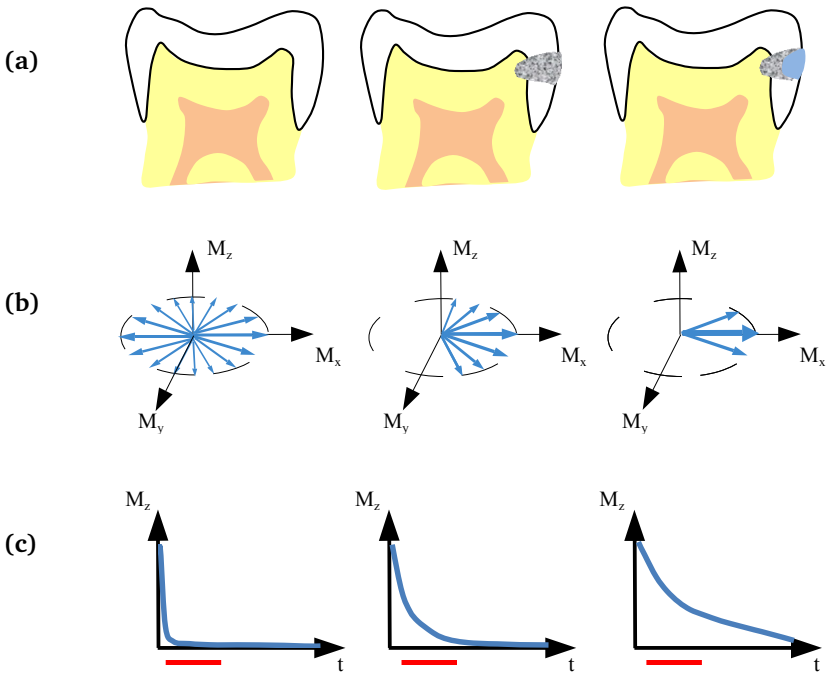

Figure 48.: T_2^* relaxation depending on caries lesion progress. (a) Schematic of intact dentin, initial demineralization and breakdown of the dentin with bacterial colonization in the cavity (left to the right). (b) Related dephasing of the spins and (c) related process of the spin-spin relaxation over time. The red line marks the the acquisition time inside the imaging sequence.

mineral structures (left) the transversal magnetization dephases very fast and the signal is strongly attenuated during acquisition. A local demineralization of the enamel and the dentine (mid) leads to a reduction of dephasing and therefore to much slower T_2^* related decay of the MR signal. The total breakdown of the mineral structures (right) leads to further increase in the local T_2^* and to concomitant accumulation of acids and saliva in the caries lesion which leads to an increase in proton density and therefore in signal intensity. The impact of distortion of the mineral structure on the local T_2^* relaxation times

can be investigated by quantification of T_2^* relaxation in caries lesions in comparison to the surrounding dentine.

For the quantification of caries lesions, in-vitro as well as in-vivo experiments were performed. For the in-vitro measurements nine extracted human teeth underwent the imaging protocol. The signal reception was done with the dedicated small animal coil. A set of UTE sequences with five different echo times TE = 50, 100, 250, 500, 1000 and 2500μs were used to obtain the relaxation. The image data for in-vivo quantification in four volunteers with known caries lesions and existing bitewing x-ray was acquired using the prototype carotid artery coil. The echo times were chosen to TE = 60, 150, 340, 500, 1000, 3000, and 5000μs.

Caries lesions were identified according to section 5.3 as areas showing a signal enhancement of more than two times the standard deviation of the surrounding tissue. In-vitro 10 caries lesions were observed in six teeth. In the in-vivo experiment 11 caries lesions were observed in six teeth (moderate occludal (1), approximal (5) and secondary caries (4)). To classify the lesions to the lesion categories introduced in section 5.3 according to their visibility in the different image modalities an additional T_1-weighted TSE imaging sequence was acquired. Imaging parameters for the different experiments are listed in table 2.

No lesion was visible in the T_1-weighted TSE sequence and therefore no lesion of class CI was investigated. The lesions in the in-vivo experiment were classified according to their x-ray visibility into two classes (CIII - MRI only, 6 lesions; CII - MRI and XR, 5 lesions). To obtain the T_2^* relaxation times UTE images with different echo time were manually registered off-line and the respective T_2^* time was fitted by the introduced mono-exponential model. Statistical relevance of the resulting differences of the relaxation times was accessed by applying a one-tailed student's t-test with a two-sample unequal (heteroscedastic) variance. Differences were considered significant for p-values less than 0.05.

Table 2.: Sequence parameters for the in-vivo and in-vitro UTE-T_2^* measurements

	T_1-weighted TSE	UTE
Technique	Multi Spin-Echo	spoiled FID
k-space Encoding	cartesian	3D radial
Excitation	slice selective	non-selective
Flip Angle [°]	90	10
Echo Time [ms]:in-vivo	8.1	0.06 - 5.0
Echo Time [ms]:in-vitro	8.1	0.05 - 2.5
Repetition Time [ms]	625	10
Pixel BW [Hz]	240	800
#Echoes	16	1
Resolution [mm^3]	0.4x0.4x1	0.8x0.8x0.8
Field of View [mm^3]	230x230x8	120x120x120
Scan Time [min]	5:32	3:40

Table 3.: Measured T_2^* values of the dentin, of multiple caries lesions classified as CII or CIII lesions and the related p-values

	$T^*_{2,dentin}[\mu s]$	$T^*_{2,lesion}[\mu s]$	$T^*_{2,CI}[\mu s]$	$T^*_{2,CII}[\mu s]$	$p_{dentin,lesion}$	$p_{CI,CII}$
in-vivo:	324 ± 94	694 ± 399	464 ± 35	972 ± 470	≤ 0.01	≤ 0.05
in-vitro:	284 ± 32	361 ± 59			0.01	

For the in-vitro experiments the relaxation times of dentin were obtained for every teeth. The mean T_2^* value of dentin for the in-vivo experiments were analysed in 16 teeth. For the in-vivo as well as for the in-vitro experiments the values for dentin were significantly lower than for the caries lesions. It was also observed that the transversal relaxation for initial caries lesions of class CIII is significantly lower than for moderate CII-lesions. The mean T_2^* relaxation times for dentin as well as for the lesion result in lower values for the extracted teeth compared to the in-vivo analysis. This may be attributed to dehydration of the in-vitro samples during the measurements. Detailed values of the relaxation times and the p-values are listed in table 3. Measurement data for the in-vivo data are shown in figure 49.

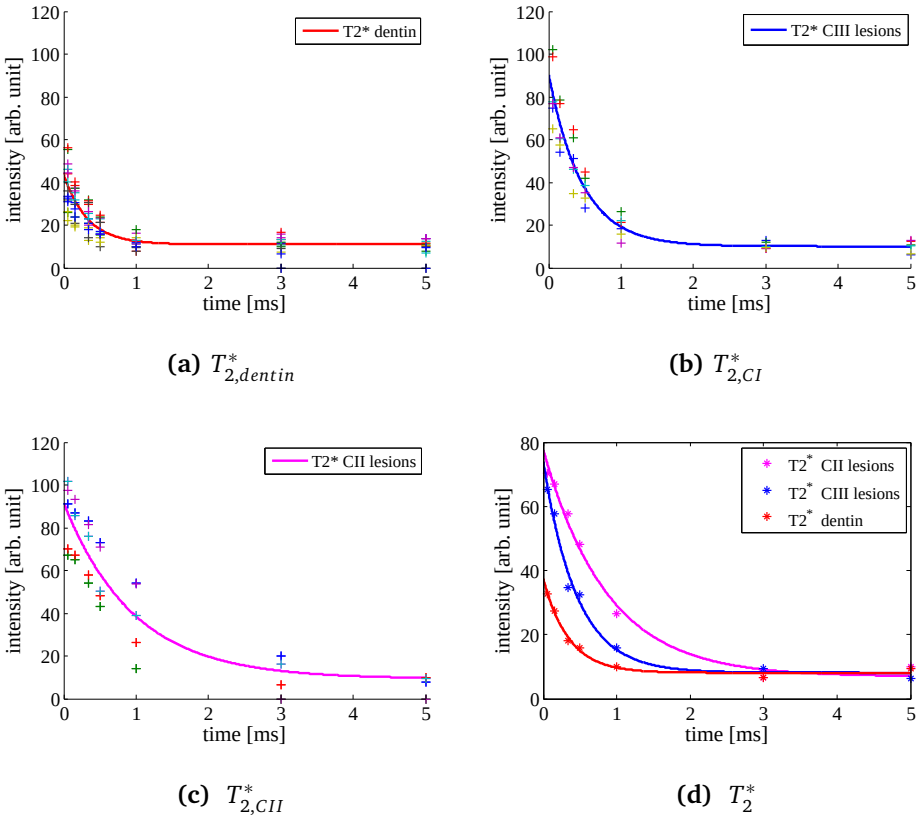

(a) $T^*_{2,dentin}$ **(b)** $T^*_{2,CI}$

(c) $T^*_{2,CII}$ **(d)** T^*_2

Figure 49.: Measured data of in-vivo examination for the T_2^* decay of (a) dentin, (b) CIII and (c) CII caries lesions. (d) Comparison of the three decay curves. Markers represent the measured data and the lines the exponential decay with the main T_2^* value obtained from the individual measurements.

A significant difference between the mean T_2^* values in caries lesions and healthy dentin was observed. The T_2^* of carious lesion was significantly larger than the T_2^* of dentin, but still well below $1ms$ in initial to moderate lesions. This proofs the sensitivity of UTE-T2* mapping of caries lesions to the loss in mineral structure of the teeth. Significant changes in T_2^* were observed even before the lesions got visible by XR. This indicates a huge potential of MRI to identify caries lesions at a very early stage before substantial breakdown of the mineral structure. The received results confirm the findings of section

5.3 that the identification of caries lesions by MRI is possible, but requires ultra-short echo time techniques.

5.5. Discussion

The main limitation of MRI for dental applications results from its inability of assessing hard tissue structures and hence from its very limited performance in delineation of the mineralized components of the tooth. Due to the high mineral content, the concentration of free protons is extremely low causing only weak magnetization and due to the susceptibility interfaces in the mineral structures, the spin-spin relaxation times result below $1ms$. For direct imaging of dental hard tissues and initial caries lesions a optimized three-dimensional UTE sequence is applied. Sequence performance depends on optimization of different imaging parameter for excitation pulse and readout gradient settings. For signal excitation a ultra-short non-selective block pulse was used to reduce the effect of T_2^* relaxation during RF excitation. Flip angle was chosen to 10° to keep the pulse as short as possible and reduce T_2^* weighting during excitation but long enough to ensure adequate signal-to-noise ratio. The impact of tissue depended T_2^* relaxation and offset in precession frequency (e.g. $f_{off,fat} = 440Hz$ for $B_0 = 3T$) during readout is investigated and minimized by using high slewrates and moderate gradient strength to minimize the slope duration but facilitate fast k-space sampling at the constant gradient and therefore ensure short acquisition durations. Non-idealities like eddy currents, off-resonances and system electronics delays change the encoding functions and produce errors in image data reconstruction assuming the ideal Fourier encoding. While eddy currents and off-resonances change over time and in a 3D radial acquisition scheme all three spatial encoding directions are performed as readout gradients, the non-ideality affects all three spatial directions and is not limited to a single spatial direction like in Cartesian imaging.

In radial UTE imaging time variable k-space displacement from uncompensated eddy currents and off-resonances, and fixed k-space displacement related to system delays lead to severe artefacts in the reconstructed image. To compensate for deviation of the theoretical gradient waveform, the distorted waveform of the actual k-space trajectory can be measured and used for image reconstruction. In addition to the readout gradients the slice selection gradient is also distorted if the eddy current correction (ECC) and the correction for gradient channel delays (GCD) are disabled. The slice selection gradient should therefore be switched on at a proper time before RF excitation starts. The basic trajectory mapping approach is extended and additional measurements are applied to compensate for trajectory errors caused by frequency distortions during RF excitations and to minimize the effect of linear off-resonances. For ensuring close-to-ideal gradient waveforms, gradient waveform pre-emphasis (GPE) and gradient channel delays (GCD) are used to avoid severe image degradation. While the effect of eddy currents and gradient delays can be corrected for at the hardware side, untreated non-idealities (like gradient power supply rising edges) have to be compensated on the software side during image reconstruction. It is also shown that image distortions due to eddy currents and inconsistent channel delays can be sufficiently compensated without any need for GPE or GCD by simply mapping the real k-space trajectory and using it as input of the reconstruction framework. The gradient distortions caused by eddy currents of linear order and channel delays of the three gradient axes are automatically considered during reconstruction. Related artefacts are corrected by consideration of the true trajectory during reconstruction.

Applying the correction approach to image reconstruction ensures sufficient image quality for in-vivo evaluation of the introduced three-dimensional ultra-short echo time imaging sequence regarding identification of caries lesions. Therefore 12 patients with suspected caries lesions underwent a conventional clinical dental investigation including visual assessment of the teeth, dental x-ray, dental MRI investigation comprising UTE imaging, and

conventional turbo-spin-echo imaging (TSE). It has been shown that the sensitivity of the UTE sequence resulted at least in similar diagnostic accuracy as the clinical standard x-ray and clearly outperforms the MRI TSE sequence. The lesion extend appears smaller in the x-ray images compared to the observed lesions in UTE. Considering that the caries lesions normally appears too small on XR, MRI might be able to provide a more precise assessment of the real extent of the lesion. The signal enhancement observed for caries lesions compared to the mineralized structures of the teeth is accredited to the process of caries lesion formation. In lesion formation primeraly the local concentration of acids and salvia increase. This leads to a local increase in proton density and therefore to a local increase in magnetization. The initial decay of the local mineralization structure leads to a decrease of local random dephasing of the MR signal. With increasing demineralization, the local magnetization as well as the T_2^* relaxation time further increase to the point of local breakdown of the mineral structure where T_2^* values are no longer ultra-short or short but in the range of a few ten milliseconds or more. Three different classes of caries lesions are defined according to their visibility in the different image modalities which likely indicate caries lesions at different stages. Class CIII lesions indicate very early lesions/demineralization with no substantial breakdown of the microscopic mineral structure. These lesions are not visible using x-ray but visible in MR applying a 3D UTE imaging approach. With advanced demineralization and related breakdown of the mineral structure, the loss in mineral content can be depict from the x-ray images (CII) and finally even from conventional TSE sequences (CI). This presumption was confirmed by the findings of quantitative analysis of the T_2^* relaxation times for caries lesions. The significant increase in T_2^* between dentin and CIII as well as between CIII and CII demonstrates the progress in mineral structure degradation between the different caries classes.

6. Center-Acquisition at Partial Ramp Imaging (CAPRI)

In conventional UTE imaging the k-space center is acquired at the beginning of the ramp-up of the readout gradient. In CAPRI imaging at least the dead time of the system is used to shift the k-space center along the gradient ramp towards the constant part of the gradient and therefore reduce k-space data sampling during gradient ramp up. In this chapter the utilization of 3D radial FID imaging with center acquisition at partial ramp imaging is demonstrated for the acquisition of volume data with ultra-short echo times. In the first section the impact of T_2^* decay and off-resonances during the readout process on spatial resolution and signal intensity is analysed, the impact on SNR due to the modified sampling scheme is investigated and the consequence for signal acquisition is discussed. The following section introduces an approach for automatic gradient channel delay correction without any additional need for calibration scans by starting k-space sampling before the k-space center is reached. At last the application of CAPRI in dental MRI for visualization of initial caries lesion is investigated and compared to the conventional UTE imaging sequence.

6.1. Imaging Sequence

The CAPRI approach is a modification of the UTE sequence introduced in section 5.1 using an additional small prephasing gradient with amplitude G_{PRE} and duration T_{PRE} played

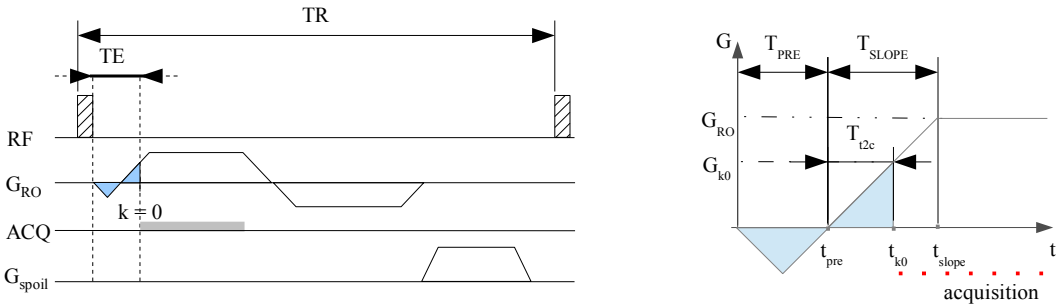

(a) **(b)**

Figure 50.: 3D CAPRI sequence: a small prephasing gradient is played out in front of the UTE readout gradient, which shifts the k-space center to a higher gradient strength. At least the dead time of the system is used to shift k-space center towards the flattop of the readout gradient. The block pulse excitation for spin stimulation, the rephasing gradient for gradient readout net-area nulling, and the spoiling gradient for dephasing of residual transverse magnetization remains the same as in the UTE sequence (sec. 5.1).

out at the same direction as the readout gradient. An example of the imaging sequence is shown in figure 50 for a single cycle repetition (left) and a cut-out of the initial gradient ramping (right). It starts with an prephasing gradient followed by the readout gradient G_{RO} and a rephasing gradient. The prephasing gradient area positions the k-space trajectory to a negative k-space coordinate in such way that the rising slope of readout gradient starts in front of the k-space center. The amount of time the k-space center is shifted along the gradient ramp is defined as a factor $f_{CAPRI} \in [0,1]$ of the slope duration itself:

$$T_{t2c} = f_{CAPRI} \cdot T_{slope}, \tag{6.1}$$

and the reached gradient strength can be expressed as a factor of the readout gradient strength:

$$G_{t2c} = f_{CAPRI} \cdot G_{RO}. \tag{6.2}$$

To minimize eddy current effects the same slewrates for prephasing and readout gradient are assumed. For further computation it is also assumed that the waveform of the prephasing gradient is a triangle (only rising and falling slope without constant part). The maximum gradient strength of the prephasing gradient can then be expressed in terms of the slope duration $T_{PRE}/2$:

$$\begin{aligned} \frac{G_{PRE}}{T_{PRE}/2} &= \frac{G_{RO}}{T_{slope}} \\ \Rightarrow G_{PRE} &= \frac{G_{RO} \cdot T_{PRE}}{2T_{slope}} \end{aligned} \tag{6.3}$$

The duration of the prephasing gradient can be obtained by equalizing the gradient area of the prephasing gradient A_{PRE} and of the rising readout gradient slope till k-space center A_{t2c} :

$$\begin{aligned} A_{PRE} &\stackrel{!}{=} A_{t2c} \\ -2 \cdot \frac{1}{2} G_{PRE}(T_{PRE}/2) &\stackrel{!}{=} -\frac{1}{2} G_{t2c} \cdot T_{t2c} \\ \Rightarrow T_{PRE} &= \sqrt{2} T_{slope} \cdot f_{CAPRI} \end{aligned} \tag{6.4}$$

The duration of the prephasing gradient can be rewritten as a function of G_{RO} using equations 6.3 and 6.4:

$$G_{PRE} = \frac{1}{\sqrt{2}} G_{RO} \cdot f_{CAPRI} \tag{6.5}$$

To keep the net-area of the readout gradient the same as in the original imaging sequence the gradient length has to be adapted by a factor $0.5 \cdot f_{CAPRI}^2 T_{slope}$ and the overall acquisition

duration of the basic CAPRI sequence results to:

$$T_{ACQ} = T_{const} + 0.5 \cdot f_{CAPRI}^2 T_{slope} + (1 - f_{CAPRI}) T_{slope} \tag{6.6}$$

The applied gradient in readout direction is separated in a falling slope of the prephasing gradient, a rising slope of the duration $T_{PRE}/2 + T_{slope}$ which starts at the mid of the prephasing gradient and the constant part of the gradient:

$$G_{CAPRI}(t) = \begin{cases} -\frac{G_{RO}}{T_{slope}} t & : 0 \leq t < T_{PRE}/2 \\ \frac{G_{RO}}{T_{slope}} (t - \sqrt{2} f_{CAPRI} T_{slope}) & : T_{PRE}/2 \leq t < T_{PRE} + T_{slope} = t_{slope} \\ G_{RO} & : t_{slope} \leq t \end{cases} \tag{6.7}$$

The respective k-space trajectory is calculated according to equation 2.21:

$$k(t) = \begin{cases} -\frac{\gamma}{2\pi} \frac{1}{2} \frac{G_{RO}}{T_{slope}} t^2 & : 0 \leq t < T_{PRE}/2 \\ \frac{\gamma}{2\pi} \frac{1}{2} \frac{G_{RO}}{T_{slope}} (t^2 - 2\sqrt{2} f_{CAPRI} T_{slope} t + f_{CAPRI}^2 T_{slope}^2) & : T_{PRE}/2 \leq t < t_{slope} \\ \frac{\gamma}{2\pi} G_{RO} (t - T_{slope}(1 + \sqrt{2} f_{CAPRI})) + k_{slope} & : t_{slope} \leq t \end{cases} \tag{6.8}$$

where $k_{slope} = k(T_{slope}) = \frac{\gamma}{4\pi} G_{RO} T_{slope} (1 - f_{CAPRI}^2)$ is the k-space value at the end of the gradient ramp. Since data acquisition starts not simultaneously with start of the prephasing gradient, the part of the trajectory required for image reconstruction has to be extracted according to data acquisition timing.

In figure 51 the physical amplifier response to the applied gradients in readout direction is shown for different CAPRI factors (f_{CAPRI}). The black lines correspond to the measured gradients using the trajectory mapping approach introduced in section 5.2. The blue solid line belongs to the calculated gradient using the compensation model from section 5.2.2 to reproduce non-idealities of the real gradient waveform. For trajectory mapping the acquisition is started at the initial slope of the prephasing gradient to ensure start at k-space center and therefore ensure exact initial phase for the unwrapping algorithm.

In the basic imaging sequence the data acquisition starts at the minimal possible echo time for the chosen CAPRI factor. The echo time of the CAPRI sequence can be expressed in terms of the CAPRI factor and the slope duration of the original UTE sequence, and is limited by the dead time of the system:

$$\mathrm{TE}_{min} = \max\left(t_{Dead}, (1+\sqrt{2}) f_{CAPRI} T_{slope}\right) \tag{6.9}$$

While the minimal echo time corresponds at least to the dead time of the system, there exist, a minimal CAPRI factor for each sequence which can be used without affecting the echo time of the sequence. The minimal echo time as a function of the CAPRI factor is plotted in figure 52 for different slope durations T_{slope} and a dead time $t_{Dead} = 50\mu s$. Assuming a gradient strength of $G_{RO} = 20mT/m$ and a slewrate of $200mT/ms$ the ramp duration results in $T_{slope} = 0.1ms$. For the given t_{Dead} the minimal CAPRI factor results in $f_{CAPRI} \approx 0.2$. It should be noted that an increased dead time of the system increases the minimal CAPRI factor. The black dashed line emulate, the minimal TE curve for a dead time of $t_{Dead} = 80\mu s$. The crossing of this line with the original course of the echo time functions yield the minimal CAPRI factor. For the same sequence parameter as before the k-space center could now be shifted to 30% of the slope duration.

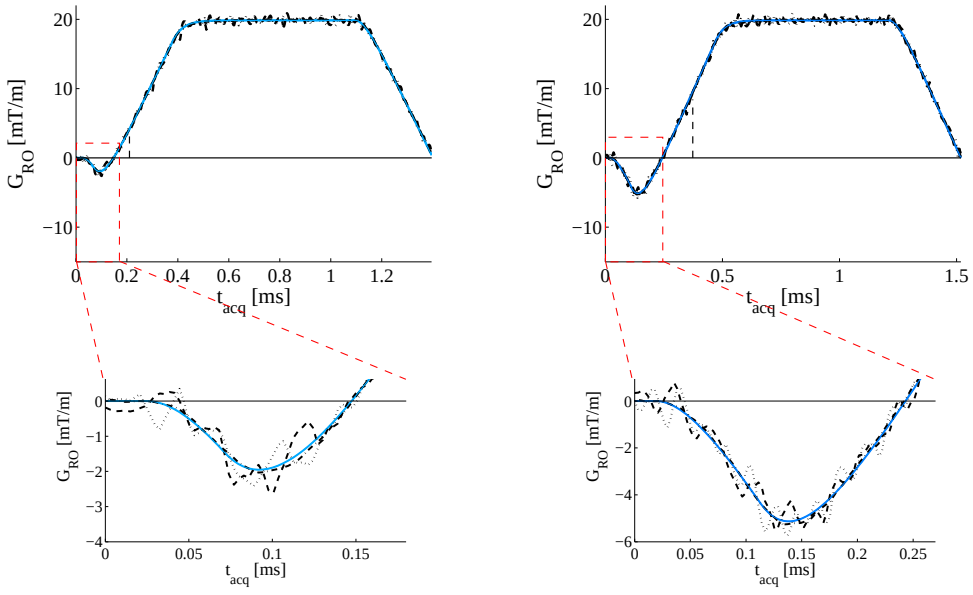

(a) $f_{CAPRI} = 0.25$ **(b)** $f_{CAPRI} = 0.5$

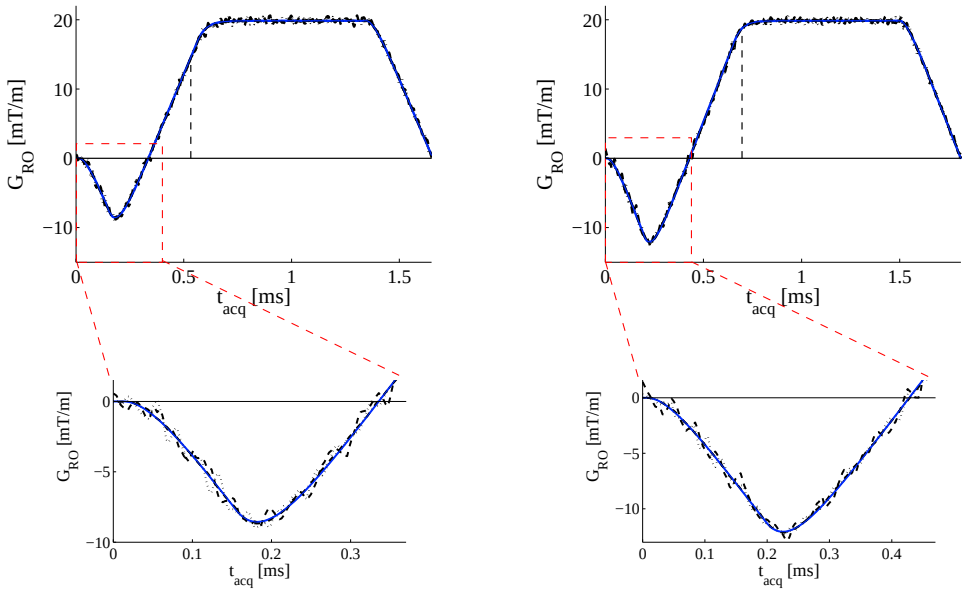

(c) $f_{CAPRI} = 0.75$ **(d)** $f_{CAPRI} = 1$

Figure 51.: Gradient amplifier output for the three gradient axes (black; dotted, dashed, dotted-dashed) and estimated gradient used in the image reconstruction framework (blue solid) for different CAPRI factors.

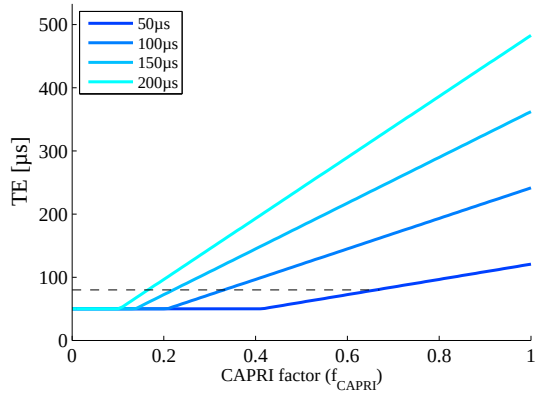

Figure 52.: Minimal echo time of the CAPRI sequence as a function of CAPRI factor f_{CAPRI}. The higher the dead time of the system and the shorter the gradient slope duration, the higher is the CAPRI factor for the minimal echo time as used in UTE imaging.

Different from conventional MR imaging, the time dependent signal behaviours like signal relaxation and phase evolution due to offset frequencies, are no longer proportional to the k-space positions due to non-equidistant k-space sampling during gradient ramp-up. For better understanding of the signal behaviour in non-equidistant k-space sampling the time can be described as a function of k-space position. Equation 6.10 depicts the time dependence during data acquisition as a function of k-space coordinates assuming the start of acquisition at the k-space center:

$$t(k) = \begin{cases} \sqrt{T_{slope}^2 f_{CAPRI}^2 + \frac{2\pi}{\gamma}\frac{2k \cdot T_{slope}}{G_{RO}}} - f_{CAPRI} T_{slope} & : 0 \leq k \leq k_{slope} \\ \frac{2\pi}{\gamma G_{RO}}(k - k_{slope}) + T_{slope}(1 - f_{CAPRI}) & : k_{slope} < k \end{cases} \tag{6.10}$$

The above equation enables the description of discrete sampling as a function of equidistant k-space samples instead of equidistant time samples. The function can be used for simulation of the MTF and respective PSF for various time dependent system characteristics without any influence of non-idealities of the gridding algorithm used for image reconstruction.

By applying a prephasing gradient, the k-space center is sampled at a higher readout gradient and hence much faster than in the conventional UTE technique. Figure 53 shows the time as a function of k-space position for a constant gradient ($f_{CAPRI} = 1$) and the special case of a UTE sequence where the gradient consists only of a ramp. For comparison two fictious reference cases have been introduced: one ramp-only gradient with equal duration as the constant gradient and second - more realistic case - ramp-only gradient with equal maximum strength. In case of same limitations for gradient strength the ramp-only gradient needs twice the time to cover the same k-space area. In case of same acquisition duration the time starts and ends in the same time position for constant gradient and ramp-only gradient, the k-space positions in between are reached further along the timeline for the ramp-only case.

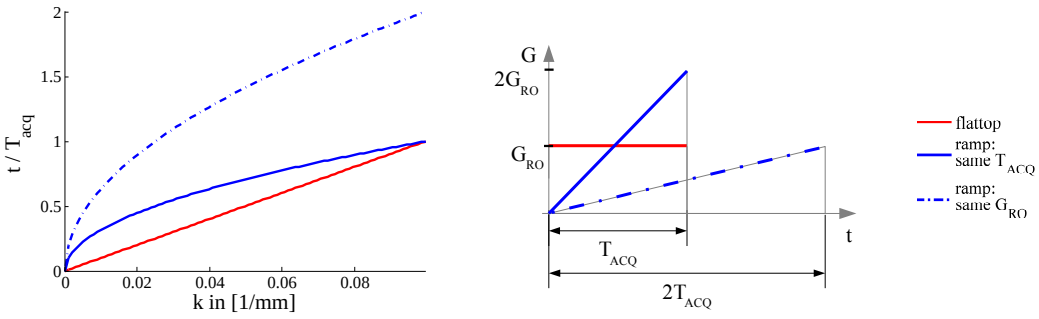

Figure 53.: Timing of constant versus ramp-only gradient: (a) acquisition time as a function of k-space distance for constant gradient (red, solid) versus ramp-only gradient of equal length (blue, solid) and equal maximum strength (blue, dashed-dotted) and (b) the respective gradient waveforms.

For all measurements in this section an improved carotid coil was available with 4 coil elements per side. The coil provides higher SNR and improved coil sensitivity map compared to the prototype coil used in the previous studies (section 5.3). Therefore the jaw could be completly covered in a single scan. The coil offers a slightly increased switching time which shifts the minimal echo time in the range of $\mathrm{TE}_{min} = 70\mu s$.

6.1.1. Impact of T_2^* Relaxation During Acquisition

In this section an analysis of the impact of T_2^* decay during acquisition on the spatial resolution and signal amplitude is given, which can be described by the behaviour of the point spread function in the presence of exponential decay. While the effect on the PSF due to shape and extension of the sampled k-space area only depends on the desired resolution in image space (sec. 5.1.2), the effect in spatial resolution and signal amplitude of the PSF due to T_2^* decay depends on the time dependence of the readout gradient (eq. 6.10). The exponential T_2^* signal decay is described by the following filter function:

$$H_{T_2^*}(t) = e^{\left(-\frac{t}{T_2^*}\right)} \tag{6.11}$$

Since the variable t represents radial distances in spherical coordinates, the 3D fourier expression of the centrosymetric filter can be calculated by the Hankel transformation (eq. 2.31).

In the case of pure flattop sampling and infinite acquisition duration the T_2^* dependend PSF as well as its amplitude and FWHM can be represented in simple analytical expressions [37]. In case of a constant gradient readout ($f_{CAPRI} = 1$) the relation between time and

radial k-values is linear (eq. 2.21) and the filter function results in:

$$H_{T_2^*}(k) = e^{-\left(\frac{2\pi|k|}{\gamma G_{RO}}\frac{1}{T_2^*}\right)} = e^{-\left(\frac{|k|}{k_{max}}\frac{T_{ACQ}}{T_2^*}\right)} \tag{6.12}$$

The amplitude of the related PSF depicts the signal loss due to T_2^* decay and is proportional to the cube of the ratio between relaxation time and readout time, and the T_2^* dependent linewidth can be expressed in the FWHM:

$$FWHM = \frac{2\sqrt{\sqrt{2}-1}}{\pi}\frac{T_{ACQ}}{T_2^*}\Delta r \tag{6.13}$$

where $\Delta r = {}^1/_{2k_{max}}$ represents the voxel size.

In the case of pure ramp sampling the time is a square root function of k-space variable k and the filter function

$$H_{T_2^*}(k) = e^{-\left(\sqrt{\frac{4\pi|k|}{\gamma G_{RO}}}\frac{1}{T_2^*}\right)} = e^{-\left(\sqrt{\frac{|k|}{k_{max}}}\frac{T_{ACQ}}{T_2^*}\right)} \tag{6.14}$$

describes the T_2^* decay during ramp sampling. Unfortunately there exists no closed analytical expression for the Fourier transform of a exponential function with a square-root function as exponent. The PSF for pure ramp sampling can be expressed in terms of a Hypergeometric function (eq. appendix A.1). The amplitude of the PSF results in $PSF_{T_2^*,ramp,inf}(0) = 960\pi k_{max}^3 \left({}^{T_2^*}/_{T_{ACQ}}\right)^6$. The overall PSF and the related FWHM are obtained numerically. To

quantitatively assess the effect of finite k-space sampling ($k_{max} = k(T_{ACQ})$) the total PSF was calculated by solving the finite Fourier integral. The amplitude of the PSF function can be obtained by evaluating the Fourier-Integral for $r = 0$ while the FWHM is obtained numerically. Detailed representation of the whole PSF for pure flattop and pure ramp sampling in the case of infinite and limited k-space sampling is given in appendix A.1.

The MTF as well as the normalized PSF for the exemplary case of $T_{ACQ} = 4T_2^*$ are shown in figure 54 for pure ramp sampling with equal acquisition duration (blue, solid) and pure ramp sampling with equal settings for maximum gradient strength (blue, dotted-dashed) compared to constant gradient settings (red, solid). The MTF ends up in the same signal decay for pure flattop and pure ramp sampling with same acquisition duration but the ramp sampling leads to much higher decay for k-space values near the k-space center compared to pure flattop sampling. In the special case of pure ramp sampling the PSF shows a smaller linewidth compared to flattop sampling with same acquisition duration. Comparing pure flattop and pure ramp sampling for same acquisition settings results in nearly identical FWHM. The pure ramp sampling approach leads to a larger spatial extension of the PSF.

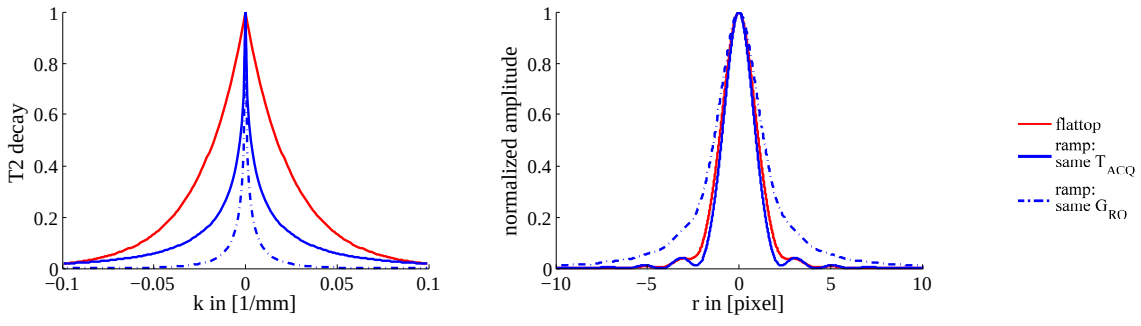

(a) MTF **(b)** PSF

Figure 54.: (a) MTF and (b) PSF in case of pure flattop (red) and pure ramp sampling (blue) for $T_{ACQ} = 4T_2^*$ and limited k-space sampling.

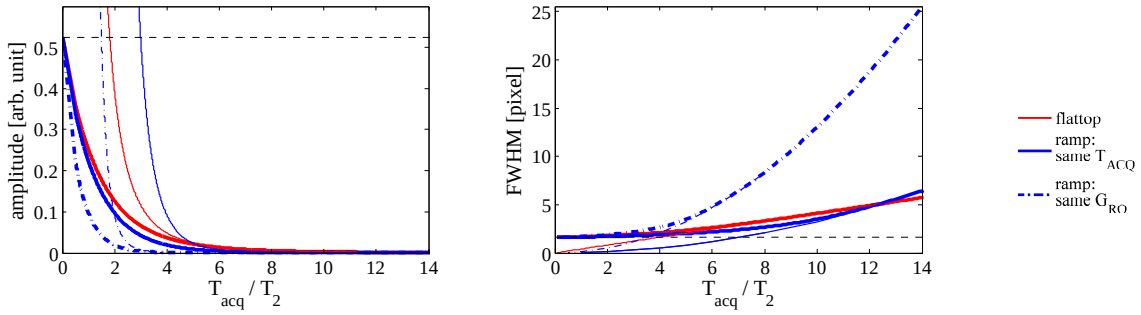

(a) **(b)**

Figure 55.: (a) Amplitude and (b) linewidth of the PSF for pure flattop and pure ramp sampling as functions of T_{ACQ}/T_2^* in case of infinite (thin lines) and limited k-space sampling.

The performance of linewidth and signal amplitude as a function of the ratio between sampling duration and relaxation time is shown in figure 55 for the different gradient settings. The thick lines refer to the total PSF including T_2^* relaxation and limited k-space sampling while the thin lines represent the T_2^* depended blurring function only (infinite k-space sampling). The black dashed line shows the amplitude and FWHM of the point–spread function PSF_{trunc} (eq. 5.11) considering only k-space truncation without any tissue depended system imperfections. For $T_{ACQ}/T_2^* \rightarrow 0$ the influence of T_2^* relaxation can be neglected and the FWHM as well as the amplitude of the PSF from all gradient settings converge to the PSF settings of PSF_{trunc}. For increasing T_{ACQ}/T_2^* the FWHM as well as the PSF amplitude converge to the parameter of the PSF for infinite k-space sampling since the influence on the PSF behaviour of T_2^* relaxation becomes more and more prominent compared to the effect of truncated k-space. Pure flattop sampling results in a maximum signal amplitude of the PSF over the whole range of values compared to both parameter settings for pure ramp sampling and to smaller lineshape over the whole range of values compared to ramp sampling with same maximum gradient strength. In case of same acquisition duration the different dependencies of the FWHM lead to a crossover of the functions for $T_{ACQ} \approx 12.4T_2^*$.

Therefore pure ramp sampling shows less blurring for values below $T_{ACQ} \leq T_2^*$ while for $T_{ACQ} > 12.4T_2^*$ pure flattop sampling shows higher system performance.

Calculations of the PSF amplitude in case of finite flattop (eq. A.3) as well as in case of finite pure ramp sampling (eq. A.7) support the findings of the simulation of a single point object with the simulation framework (sec. 3.3). The simulation results for the FWHM of the PSF could be numerical confirmed for limited pure flattop and pure ramp sampling.

In a real sampling scenario the readout gradient combines the linear rising and the constant gradient part. Therefore the impact between UTE and different CAPRI factors up to pure flattop sampling $f_{CAPRI} = 1$ on the spatial resolution and signal amplitude was investigated for different ratios between duration of the slope and constant part of the gradient. According to the T_2^* simulation in section 5.1.4, the slope duration was defined as a ratio of the acquisition duration $T_{slope} = f_{slope} \cdot T_{ACQ}$. The T_2^* relaxation time was defined as a factor $f_{T_2^*}$ of the acquisition duration for full trapezoidal gradient ($f_{CAPRI} = 0$; UTE).

Figure 56 shows the MTF and PSF exemplarily for $T_{slope} = 0.5T_{ACQ}$ and a relaxation time of $T_2^* = 0.125T_{ACQ}$. The amplitude of the PSF rapidly decreases with decreasing CAPRI

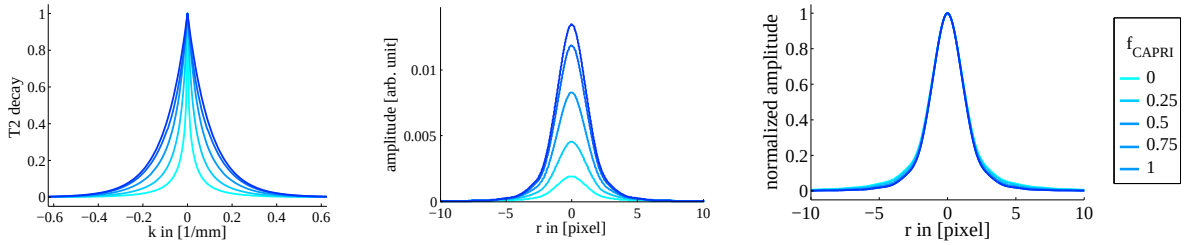

(a) **(b)** **(c)**

Figure 56.: (a) MTF, (b) PSF and (c) normalized PSF for different CAPRI factors using a ramp ratio of $f_{slope} = 0.5$ and a relaxation ratio of $f_{T_2^*} = 0.125$. The normalized PSF reveals nearly same FWHM for all gradient settings but higher spatial extend of the PSF for decreasing CAPRI factor.

factor. The lineshape shows tiny spatial broadening for decreasing CAPRI factor which is clearly revealed by the normalized PSF.

Analysis of the FWHM and the PSF amplitude for different gradient waveform settings revealed a high benefit from the CAPRI sequence for gradient settings with high ramp portion. The T_2^* dependence of the FWHM is shown in figure 57a for gradient rise times between $T_{slope} = {}^1/_8 T_{ACQ}$ and $T_{slope} = T_{ACQ}$ considering only minimal $f_{CAPRI} = 0$ and maximal $f_{CAPRI} = 1$ impact of the CAPRI sequence.

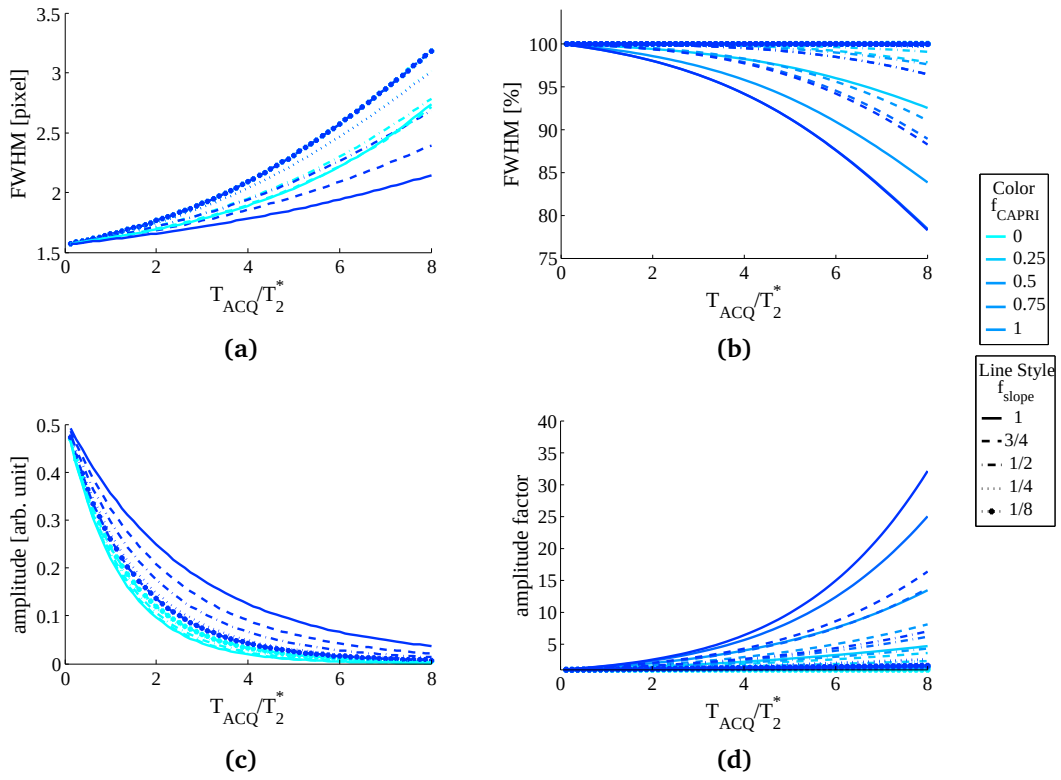

Figure 57.: Impact of partial ramp sampling on PSF amplitude and linewidth for different gradient settings. (a) FWHM and (c) PSF amplitude for conventional UTE (light blue) and pure flattop sampling (dark blue) for different slope durations related to the acquisition duration. (b) FWHM and (d) PSF amplitude for different CAPRI factors in relation to the respective conventional UTE sequence.

The influence of different CAPRI factors on the FWHM is shown in figure 57b relative to the FWHM of the related UTE sequence. Virtually no impact on the lineshape over the whole range of simulated T_2^* values for the different CAPRI factors is observed, when the rise time of the gradient represents less than 0.25% of the acquisition duration. The impact of the CAPRI sequence on FWHM narrowing increases with increasing relaxation time and slope fraction. Figure 57c shows the amplitude of the PSF for conventional UTE ($f_{CAPRI} = 0$) and pure flattop sampling($f_{CAPRI} = 1$) and figure 57d shows the related amplitude gain using different CAPRI factors for multiple gradient settings. The gain of PSF amplitude increases with increasing relaxation time, slope fraction, and CAPRI factor.

The increase in signal amplitude due to faster sampling and due to minimized ramp sampling effects on amplitude, directly competes against the signal loss due to higher echo times compared to basic UTE sequence. The additional signal decay due to the shift of k-space center acquisition depends on the T_2^* relaxation and the slope duration, which were both expressed as ratio of the acquisition duration, and on the CAPRI factor and the dead time of the system, which are both expressed as ratio of the slope duration:

$$I(\mathrm{TE}) = I(t_{Dead}) \cdot e^{\left(f_{CAPRI}\left(1+\sqrt{2}\right) - \frac{t_{Dead}}{T_{slope}}\right)\frac{f_{slope}}{f_{T_2^*}}} \quad : t_{Dead} < \mathrm{TE} \tag{6.15}$$

The impact of increased echo time on signal amplitude is shown in figure 58a, neglecting the dead time of the system (solid line) and assuming a dead time of the system $t_{Dead} = 0.7T_{slope}$(dashed line) for different relaxation times related to the slope duration. Using a gradient amplitude of $20mT/m$ for the constant part and a slewrate of $200mT/ms$ ($T_{slope} = 100\mu s$), the dead time of the system results in $t_{Dead} = 70\mu s$.

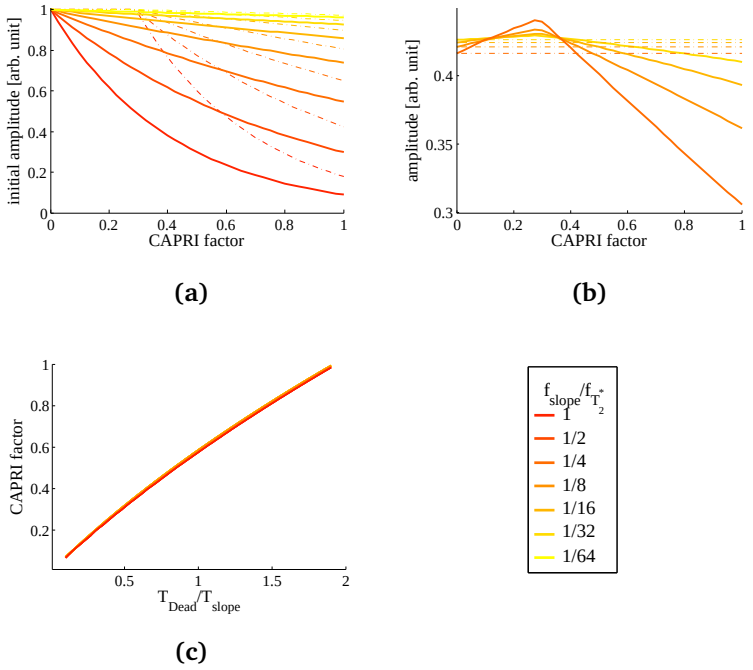

Figure 58.: Effect of increased echo time on the initial signal amplitude at the k-space center. (a) Course of initial signal amplitude for different slope factors and T_2^* relaxation times as function of the CAPRI factor. Solid lines represent the signal decay neglecting the dead time of the system while dashed lines represent a system delay of $t_{Dead} = 70\mu s$. (b) Course of the signal amplitude (solid lines) considering the gain in signal amplitude due to the CAPRI sampling scheme and the signal loss due to the related increase in echo time. Dashed lines represent the amplitude for conventional UTE. Crossing of solid and dashed lines indicate the maximal achievable CAPRI factor $f_{CAPRI,opt}$ without signal loss of the CAPRI sequence compared to UTE. (c) $f_{CAPRI,opt}$ for multiple slope factors and T_2^* times as function of ratio of dead time and slope duration.

The course of the signal amplitude considering the gain in signal amplitude due to the modified sampling scheme and the signal loss due to increased echo time is shown in figure 58b as function of the CAPRI factor for the case of $f_{T_2^*} = 4$ and slope fractions of $f_{slope} = 1/0.5/0.25/0.125$. Dashed lines indicate the respective signal amplitude of the UTE sequence. The signal amplitude reveals a maximum for a CAPRI factor which

provides the same echo time as the UTE sequence. The intersection point of the dashed and solid lines represents the CAPRI factor which can be chosen without any loss in signal amplitude compared to conventional UTE. This optimal CAPRI factor strongly depends on the relation between slope duration and system dead time, and is only insignificantly influenced by relaxation times and slope fractions (fig. 58c).

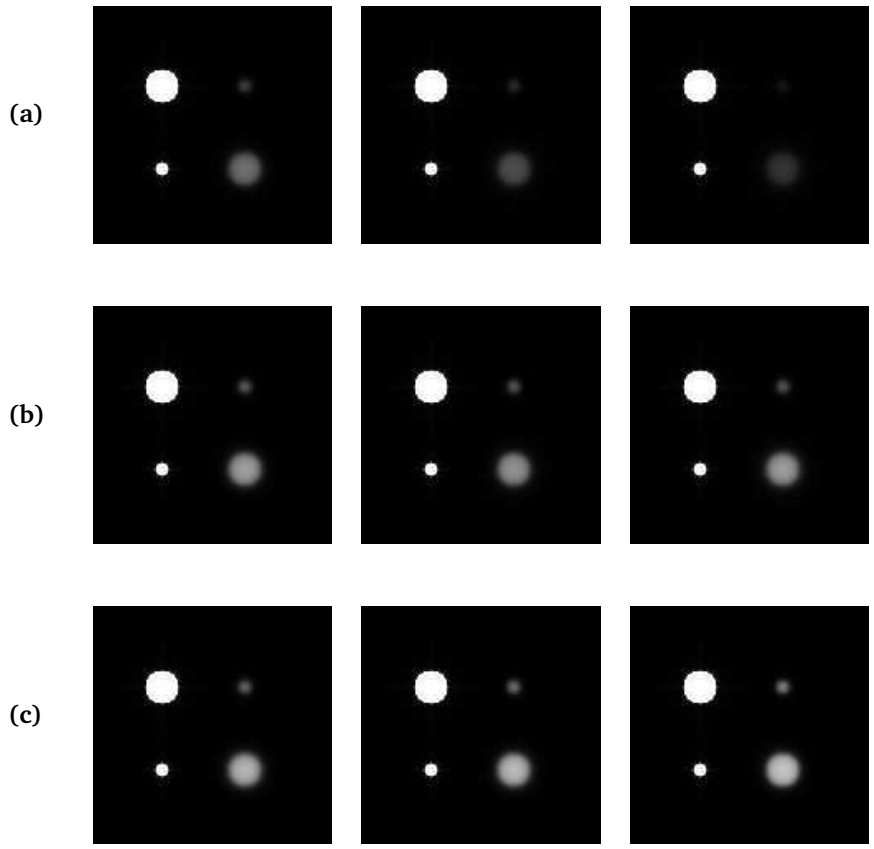

Figure 59.: Simulated effect of T_2^* relaxation for $f_{slope} = 0.125$ (left), $f_{slope} = 0.25$ (mid), and $f_{slope} = 0.5$ (right) for increasing CAPRI factors: (a) $f_{CAPRI} = 0$, (b) $f_{CAPRI} = 0.5$, (c) $f_{CAPRI} = 1$. For each case the objects on the left side are unaffected from transversal relaxation and the objects on the right are influenced by a relaxation factor of $f_{T_2^*} = 8$.

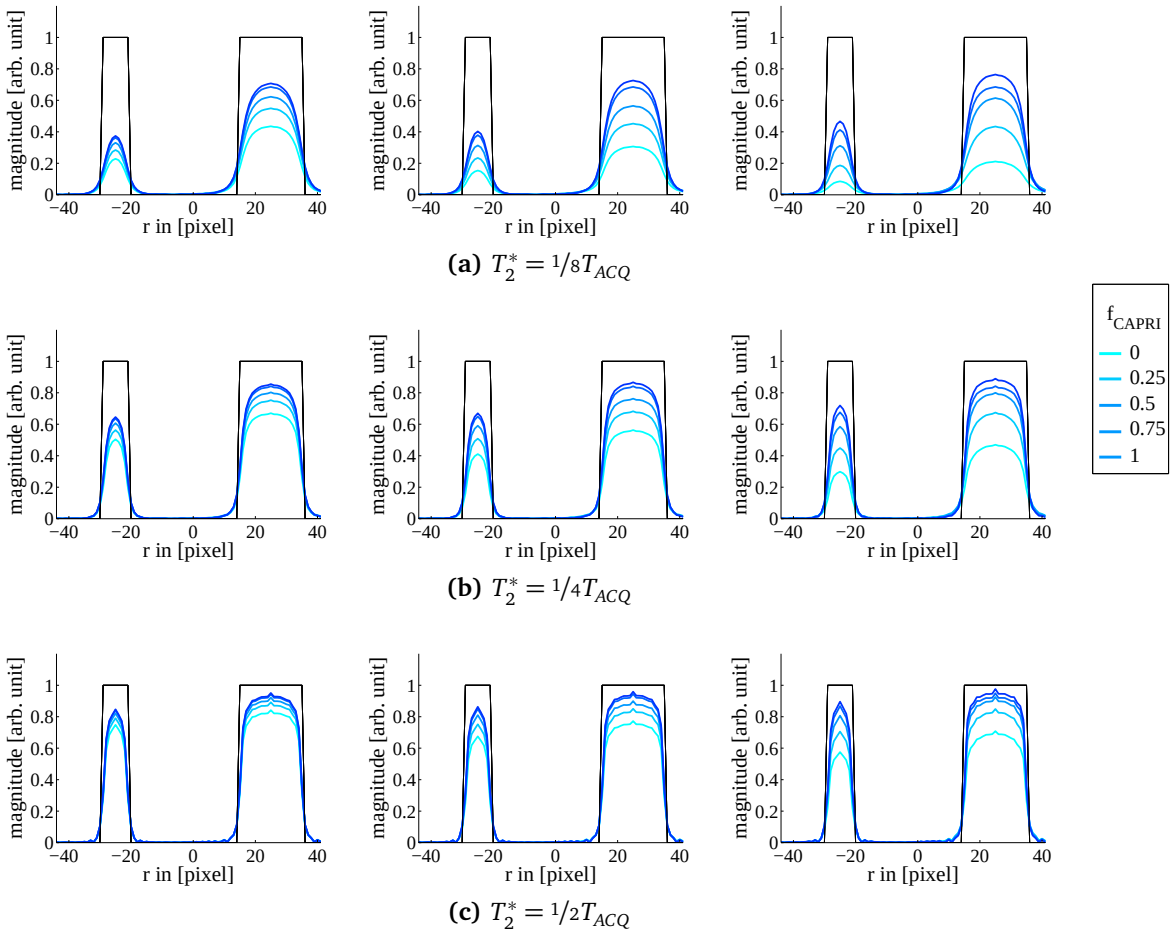

(a) $T_2^* = 1/8 T_{ACQ}$

(b) $T_2^* = 1/4 T_{ACQ}$

(c) $T_2^* = 1/2 T_{ACQ}$

Figure 60.: Profiles of T_2^* affected objects of different size for ramp fractions of $f_{slope} = 0.125$ (left), $f_{slope} = 0.25$ (mid), and $f_{slope} = 0.5$ (right).

The impact of T_2^* relaxation on objects is shown in figure 59 for $f_{T_2^*} = 8$, slope durations of $f_{slope} = 0.125$ (left), $f_{slope} = 0.25$ (mid), and $f_{slope} = 0.5$ (right) and increasing CAPRI factors $f_{CAPRI} = 0/0.5/1$ ((a) - (c)) assuming equal echo times for all settings. The respective profiles of the T_2^* affected tissues are shown in figure 60a. Additionally the profiles for $f_{T_2^*} = 4$ (second row) and $f_{T_2^*} = 2$ (third row) are plotted in figure 60. Since the acquisition duration stays the same for all full trapezoidal gradients (UTE), the drop in signal

amplitude from left to right for $f_{CAPRI} = 0$ is only caused by different slope fractions and not by changing T_2^* relaxation times.

6.1.2. Impact of Off-Resonances During Acquisition

In this section the impact of phase evolution during acquisition caused by a shift of the resonance frequency is investigated. The amount of loss in resolution and signal intensity can be expressed in terms of linewidth, lineshape and signal amplitude of the point spread function. The effect in spatial resolution and signal amplitude due to ω_{off} caused by phase evolution during signal sampling depends on the time dependence of the readout gradient (eq. 6.10). The time-dependent filter function which describes the presence of an offset frequency during acquisition can be expressed by the following equation:

$$H_{\omega_{off}}(t) = e^{\mathrm{i}(\omega_{off} t)} \tag{6.16}$$

In case of pure flattop sampling the k-space is traversed linearly in time and the respective filter function results in

$$\begin{aligned} H_{\omega_{off}}(k) &= e^{\mathrm{i}\left(\omega_{off} \frac{2\pi k}{\gamma G_{RO}}\right)} \\ &= e^{\left(\mathrm{i}\omega_{off} T_{ACQ} \frac{k}{k_{max}}\right)} \end{aligned} \tag{6.17}$$

In case of pure ramp sampling, where the readout gradient is ramped up from zero to G_{RO} at a constant slewrate, the time can be expressed as a function proportional to the square

of the k-space distance, and the filter function which describes the change in phase during acquisition results in:

$$H_{\omega_{off}}(k) = e^{\left(i\omega_{off}\sqrt{\frac{4\pi k}{\gamma G_{RO}}}\right)} \tag{6.18}$$

$$= e^{\left(i\omega_{off}T_{ACQ}\sqrt{\frac{k}{k_{max}}}\right)} \tag{6.19}$$

As mentioned in section 6.1.1, no closed analytical expression of the Fourier transform exists for a filter function of that kind.

Detailed representation of the PSF for pure flattop and pure ramp sampling and the respective representation of the PSF amplitudes are given in appendix A.2.

Figure 61 shows the phase evolution of the MTF and absolute PSF for pure flattop and pure ramp sampling. In case of pure ramp sampling with acquisition duration $T_{ACQ,flattop}$, the overall phase accumulation stays the same as for pure flattop sampling but k-space values acquired near the k-space center experience a much higher phase difference between adjacent samples than those in the k-space peripherie. In case of pure ramp sampling considering same gradient restrictions as in the case of pure flattop sampling, the overall acquisition time and therefore the overall phase accumulation is doubled. The impact on the PSF is plotted for off-resonance values between $f_{off} = 0$ and $f_{off} = {}^{1.8}/_{T_{ACQ,flattop}}$. In all cases the absolute PSF is characterised by a small main lobe and a high spatial extend of the side lobes. The findings for these exemplarily cases are equally valid for the simulated range of off-resonances between $f_{f_{off}} = 0$ and $f_{f_{off}} = 4$ (fig. 62). While the FWHM – which describes the width of the main lobe – decreases with increasing off-resonance, the FWTM – which stands for the spatial influence of the side lobes – continuously increases. Assuming the same gradient restrictions, the width of the main lobe shows much smaller values

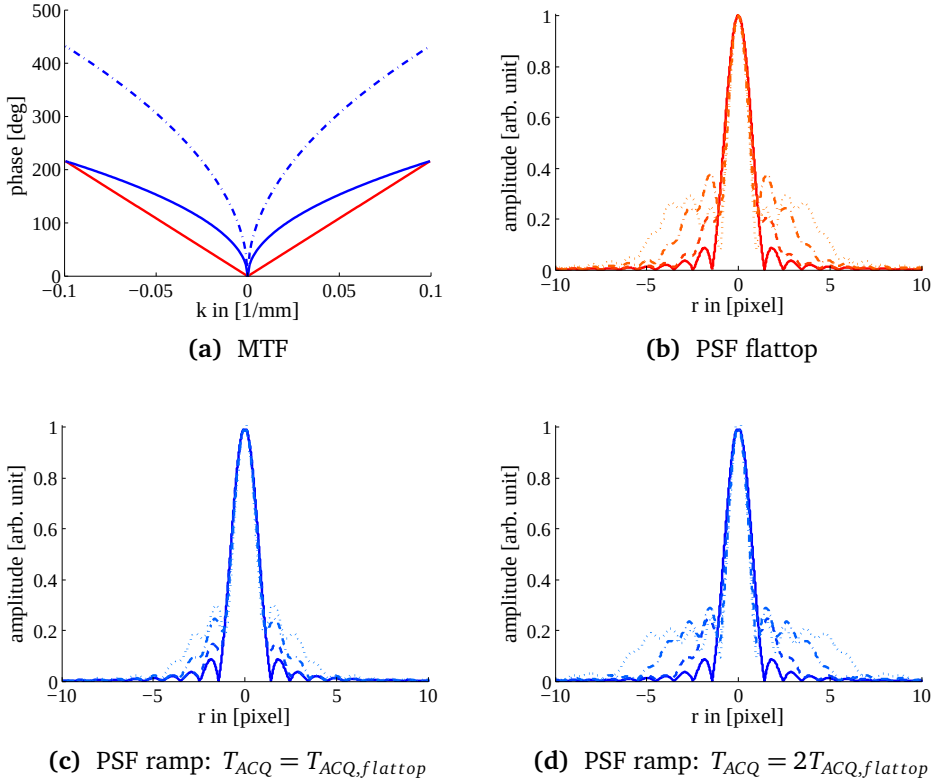

(a) MTF **(b)** PSF flattop

(c) PSF ramp: $T_{ACQ} = T_{ACQ,flattop}$ **(d)** PSF ramp: $T_{ACQ} = 2T_{ACQ,flattop}$

Figure 61.: (a) Phase evolution of the MTF for $f_{off} = {}^{0.6}/_{T_{ACQ,flattop}}$ and evolution of the absolute PSF in case of (b) pure flattop, (c) pure ramp sampling with same acquisition duration and (d) pure ramp sampling with same maximum gradient amplitude for off-resonance values of $f_{off} = 0$, $f_{off} = {}^{0.6}/_{T_{ACQ,flattop}}$, $f_{off} = {}^{1.2}/_{T_{ACQ,flattop}}$, and $f_{off} = {}^{1.8}/_{T_{ACQ,flattop}}$ (solid to dashed).

for pure ramp sampling for off-resonance values below $f_{off} \approx {}^{1.8}/_{T_{ACQ,flattop}}$, while the spatial extend is much higher than for pure flattop sampling over the whole simulation range. For the same case the PSF amplitude shows slightly increased values for pure flattop sampling up to an offset frequency of $f_{off} \approx {}^{1.8}/_{T_{ACQ,flattop}}$ and stays nearly the same as in case of pure ramp sampling for values above. The findings of the system behaviour, regarding PSF amplitude, FWHM and FWTM for pure flattop and ramp sampling, received from the simulation framework (sec. 3.3) were supported by the performance of the calculated PSF from eq. A.11 and A.15.

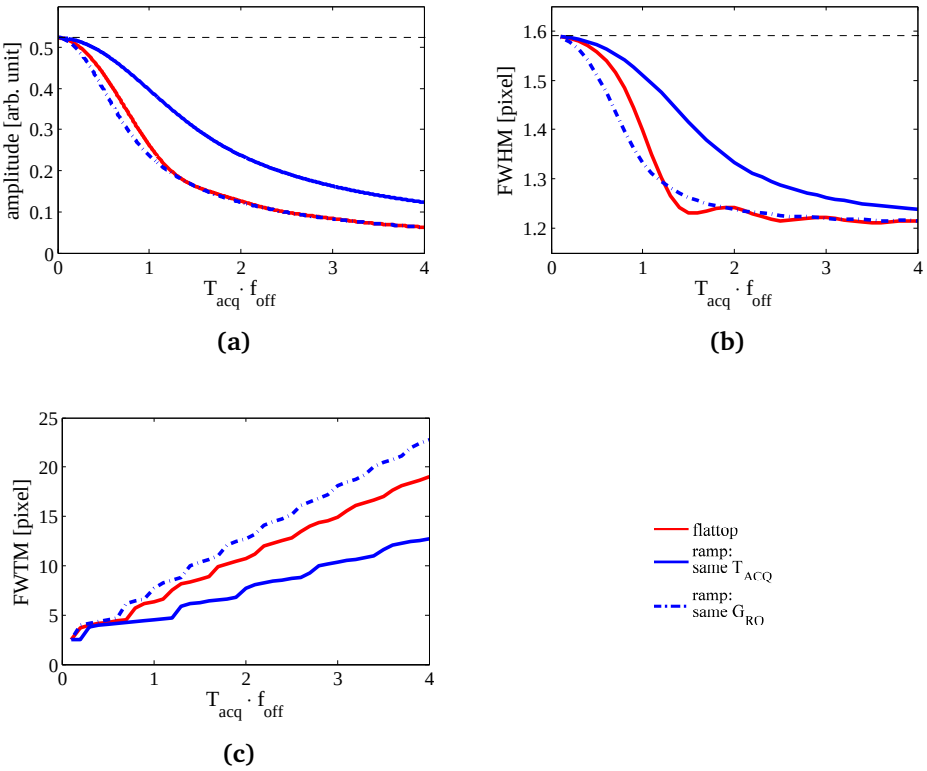

Figure 62.: (a) Amplitude, (b) impact on the main lobe (FWHM), and (c) spatial extend of the side lobes (FWTM) of the PSF for pure flattop and pure ramp sampling as functions of $T_{ACQ} \cdot f_{off}$. While no explicit gain of pure flattop sampling compared to ramp sampling considering same gradient restrictions is observed in PSF amplitude and FWHM, the FWTM is noticeable decreased.

To evaluate the impact of CAPRI acquisition on image quality in the presence of off-resonances, different scenarios of gradient settings regarding the proportion of slope and acquisition duration are simulated. As mentioned before, the off-resonances are specified in terms of the acquisition duration for conventional UTE without partial ramp sampling.

The PSF amplitude and behaviour of the lineshape in terms of FWHM and FWTM are plotted in figure 63. In the left column the amplitude, FWHM and FWTM for pure flattop

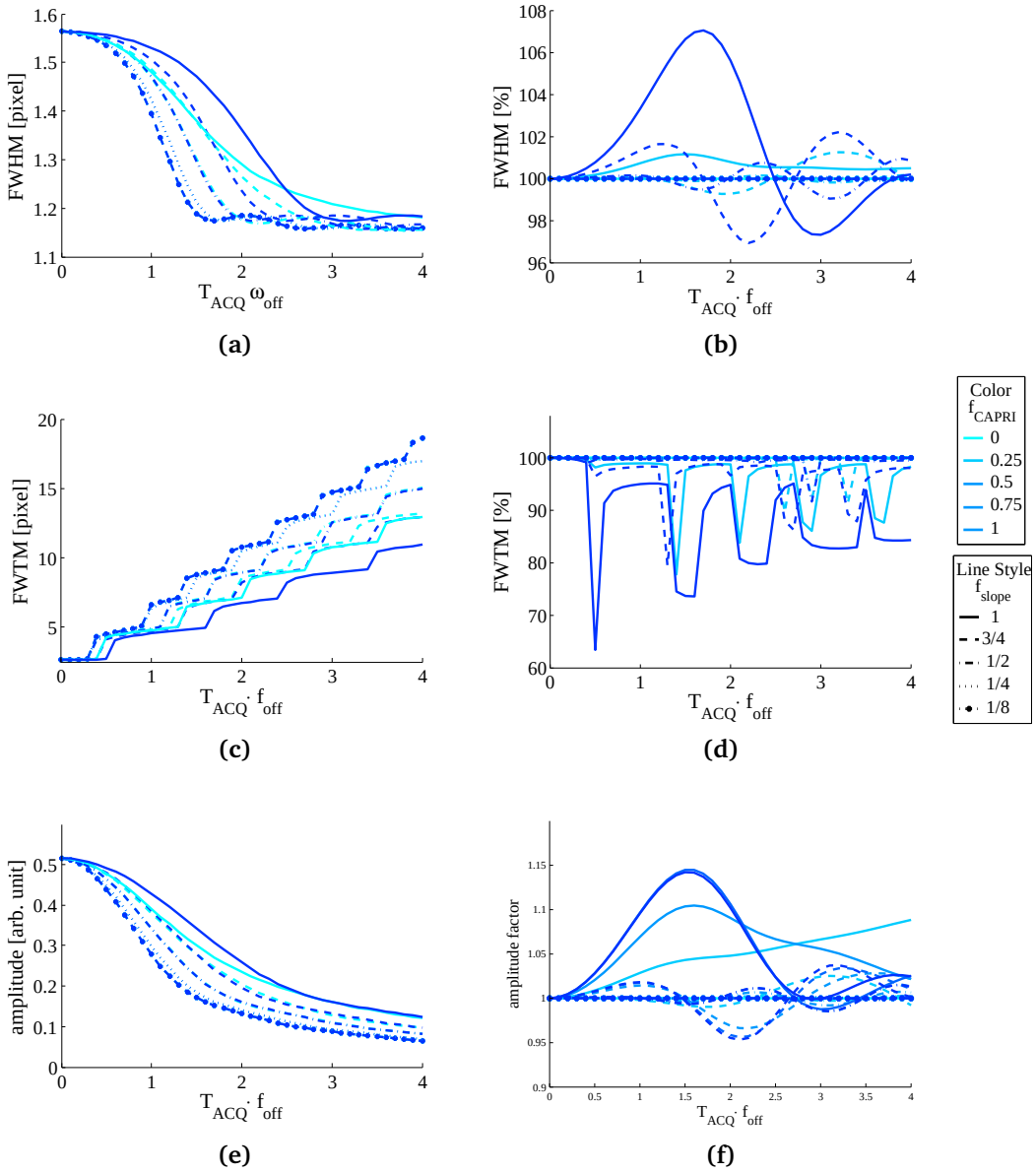

Figure 63.: Impact of partial ramp sampling on PSF amplitude and linewidth for different gradient settings. (a) FWHM and (e) PSF amplitude for conventional UTE (light blue) and pure flattop sampling (dark blue) for different slope durations related to the acquisition duration. (b) FWHM and (f) PSF amplitude for different CAPRI factors in relation to the respective conventional UTE sequence.

(dark blue) and for conventional UTE imaging (light blue) are plotted for an off-resonance range of $f_{off} = 0$ and $f_{off} = {}^{4}/_{T_{ACQ}}$ and slope durations between $T_{slope} = \frac{1}{8} T_{ACQ}$ and $T_{slope} = T_{ACQ}$.

On the right side the respective PSF behaviour is shown as a ratio of the values attained by conventional UTE technique. In contrast to the T_2^* related PSF performance – where a continuous change in signal amplitude and FWHM compared to the behaviour from conventional UTE imaging technique is observed – the benefit of the CAPRI sequence strongly depends on the relation between the existing off-resonance and the acquisition duration. Both the signal amplitude and the FWHM show a wavelike behaviour and alternate positive and negative impact from the CAPRI sequence. It can be observed that in nearly all cases the gain in signal amplitude leads to an increased linewidth of the main lobe and vice versa. The FWTM for slope factors of $f_{slope} = 0.25$ or below shows only neglecting benefit for all CAPRI factors. While only a small gain is observed for $f_{slope} = 0.5$, a gain up to 35% and 20% is obtained respective for $f_{slope} = 0.75$ and $f_{slope} = 1$. The FWTM shows a high impact from CAPRI sequence for defined intervals. Between these intervals the amplitude of the side lobes increases with increasing off-resonance.

The impact on objects of additional phase evolution during acquisition, caused by a precession frequency with an offset from the center frequency is shown in figure 64. The used simulation settings include an offset frequency of factor $f_{f_{off}} = 0.8$, varying slope durations with relation to the acquisition duration of $f_{slope} = 0.125$ (left), $f_{slope} = 0.5$ (mid), and $f_{slope} = 1$ (right) and increasing CAPRI factors $f_{CAPRI} = 0/0.5/1$ ((a) - (c)). For all settings the timing is chosen to ensure similar echo times for the different gradient settings and therefore the impact of phase accumulation in front of acquisition start is neglected. The respective profiles of the off-resonance affected tissues are shown in figure 65. Where the rows represent the profiles measured at different slope factors and the columns from left to right represent the absolute, real and imaginary part of the object. In case of a slope

fraction of $f_{slope} = 0.125$ only small changes in real and imaginary part are observed for the different ramp sampling settings while for slope values of $f_{slope} = 0.5$ and $f_{slope} = 1$ the acquisition duration shows strong modulations of both the real and imaginary part of the object. The absolute representation of the profile shows only minor variations for the different CAPRI factors.

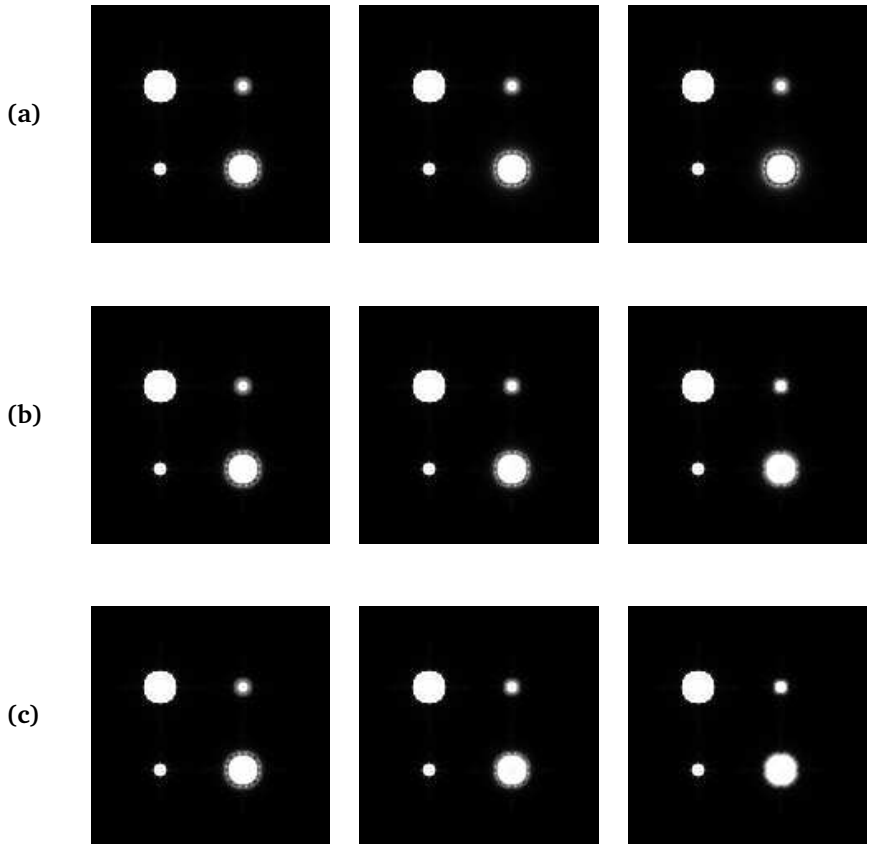

Figure 64.: Simulated effect from the presence of an offset frequency during acquisition for a ramp factor of $f_{slope} = 0.125$ (left), $f_{slope} = 0.5$ (mid), and $f_{slope} = 1$ (right) for increasing CAPRI factors (a) $f_{CAPRI} = 0$, (b) $f_{CAPRI} = 0.5$, and (c) $f_{CAPRI} = 1$. For each case the objects on the left side are unaffected from additional phase variation and the objects on the right are influenced by an off-resonance of value $f_{off} = {}^{0.8}/_{T_{ACQ,min}}$. The respective profiles of the off-resonance affected tissues are plotted in fig. 65.

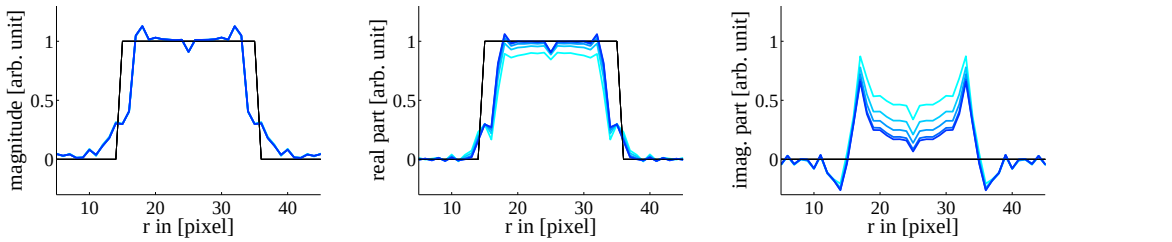

(a) $f_{slope} = 0.125$

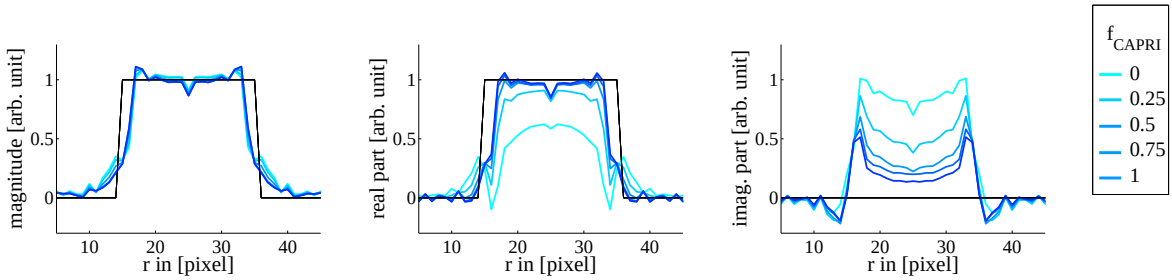

(b) $f_{slope} = 0.5$

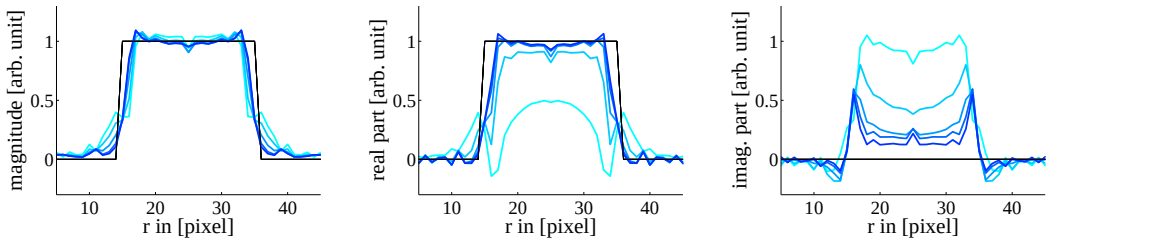

(c) $f_{slope} = 1$

Figure 65.: Absolute (left), real (mid) and imaginary (right) part of the profiles from the off-resonance affected objects of different size for ramp fractions of (a) $f_{slope} = 0.125$, (b) $f_{slope} = 0.5$, and (c) $f_{slope} = 1$.

Figure 66 presents the measurement results for a gradient slope duration of 0.5% of the acquisition duration and offset frequencies of $f_{off} = {}^{0}/_{T_{ACQ,min}}$ (left), $f_{off} = {}^{0.4}/_{T_{ACQ,min}}$ (mid), and $f_{off} = {}^{0.8}/_{T_{ACQ,min}}$ (right), where the minimum acquisition duration is defined as the acquisition duration for the case of pure flattop sampling ($f_{CAPRI} = 1$: $T_{ACQ,min} = T_{ACQ,flattop}$). The phantom measurements confirm the theoretical findings. The impact on the image

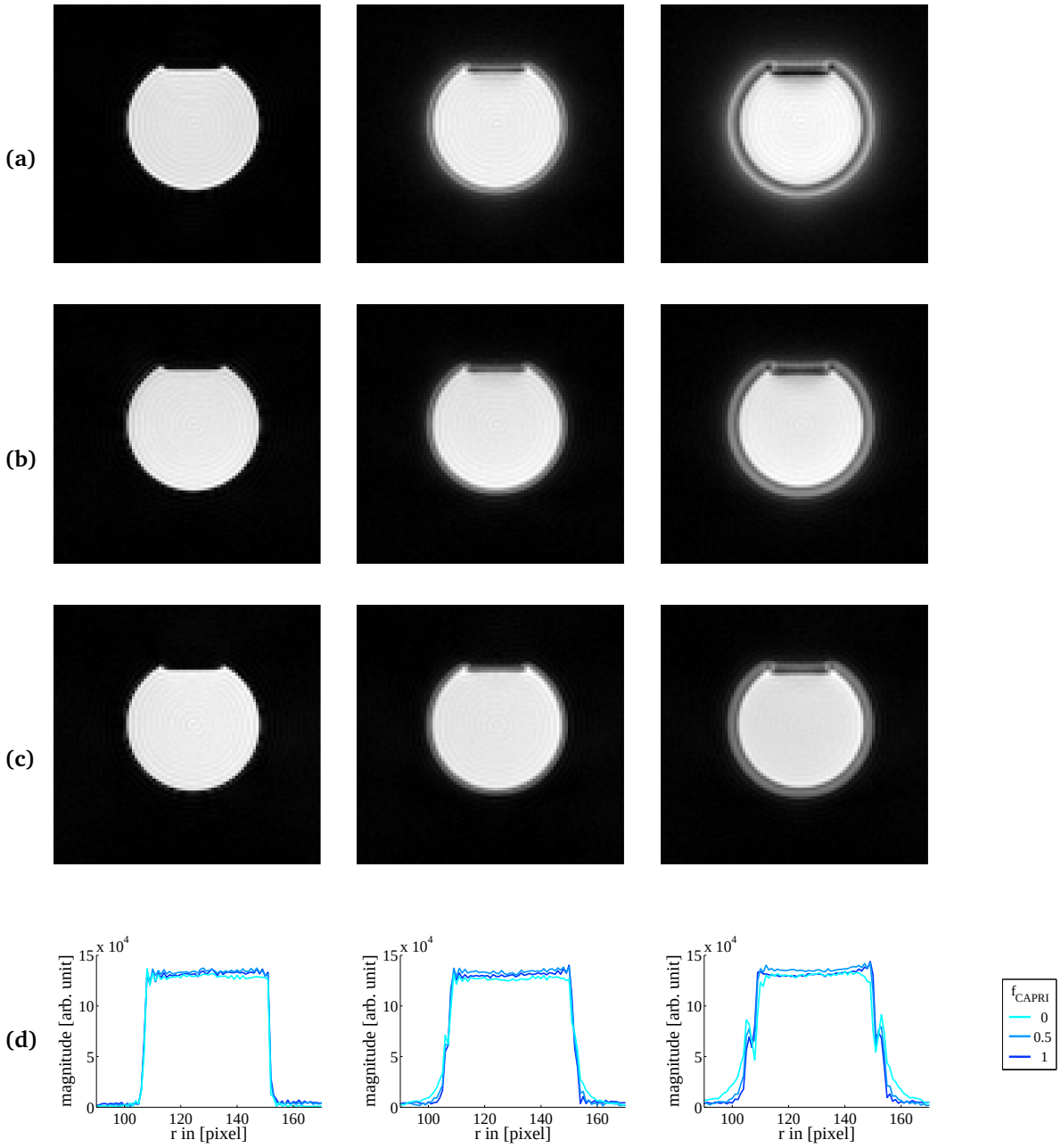

Figure 66.: Measurement results for a ramp factor of $f_{slope} = 0.5$ and offset frequencies during acquisition of $f_{off} = {}^{0}/_{T_{ACQ,min}}$ (left), $f_{off} = {}^{0.4}/_{T_{ACQ,min}}$ (mid), and $f_{off} = {}^{0.8}/_{T_{ACQ,min}}$ (right): reconstructed images for increasing CAPRI factors (a) $f_{CAPRI} = 0$, (b) $f_{CAPRI} = 0.5$, and (c) $f_{CAPRI} = 1$ and (d) the respective profiles of the off-resonance affected tissues.

quality in the presence of an offset frequency – represented by a halo around the object – is significantly reduced for increasing CAPRI factors due to the related reduced acquisition durations. A comparison of the profiles (fig. 66d) for different CAPRI factors reveals the impact on smoothing and repetition of the edges (fig. 66a: $f_{CAPRI} = 0$, fig. 66b: $f_{CAPRI} = 0.5$, and fig. 66c: $f_{CAPRI} = 1$).

6.1.3. SNR Considerations

According to the derivation in section 3.4 the SNR can be specified by the image resolution, and the overall acquisition time of the measurement:

$$SNR(\vec{x}) \propto \Delta x \Delta y \Delta z \cdot \sqrt{T_{ACQ} N_y N_z}.$$

The volume of a single voxel $V_s = \Delta x \Delta y \Delta z$ in the image domain as well as the total number of radial profiles $N_y N_z$ stay the same for the different CAPRI factors and the Signal-to-Noise ratio is only affected by the acquisition duration. The acquisition duration of a conventional UTE sequence is given by the duration of the ramp and the constant part of the readout gradient $T_{ACQ} = T_{slope} + T_{const}$ while the acquisition duration of CAPRI sequences is given by equation 6.6. The relative SNR of the CAPRI sequence compared to conventional UTE imaging therefore results in:

$$SNR_{CAPRI}(f_{CAPRI}) = \sqrt{\frac{T_{const} + T_{slope}(1 - f_{CAPRI} + f_{CAPRI}^2/2)}{T_{const} + T_{slope}}} \cdot SNR_{UTE} \tag{6.20}$$

$$= \sqrt{\frac{\frac{1}{f_{slope}} + (1 - f_{CAPRI} + f_{CAPRI}^2/2)}{\frac{1}{f_{slope}} + 1}} \cdot SNR_{UTE}$$

Figure 67 shows the loss in SNR for different relations between acquisition and slope duration. The complete dependence of the single-voxel SNR, considering decreases in signal amplitude due to variable echo times and different behaviours of PSF amplitude for the different CAPRI factors, can be obtained from the total PSF amplitude weighted by the given SNR in equation 6.20.

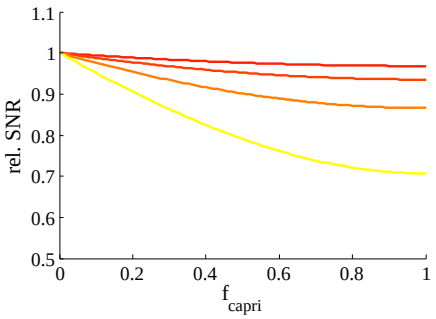

Figure 67.: Signal-to-noise-ratio for $f_{slope} = 0.125/0.25/0.5/1$ (red to yellow), neglecting amplitude variations for the different CAPRI factors due to T_2^* relaxation.

6.2. Automatic Delay Correction using CAPRI

Center-out imaging sequences like UTE are very sensitive to waveform distortions and shifts of the k-space trajectory. The accurate knowledge of the gradient delay is essential to obtain adequate image quality for center-out imaging techniques like UTE and CAPRI. Until now there exists no direct approach to measure the associated shift of the echo top of the k-space signal and usually additional reference scans are used to obtain the gradient delays

[1,44]. In this section a CAPRI-based automatic delay correction method is introduced to determine the delays by direct measurement of the echo peak shift.

For the correction approach the signal acquisition is started in front of the k-space origin. Therefore a partial echo can be acquired and used for the detection of echo peak. Figure 68 shows the impact of gradient delay to the gradient timing of the CAPRI sequence.

The delay of the k-space trajectory can be calculated by comparing the theoretical time of the k-space center

$$t_{k_0} = \left(1 + \sqrt{2}\right) f_{CAPRI} \cdot T_{slope}$$

to the real time

$$t_{peak} = t_{k_0} + T_D$$

of the k-space center crossing. To estimate the time position of the echo peak (t_{peak}) a continuous k-space signal was generated by using a piecewise polynomial form of cubic spline interpolation and the maximum intensity (I_{max}) along the k-space profile was detected:

$$t_{peak} = t_{ACQ}(I_{max}).$$

The theoretical time of k-space center was computed by determining the zero-crossing of the waveform approximation k-space trajectory. Finally the gradient delay for a single

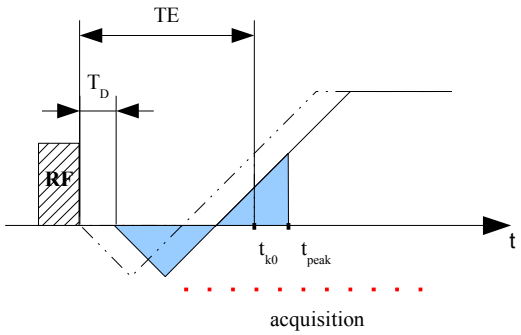

Figure 68.: 3D CAPRI sequence: Pulse sequence diagram considering gradient delays. Since the prephasing gradient is affected by the same gradient delay as the readout gradient a delay results in a shift of the k-space trajectory.

k-space profile was determined from the difference between theoretical and real k-space center crossing:

$$T_D = t_{k_0} - t_{peak}.$$

The presence of linear off-resonances – which can be considered as an additional constant gradient G_{off} – moves the k-space trajectory in direction of this inhomogeneity gradient. Hence the echo peak is shifted in opposite direction for positive and negative amplitude of the readout gradient:

$$\vec{k(t)} = \begin{cases} \vec{k_D}'(t) + \vec{k_{off}}(t) & : G_{RO} \leq 0 \\ \vec{k_D}'(t) - \vec{k_{off}}(t) & : G_{RO} > 0 \end{cases} \tag{6.21}$$

The first term $\vec{k}_D{}'$ represents the trajectory calculated from the waveform corrected readout gradient and the k-space dependence of the linear off-resonance is given by $k_{off}(t) = \frac{\gamma}{2\pi} G_{off}\, t$.

Figure 69 shows the impact of a linear off-resonance G_{off} on the k-space sampling for G_{off} having opposed (fig. 69a) and same (fig. 69b) sign of gradient amplitude as the readout gradient.

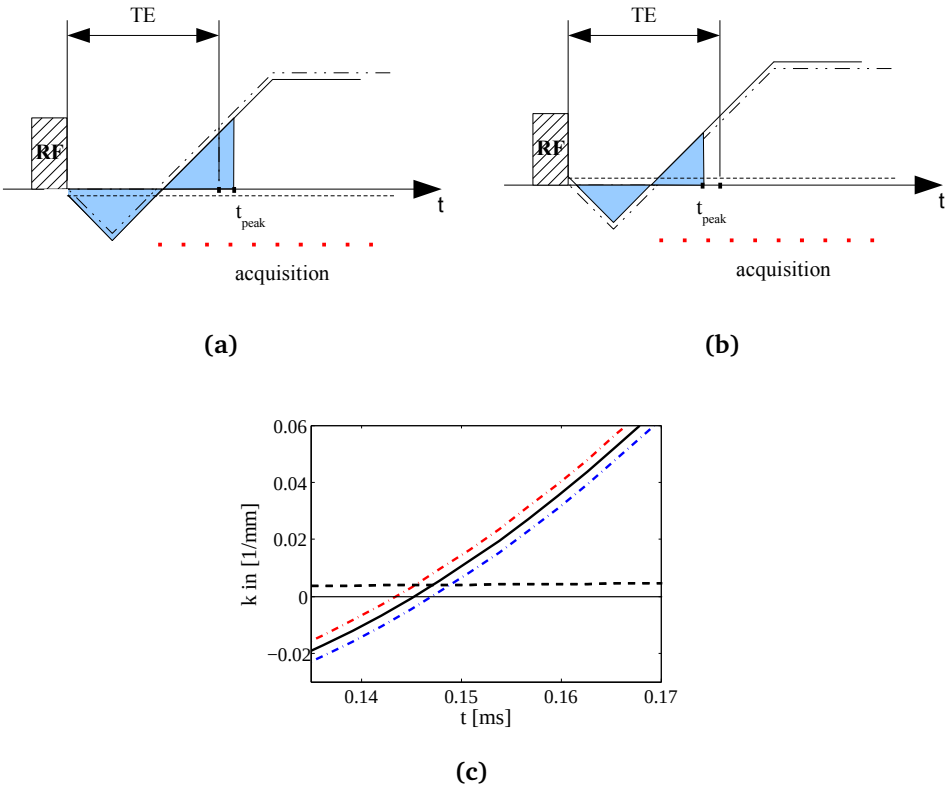

Figure 69.: Impact of a linear off-resonance G_{off} on the echo peak position, considering G_{off} having (a) opposed and (b) same sign as the readout gradient G_{RO}. (c) Deviation of k-space trajectory considering a linear off-resonance (black, dashed). The crossing of the k-space center for the estimated trajectory (black, solid) deviates from crossing of the off-resonance affected trajectories (dashed-dotted). The center crossing is postponed for equal signs (blue) and preponed for opposed signs (red) of the gradients G_{RO} and G_{off}.

Figure 69c shows the deviation of k-space trajectory considering a linear off-resonance of $G_{off} = 0.1mT/m$ at a readout gradient strength of $G_{RO} = 20mT/m$, a slewrate of $S_{RO} = 200mT/ms$, and a CAPRI factor of $f_{CAPRI} = 0.5$. The shift of k-space due to linear off-resonances leads to different times of k-space center crossing for opposed k-space profiles. This results in related different delay values for the gradient channels considering positive or negative gradient amplitudes. In the presence of off-resonance the delay correction algorithm based on pure peak detection therefore can fail to act for an off-resonance affected k-space profile.

Since the impact of the linear off-resonance on the k-space trajectory is time dependend ($k_{off} = G_{off} \cdot t$), the impact is much higher for the postponed k-space center crossing ($t_{k_0} > t_{peak}$) than for the preponed ($t_{k_0} < t_{peak}$) and the echo peak is not shifted by the same amount of time for opposed profiles (see fig. 69). Assuming $t_{k_0,1}$ and $t_{k_0,2}$ as peak times of opposed profiles and the precondition that $k(t_{peak}) = 0$ equation 6.21 results in:

$$\vec{k}(t_{peak}) = 0 = \begin{cases} \vec{k_D}'(t_{k_0,1}) + \frac{\gamma}{2\pi} G_{off}\, t_{k_0,1} & : G_{RO} \leq 0 \\ \vec{k_D}'(t_{k_0,2}) - \frac{\gamma}{2\pi} G_{off}\, t_{k_0,2} & : G_{RO} > 0 \end{cases} \tag{6.22}$$

By equalizing the above equations for a single k-space profile the following condition can be received:

$$\frac{t_{k_0,1}}{t_{k_0,2}} = \frac{k'_D(t_{k_0,2})}{k'_D(t_{k_0,1})}. \tag{6.23}$$

The equation is satisfied using the actual gradient delay for calculation of the delayed trajectory $k'_D(t)$.

Since it is much more time efficient using the mean delay $T_{D,mean} = (t_{k_0,1} - t_{k_0,2})/2$ from opposed k-space profiles instead of using equation 6.23, a error estimation for both approaches was performed. The resulting k-space delay for different values of linear off-resonances and multiple gradient settings were emulated. For the analysis the theoretical time of k-space center crossing of the profiles was calculated and the gradient delays were calculated by both, solving equation 6.23 for each parameter set, and using the mean delay of opposite k-space profiles. The simulation parameters were chosen as follows: a gradient delay range between $0\mu s$ to $10\mu s$ in steps of $2\mu s$, a gradient amplitude range between $20mT/m$ and $30mT/m$ in steps of $5mT/m$, a gradient slewrate range from $50mT/ms$ to $200mT/ms$ in steps of $50mT/ms$ and multiple off-resonances between $0mT/m$ and $0.5mT/m$ in steps of $0.1mT/m$.

In cases where the k-space center crossing is shifted in front of the acquisition start, no estimation for gradient delay is possible for both approaches. For CAPRI factors equal or greater than $f_{CAPRI} = 0.5$ the deviation from the estimated to the used gradient delay results in less than $0.5\mu s$ for both delay calculation approaches. Using the complex delay estimation, the gradient delay for $f_{CAPRI} = 0.25$ and slewrates of $50mT/ms$ and $100mT/ms$ results in delay deviation of about 1 and $1.5\mu s$. Using mean delay for absolute gradient channel delay calculation with $f_{CAPRI} = 0.25$ and $G_{off} \leq 0.3mT/m$ half of the delay calculations result in deviations of more than $0.5\mu s$ while only an eighth in deviations of more than $1\mu s$. A great benefit of the time consuming approach is only observed for CAPRI factor $f_{CAPRI} = 0.5$ in the presence of $G_{off} \leq 0.3mT/m$. Therefore the mean gradient delay approach was chosen as default calculation method.

Two different approaches of delay compensation were investigated in this work. For the first approach the system delays are determined for every measured profile as mentioned

above. The trajectory for every single profile is calculated by

$$k_D(t,n) = \frac{\gamma}{2\pi} \int_0^t G_{RO}\big(\tau - T_D(n)\big)\,\mathrm{d}\tau \tag{6.24}$$

and convolved with the exponential system impulse response from section 5.2.2. The Off-resonance related echo peak shifts are eliminated by calculating the k-space trajectory for the mean gradient delay of projections in opposite readout directions. This approach is very time consuming since every k-space raw data profile underwent the delay identification routine and every trajectory profile has to be calculated independently with a different gradient delay. A much more time efficient approach is to calculate the gradient delays and respective k-space trajectory profiles for the three main axes only. The correction for linear frequency offset was applied individually for the three gradient channels. The whole kooshball trajectory was calculated by using tri-linear interpolation of the three k-space profiles of the main axes.

For evaluation of image quality improvement, the delay compensation algorithms were applied to various ex-vivo measurements considering multiple gradient settings. Measurements were performed for gradient amplitudes of $G_{RO} = 20/25/30mT/m$ and gradient slewrates of $S_{RO} = 100/150/200mT/ms$. CAPRI factors between $f_{CAPRI} = 0$ (UTE) and $f_{CAPRI} = 1$ are applied in steps of 0.25. For CAPRI factors smaller than $f_{CAPRI} \leq {}^{t_{Dead}}/(\sqrt{2}T_{slope})$ the rising slope starts before the system dead time is reached and the acquisition start is chosen to t_{Dead}. Elsewise the start of acquisition is shifted to the beginning of the rising slope of the readout gradient. For image reconstruction the data points sampled prior to k_0 are discarded, to avoid mixed k-space data weighting and impact of digital filter imperfections during the first readout points. To get close-to in-vivo measurement settings a grapefruit was chosen as phantom due to the various susceptibility (air-tissue) interfaces. Therefore the presence of linear off-resonances and related shift in k-space position can be assumed.

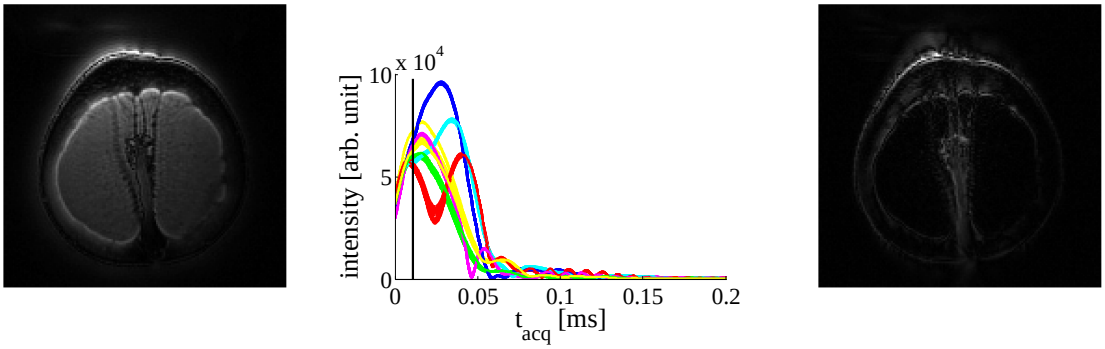

(a)

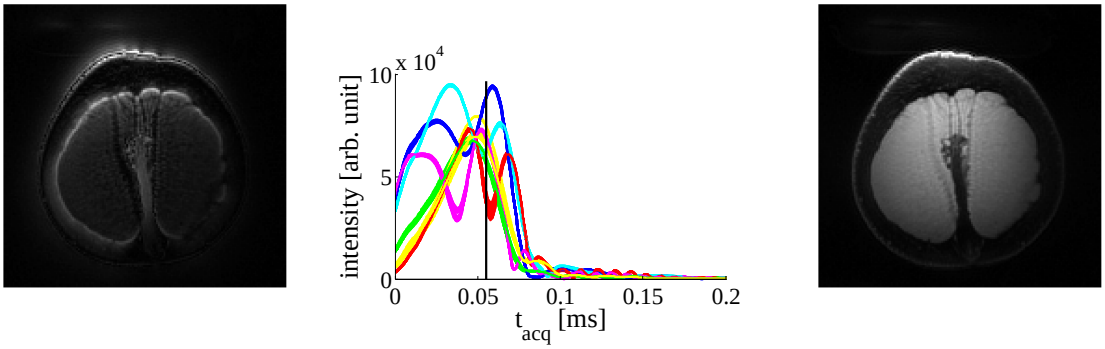

(b)

Figure 70.: Reconstructed images without delay correction (left) and using the detected delays (right) for (a) $f_{CAPRI} = 0.25$ and (b) $f_{CAPRI} = 0.5$ using a maximum gradient strength of $G_{RO} = 25mT/m$ and a slewrate of $200mT/ms$. Delay correction for opposed k-space profiles (mid) for x-axis (green, yellow), y-axis (red, magenta), and z-axis (blue, cyan) failed for $f_{CAPRI} = 0.25$ due to the incorrect detection of maximal echo peak.

Reconstructed images are shown in figure 70 for non-applied delay correction (left) and automatic delay correction approach using the default settings (right). The delays for the three main gradient axes were caluclated from the profiles shown in the middle. The profiles are plotted pairwise for opposed k-space profiles for x-axis (green, yellow), y-axis (red, magenta), and z-axis (blue, cyan). In the case of $f_{CAPRI} = 0.25$ the delay detection

approach failed since the peak of the cyan profile is shifted out of T_{ACQ} and the maximal echo peak of the red profile is affected by digital filter build up.

For CAPRI factors greater than or equal to $f_{CAPRI} = 0.5$ the automatic delay compensation algorithm worked well. For a CAPRI factor of $f_{CAPRI} = 0.25$ it was observed that in cases with high slewrates the echo top was either shifted in front of the acquisition start due to linear off-resonances, or the signal amplitude of the echo peak was not the maximum peak of the profile. This drop in signal amplitude for the first echo peak indicates that the digital filter is still in the transient state at start of acquisition and therefore the first samples are affected. In both cases the algorithm detected none or the wrong peak for echo estimation and the determination of gradient delay failed. In all of these cases the time between theoretical crossing of k-space center and start of rising slope was below $42\mu s$ and difference between center crossing and start of acquisition was below $30\mu s$.

Figures 71 and 72 represent the findings of the in-vivo measurements. The delay distribution along a kooshball interleave is shown in figure 71 for individual delay calculation for each profile (blue) and linear combination of the delays for the three main gradient axes (red). Reconstructed images for the different settings of the automatic delay correction approach are shown in figure 72.

The characteristics of the uncorrected delays show an oscillation at $0\mu s$ for the first half of the kooshball interleave and at $-10\mu s$ for the second. The existing off-resonances lead to delay deviation of about $15\mu s$ for the single profile approach. In case of delay calculation from the three main gradient axes the delay varies between -10 and $15\mu s$. The respective images 72e and 72c therefore suffer from image degradation.

Using the off-resonance correction approach the resulting delay oscillates around $5\mu s$ in both cases, with an amplitude of $\pm 1\mu s$ for the single profile approach and $\pm 0.3\mu s$ for tri-linear interpolation of the main gradient delays. The respective images 72f and 72d

show comparable good image quality. Differences between the reconstructed images using detected and calculated off-resonance-corrected delays appear negligible.

Using the mean delay of all profiles as indicated in the abstract of Krämer et al. [29] does not lead to severe image degradation as in the non-off-resonance corrected cases but still affects image quality in form of repetition of the edges (fig. 72b, red arrow).

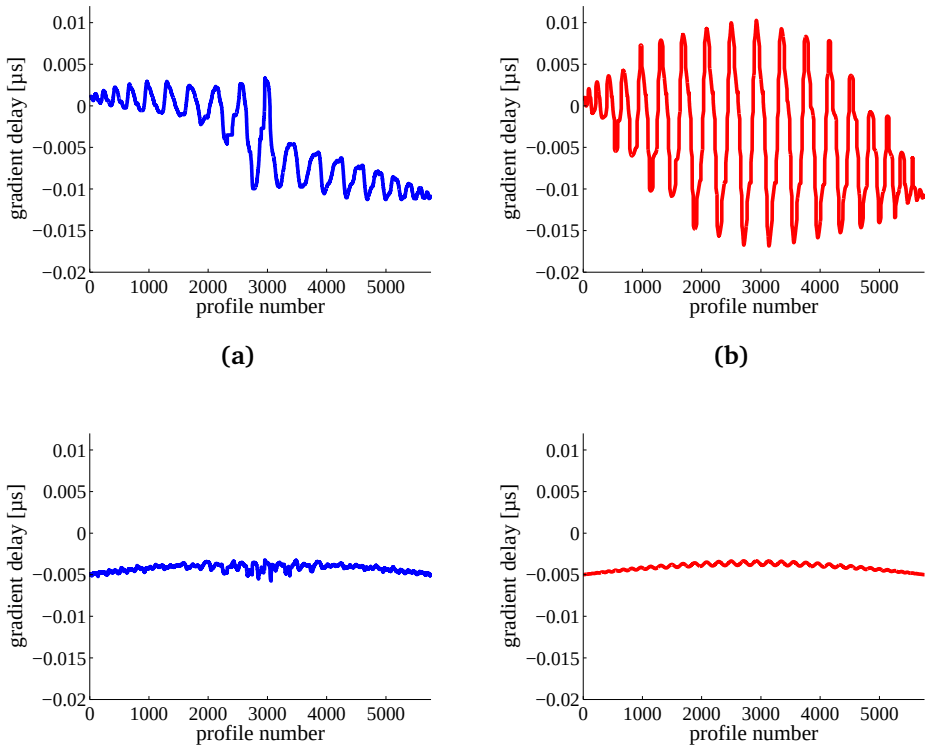

Figure 71.: Characteristics of calculated delays along a single kooshball interleave using individual delay calculation for each profile (blue) and linear combination of the delays for the three main gradient axes (red). Estimated delays are shown for non-off-resonance (upper) and off-resonance (lower) correction approach.

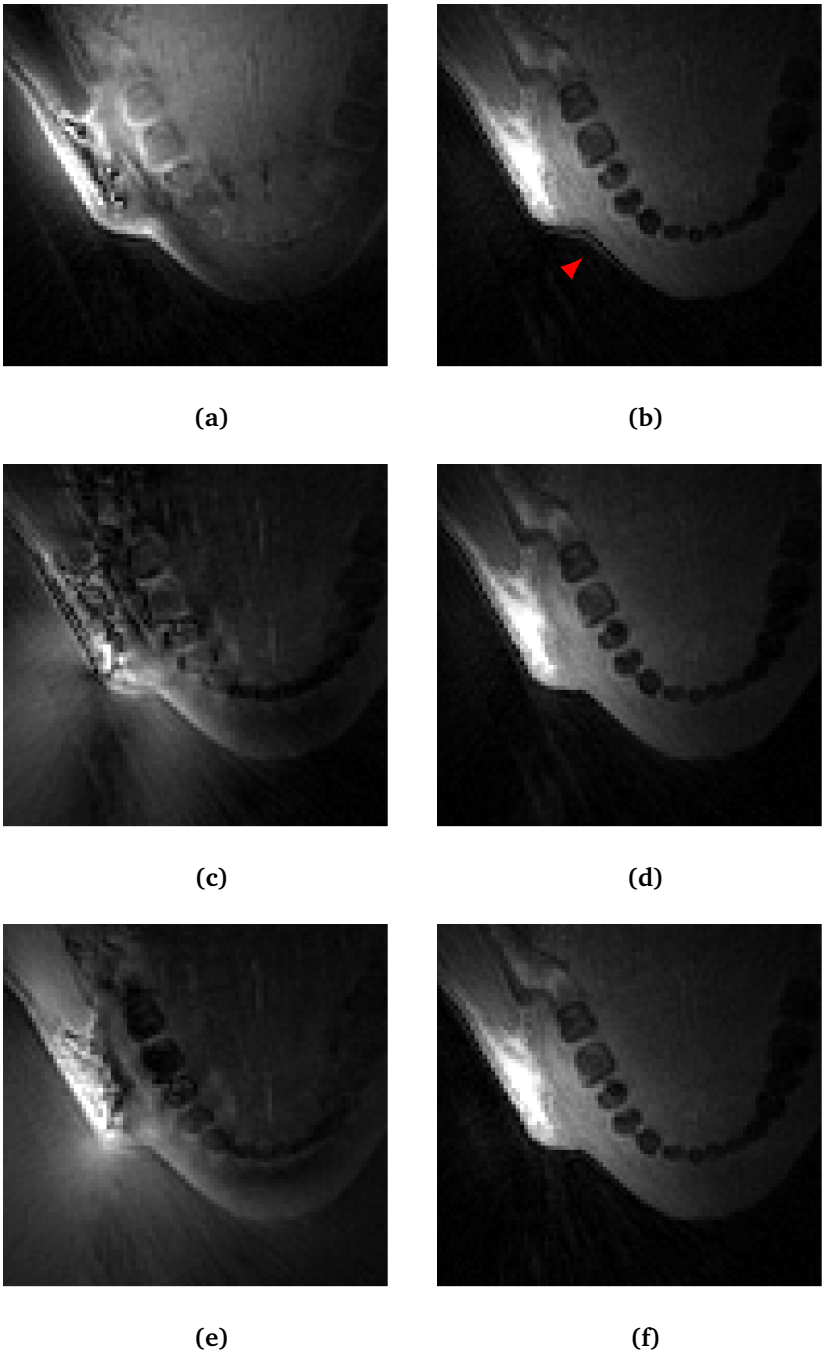

(a) **(b)**

(c) **(d)**

(e) **(f)**

Figure 72.: Reconstructed images corrected by (a) no gradient delay, (b) mean gradient delay of all profiles, ((c), (e)) non-off-resonance, and ((d), (f)) off-resonance corrected delays for ((e), (f)) every single profile and for ((d), (c)) tri-linear interpolation. The reconstructed images using no correction of the system delay (a) or using non-off-resonance corrected delays ((c), (e)) suffer from severe image degradation.

6.3. CAPRI for Identification of Caries Lesions

Ultra-short echo time (UTE) imaging has proven its potential for radiation free detection of caries lesions and also for classification of lesion progression using ultra-short T2* mapping. The UTE imaging sequence is very sensitive to gradient delay related k-space center shifts and off-resonance effects. CAPRI allows automatic correction of gradient delays, reduces off-resonance and T_2^* induced blurring artefacts and provides T_2^* mapping for lesion classification. In this section the performance of CAPRI for visualization of caries lesions is investigated.

Five volunteers underwent a MRI examination including a conventional UTE ($f_{CAPRI} = 0$) sequence and three CAPRI sequences with different CAPRI factors. For the reference UTE scan the slope duration was chosen to be double the minimal echo time and the acquisition duration was chosen in such way, that the T_2^* for dentin is half of it: $T_{ACQ,min} \approx 2T^*_{2,dentin}$. This results in a gradient slewrate of $150mT/ms$, a readout gradient strength of $21mT/m$, and a slope factor of $f_{slope} = {}^{T_{slope}}/_{T_{ACQ}} = 0.22$.

Detailed sequence parameters are listed in table 4. CAPRI factors where chosen to $f_{CAPRI} = 0/0.33/0.5/1$. As mentioned before the CAPRI factor (f_{CAPRI}) describes the relative position of k-space center on the gradient slope (e.g. $f_{CAPRI} = 0$: UTE; $f_{CAPRI} = 1$:end of slope) and defines the duration of the prephasing gradient in readout direction and therefore the minimum TE of the sequence. The respective echo times for the applied CAPRI factors result to TE $\approx 70/110/170/340\mu s$. The different CAPRI factors also change the overall acquisition durations according to equation 6.6, which result in $T_{ACQ} \approx 630/590/580/560$. In all cases a mono-exponential decay eddy current response was applied for correction of the trajectory shape. The automatic gradient delay correction algorithm was applied once for every volunteer on the data with a CAPRI factor of $f_{CAPRI} = 1$ and the resulting delays for the three main gradient axes were used for the reconstruction of the images with all

Table 4.: Sequence parameters for the MRI measurements.

	CAPRI			
Technique	spoiled FID			
CAPRI Factor	0	0.3	0.5	1
k-space Encoding	3D radial			
Excitation	non-selective			
Flip Angle [°]	10			
Echo Time [μs]	70	110	170	340
Repetition Time [ms]	4			
Resolution [mm^3]	1			
Field of View [mm^3]	200			
Scan Time [min]	9			

four CAPRI factors. The overall duration of the examination was about 40min for each volunteer.

Data analysis was done in the same manner than for the clinical studies insection 5.3. Caries lesions were identified as areas showing a signal enhancement of more than two times the standard deviation of the surrounding dentin. Maximal width, height, and depth were quantified for all sequences. Additionally the contrast-to-noise values were determined by calculating the ratio of the difference between the mean intensities of the lesion and the surrounding tissue (dentin), and the standard deviation of the dentin:

$$CNR = (C_{lesion} - C_{dentin})/\sigma_{dentin}.$$

In total, the volunteers showed 9 caries lesions. Figures 73 and 74 respective show a comparision for transversal and para-sagittal reformatted MR images with different CAPRI factors. Figure 73 shows also a comparision of the reformatted 3D MRI sequences with the related bitewing x-ray. All lesions could be clearly identified in all images with different f_{CAPRI}.

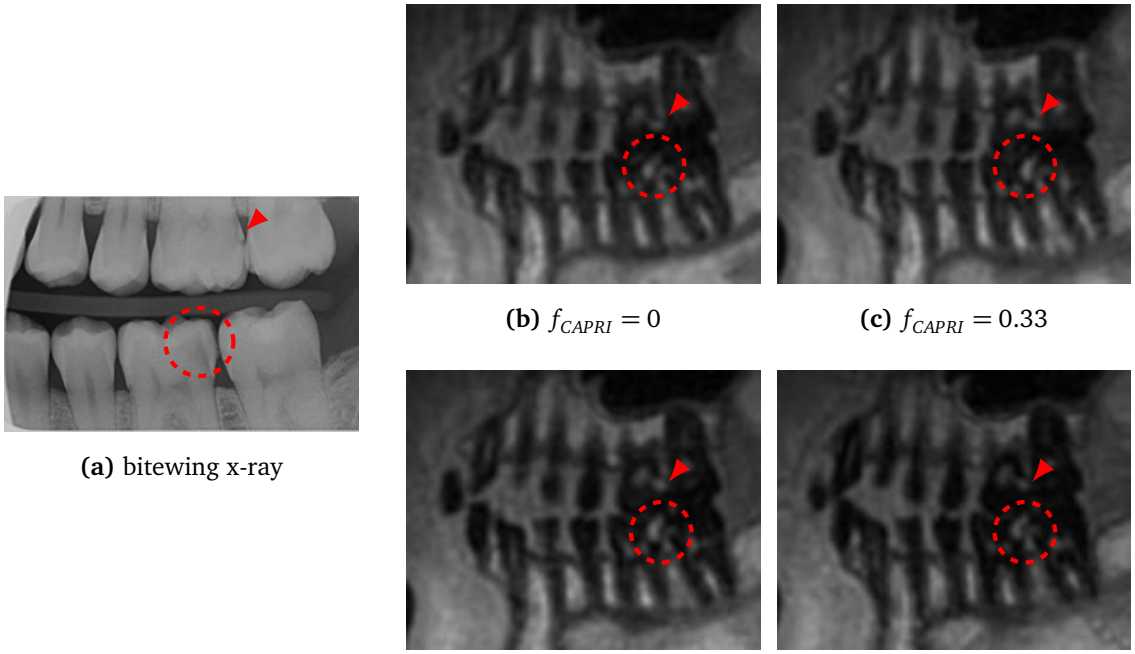

(a) bitewing x-ray

(b) $f_{CAPRI} = 0$

(c) $f_{CAPRI} = 0.33$

(d) $f_{CAPRI} = 0.5$

(e) $f_{CAPRI} = 1$

Figure 73.: Representation of a CII caries lesion in MR images with different CAPRI factors compared to the clinical x-ray bitewing.

The summarized results for the measured lesion extension and the contrast behaviour are given in table 5. No significant differences in lesion extension were observed between the different CAPRI factors. This is related to only slightly differences in the FWHM of the PSF (sec. 6.1.1) for the given parameters of less than 0.1 pixel. However, the delineation of

Table 5.: Lesion extend and contrast-to-noise ratio (CNR) for caries lesions in imaging sequences with different CAPRI factors

f_{CAPRI}	CNR	$w[mm]$	$h[mm]$	$d[mm]$
0	7.6 ± 2.8	3.4 ± 1.2	2.6 ± 0.6	2.7 ± 1.1
0.3	7.0 ± 2.7	3.4 ± 1.3	2.6 ± 0.6	2.6 ± 1.0
0.5	8.0 ± 3.0	3.0 ± 1.1	2.6 ± 0.5	2.6 ± 1.0
1	10.3 ± 4.3	3.2 ± 1.1	2.4 ± 0.6	2.6 ± 1.1

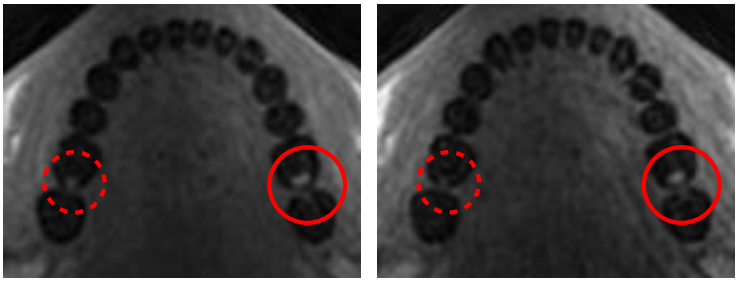

(a) $f_{CAPRI} = 0$ **(b)** $f_{CAPRI} = 0.3$

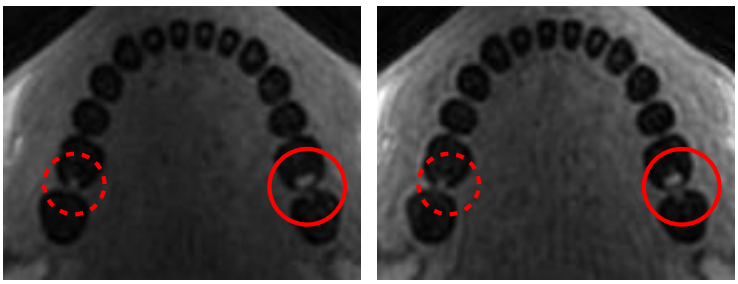

(c) $f_{CAPRI} = 0.5$ **(d)** $f_{CAPRI} = 1$

Figure 74.: Approximal caries lesions for different CAPRI factors.

small lesions improved for higher CAPRI factors (fig. 74). This observation was supported by the improved contrast between lesion and dentin with increasing f_{CAPRI}. The slightly increased contrast may be attributed on the one hand to the longer echo time which leads to higher signal decay for the surrounding dentin but on the other hand to the PSF amplitude function which provides higher differences in signal amplitude for higher CAPRI factors between ultra-short T_2^* values (sec. 6.1.1).

Although there is virtual no gain in resolution using pure flattop sampling instead of standard half-trapezodial sampling for the applied ramp acquisition fraction f_{slope}, the possibility of automatic phase correction, improved contrast and the lower sensitivity to off-resonances makes CAPRI an attractive alternative to other ultra-short echo time techniques.

6.4. Discussion

Ultra-short echo time (UTE) imaging has proven its potential for radiation free detection of caries lesions and also for classification of lesion progression using an ultra-short T_2^* mapping approach. A drawback of the UTE imaging sequence is the high sensitivity to gradient delay related k-space center shifts, to off-resonance effects, and to the prolonged sampling duration related to the reduced collection of k-space during ramp-up of the read-out gradient. The CAPRI sequence uses a small prephasing gradient to shift the k-space center along the rising slope towards the constant part of the gradient and enables a higher step size in the center of k-space using an unchanged sampling time interval. The position of k-space center related to the ramp duration shift is defined by the CAPRI factor (f_{CAPRI}). The system response which was developed for the UTE sequence to calculate the physical trajectory, is robust enough to fulfil the requirements of the CAPRI sequence for the different CAPRI factors. The faster sampling of the k-space center leads to a faster sampling of a single k-space profile and therefore reduces the impact of T_2^* decay and the accumulation of off-resonance related phase errors during data acquisition.

It has been shown that for pure ramp sampling the shift of k-space center reduces the broadening of the PSF and therefore the related image blur caused by the rapid signal decay from tissues with ultra-short T_2^* and also reduces phase accumulation from off-resonant tissues. While the improvement of the PSF shape related to T_2^* decay is mainly attributed to the reduction of acquisition duration, the reduction of the PSF width caused by off-resonance effects depends on the time reduction as well as on the mostly linear phase accumulation during flattop sampling in CAPRI imaging.

In a realistic sampling scenario of an UTE sequence – where high slewrates are chosen to keep the ramp time as short as possible and a high gradient strength is applied to ensure fast sampling during constant gradient part – the advantage of partial ramp sampling

strongly depends on the ratio between ramp portion and constant part of the gradient. For sequences were the ramp ratio is dominant (eg. low resolution images) the overall acquisition duration for a single k-space profile can be reduced by a high amount. If the ramp duration remains a quarter or less of the sampling duration the effect of time saving, supported by the CAPRI approach, is neglible even in case of tissue were the T_2^* values represents only an eighth of the acquisition duration. In case of phase induced image blur the effect of partial ramp sampling is only considerable for CAPRI factors above $f_{CAPRI} = 0.5$. In case of image blurring based on phase differences between water and fat the effect of CAPRI at the used 3T system could only be observed for very long ramp and sampling duration which is commonly not used in UTE imaging. The effect of partial ramp sampling in the presence of phase errors due to zero order off-resonances becomes more important when operating at higher field strength. The gain in signal intensity with increasing CAPRI factor – assuming the same time for k-space center sampling – is related to the reduced signal decay between adjacent k-space coordinates when sampling at higher gradient strength.

While the basic CAPRI sequence uses only the dead time of the system for the shift of the k-space center and ensures same echo time settings for UTE and CAPRI sequences, a slight modification of the sequence timing enables an automatic correction of system depended gradient delays. Since gradient delays affects the entire k-space trajectory but not the waveform, it is directly related to the shift of the echo peak in k-space.

It was found by Takizawa et al. [44] that the gradient delay varies with the gradient amplitude. He assumed that the variations are related to some un-corrected eddy currents with ultra-short time constants which can be approximately described as a delay [3]. Atkinson et al. [1] also describe a discrepancy between measured system delay and apparent system delay which he could compensate for by using an eddy current correction approach with five correction terms for both linear and zero-order eddy currents. In this thesis the

change of the apparent system delay with varying settings of the readout gradient could be approved, but could not be assigned to a related variation of eddy currents. It was found that the gradient delays vary with the gradient settings but the gradient waveform behaviour stays the same. A variation of the eddy current constants with changing gradient amplitude would lead to a non-linear scaling of the trajectory and a waveform compensation with a unique time constant eddy current model for all gradient settings would not be possible. The fact that only the gradient delay and not the waveform is affected, leads to the assumption that the differences of the gradient delay for several gradient settings are related to a varying mismatch in the timing between gradient and acquisitions due to the change in acquisition parameters. Takizawa as well as Atkinson support the findings of this thesis, that the gradient delays differ between the three main gradient axes. Takizawa [44] and Krämer [29] correct for this time dependency by using a reference prescan with identical imaging parameters as the imaging sequence. Takizawa calculates the signal delay by using a full echo calibration data set for each physical gradient axis and adapts the echo peak of the investigated UTE sequence by correlation of the the two raw data signals. In the presence of linear off-resonances the impact on the k-space trajectory of the ramp sampled UTE sequence is more prominent as for projection flattop sampling. This could lead to a deviation of the estimated gradient delay from the effective gradient delay. Krämer also uses a prephasing gradient as proposed in this thesis to produce an echo top during acquisition. Instead of using the echo peak of the raw data profiles the zero crossing of signal phase is used to estimate the gradient delay. The gradient delay is estimated by approximation of the position where the phase signal of all profiles build a phase node. Krämer did not investigate if the calculation of the mean echo top position highly varies from the findings of the phase-based approach. Also the presence of linear or zero order off-resonances is not examined. Since only a single gradient delay is estimated his method may fail for systems with different timings of the gradient amplifiers for the physical gradient axes.

In this thesis a correction scheme is proposed that facilitates a direct measurement of the echo peak along an arbitrary axis by starting the data acquisition in front of the k-space center. Since the automatic delay correction approach is applied to the same k-space data as used for image reconstruction, possible uncorrected ultra-short eddy current time constants can be treated as fixed system delays. Another factor which leads to a shift of the echo top is the presence of linear off-resonances. In contrast to an eddy current induced echo peak shift, linear off-resonances shift the echo peak in opposite direction for opposite readout gradient amplitudes. The presented method adjusts for off-resonance induced echo peak shifts by compensation of the delays from k-space profiles received with opposed gradient amplitudes. In case of non-equidistant k-space sampling, the presence of linear off-resonances leads to a change in k-space trajectory that does not behave like a linear echo peak shift. It was shown that for CAPRI factors of $f_{CAPRI} = 0.5$ or even higher the gradient delay in the presence off-resonances up to $0.5mT/ms$ anyhow can be estimated by calculating the mean delay of the opposed profiles. Even in case of $f_{CAPRI} = 0.25$ most of the delay calculations ensure sufficient image quality using the mean gradient delay.

The delay calculation for every individual k-space profile is very time consuming in the case of three-dimensional kooshball sampling. The time saving determination of the gradient delay of the three main gradient axes and tri-linear combination of these delays for trajectory calculation ensures comparable image quality. The high similarity between the results of both delay calculation methods indicates that cross term eddy currents are neglible and that the calculation of the mean gradient delays composed of system delay and short term eddy currents of the three physical gradient axes is sufficient.

A slight increase in echo time is inevitable for automatic delay correction, but can be controlled by a proper combination of slewrate, gradient amplitude and CAPRI factor.

It can be concluded that the CAPRI sequence allows automatic correction of gradient delays, enables the reduction of off-resonance and T_2^* induced blurring artefacts depended

on the ratio between ramp time and acquisition duration and provides T_2^* mapping for lesion classification.

In a first feasibility study – including five volunteers – the introduced CAPRI sequence has proven its ability for evaluation of caries lesions. For the given ratio between ramp time and acquisition duration of the investigated imaging sequences, there is virtually no gain in image resolution due to T_2^* decay or off-resonance effects for higher CAPRI factors. This supports the findings of the lesion dimensions in the different images, where no change of lesion extend could be observed for increasing CAPRI factor. The observed slight increase in contrast between lesion and surrounding tissue with increasing CAPRI factor my be attributed to the increase in echo time. Since the surrounding tissues are particular represented by dentin and enamel – which have much shorter T_2^* values than the observed caries lesion – the difference in signal magnitude between lesion and surrounding tissue changes with increasing echo time. Therefore the increase in contrast may not necessarily be directly related to the CAPRI technique. Images with higher CAPRI factor show a better delineation between the hard tissues – enamel and dentin – and soft tissue – the root – of the teeth. This reduction in image blur can not clearly be attributed to a reduced T_2^* decay, a reduced phase accumulation due to off-resonances or the dedicated delay calculation but indicates an improved sequence performance caused by the combination of the different features of the CAPRI sequence.

The deviations of the calculated delays in dental applications of up to $15\mu s$ from the estimated k-space center and an absolute difference of $25\mu s$ are caused by the high amount of susceptibility interfaces. The interface between mineralized teeth and soft muscle tissues interact like linear off-resonances and shift the k-space center for opposite profiles in opposite directions. In case of delay correction for every single k-space profile this effect could be clearly seen between the first part of the kooshball interleave (positive hemisphere – positive shift) and the second half of the kooshball interleave (negative hemisphere – negative

shift). It has been shown that the calculation of the delay from opposite profiles reliably corrects for this off-resonance behaviour. The high deviations from the estimated k-space center demand for a large k-space interval in front of k-space center. For the desired application in the field of dental MRI it seems not to be a challenge using a high CAPRI factor and measure at echo times in the range of 120μs - 340μs. For tissues with much shorter T_2^* values the use of echo times of this order may not be applicable for the imaging method, but the presented correction scheme can be applied using a CAPRI prescan to determine the gradient delays for image reconstruction. It was shown that the developed gradient waveform model for trajectory calculation fullfill the requirements for all CAPRI factors and therefore the gradient delay should stay the same for all CAPRI factors. This presumption has been proven in the dental application section, where the delay was only calculated once for the highest CAPRI factors and used for image reconstruction of the data acquired with different CARPI factors.

The results confirm the ability of CAPRI for the application of caries imaging without substantially affecting the lesion size and signal intensity. The possibility of automatic delay correction makes CAPRI an attractive alternative to other ultra-short echo time techniques in the field of dental MRI.

The CAPRI sequence can be further improved by shifting the start of the prephasing gradient prior to the RF excitation. The ramp-down of the gradient starts immediately after the end of the RF pulse is reached. The improved timing of the prephasing gradient will reduce the duration of the prephasing gradient after signal excitation by about 30% leaving all other sequence parameters including CAPRI factor unchanged. As in ZTE imaging the presence of the imaging gradient during RF excitation requires a high bandwidth of the RF pulse to ensure a uniform excitation of the investigated object. Since the 3D UTE imaging approach commonly uses a block pulse for signal excitation there is no need for adoption of the RF parameters.

7. Conclusion

The clinical application of MRI in the field of dentistry is up to now limited to tumors and displacement of the tempo-mandibular disc because of the restricted delineation of the mineralized tissues of the teeth. Due to their fast signal decay and related limited signal-to-noise ratio conventional MR imaging techniques are not able to assess those tissues. This thesis investigated the application of dedicated imaging sequences for tissues with fast signal decay for the visualization and quantification of initial demineralization and caries lesions. As imaging sequence an ultra-short echo time (UTE) method was chosen to visualize caries lesions directly and asses the penetration depth of the caries lesion into the mineralized tissues. The UTE sequence uses a center-out sampling scheme to acquire the MRI raw data and starts sampling during ramp-up of the readout gradient to minimize the signal decay between signal excitation and acquisition.

To ensure sufficient image quality accurate knowledge of the system performance is mandatory to rebuild the waveform and timing of the gradient amplifier output. To obtain the real trajectory a commonly used trajectory mapping approach was implemented. The exact gradient waveform was retrieved by using multiple measurements with opposed gradient amplitude and RF frequency offset to minimize the residual deviation of the obtained trajectory due to the effect of center frequency mismatch and global linear off-resonances. To model the real gradient amplifier output for image reconstruction a dedicated system impulse response with a single time constant was developed and applied to the ideal gra-

dient output for emulation of the smoothed edges at the beginning and end of the rising slope. The improvement of the gradient waveform and of the related k-space trajectory ensure reliable image quality. System imperfection like channel delay varies with the timing of the sequence and therefore have to be adjusted manually for each new set of imaging parameters which leads to a change in the waveform of the encoding gradient.

In a feasibility study with 12 patients the applicability of UTE for caries lesion detection was investigated and compared to a conventional MRI spin-echo (SE) sequence and to a planar bite-wing radiography which is used as nowadays gold standard for clinical caries detection. The three-dimensional imaging technique UTE clearly outperforms the clinical standard MRI SE sequence and its sensitivity resulted at least similar to the two-dimensional x-ray images. The UTE technique appears especially advantageous in cases where the x-ray is limited by structures superimposed along the unresolved third dimension. While x-ray provides an accurate delineation of the different mineralized layers of the teeth, UTE provides a high contrast between the mineralized tissues and the pulp, but facilitates only a weak delineation of the mineralized structures in the in-vivo images due to relative low SNR values. Significant differences in lesion extend and minimal distance to the pulp were observed for the different image modalities. Differences in lesion extend between UTE and x-ray were not significant but showed a trend to larger areal extent in UTE. These findings were supported by the in-vivo validation of randomly selected lesions where the underestimation of the lesion by x-ray was clearly proven. Therefore the use of conventional classification of caries progress – based on the depth of penetration of the lesion into the mineralized tissues – can not be transferred to dental MRI. A new classification to describe the lesion progress was introduced related to the visibility of the caries lesions in the different image modalities. To establish a lesion classification independent from x-ray imaging a quantitative analysis of the lesion was performed by mapping the T_2^* related signal decay over time and comparing of the results to the above obtained classification. It was proven

that the different caries classes obtained from visual comparison of the image modalities possess significantly different T_2^* relaxation times. All findings regarding lesions extension in the different image modalities and classification of caries lesions could be confirmed by the subsequently performed clinical study with 40 patients.

Conventional UTE imaging acquires the k-space center simultaneously with ramping-up of the readout gradient. The ramp sampling results in a slower collection of the k-space center which prolongs the overall sampling duration and makes the sequence very sensitive to gradient delays.

To further improve the image quality a new sequence – named CAPRI – was developed and introduced which enables k-space center-acquisition at partial ramp imaging. This CAPRI sequence shortens the sampling time at the gradient ramp by applying a small prephasing gradient to shift the k-space center along the rising slope. This leads to a faster sampling of the k-space center and therefore reduces the overall sampling duration of a k-space profile. This results in an improvement of image blur due to a reduction of T_2^* decay and a reduction of off-resonance related phase accumulation during acquisition.

The amount of k-space center shift is defined by the CAPRI factor (f_{CAPRI}) which describes the relative position of k-space center on the gradient slope and therefore determines the duration of the prephasing gradient and the related minimum echo time for the sequence. Using the minimal possible echo time for the shift of k-space center improves image quality without sacrificing signal intensity for short T_2^* components. Further image quality improvements can be realized by accepting some signal intensity reduction of the short T_2^* species and acquiring a partial echo by starting signal acquisition in front of the k-space center. This extreme asymmetric sampling approach allows direct measurement of the echo peak and therefore of the system delay. To correct for echo peak shift caused by linear off-resonances – which shifts the echo peak in opposite direction for opposite readout gradient amplitudes – the echo peak positions of opposed k-space profiles were used for delay

computation. Two different delay correction methods were investigated: determination of the gradient delay for every k-space raw data profile independently and determination of the gradient delay of the three main gradient axes with calculation of the trajectory by using a tri-linear interpolation of the delayed k-space profiles of the three gradient axes. It was shown that the time saving gradient delay correction method based on the tri-linear interpolation of the delays from the three main gradient axes ensures comparable image quality to the full correction method and is therefore the preferred approach.

To prove the concept of CAPRI for dental MRI five volunteers were included in a feasibility study. While the lesion dimensions resulted similar with the different techniques a slightly increased contrast was observed for increasing CAPRI factor. This may be attributed to the prolonged echo times for higher CAPRI factor and not necessarily be directly related to the CAPRI technique. It was shown that the automatic delay correction and the lower sensitivity to off-resonances makes CAPRI an attractive alternative to the UTE approach. For the chosen sequence parameters in dental MRI a CAPRI factor of $f_{CAPRI} = 0.5$ ensures reliable peak detection while leaving the echo time of the sequence as small as possible.

It could be shown that the UTE as well as the introduced CAPRI sequence are suitable in the area of dental MRI to examine the extend and progress of caries lesions.

In order to enable dental MRI for caries lesions to enter clinical routine it is imperative to further improve the imaging sequences as well as to develop dedicated hardware. Besides a reduction of the investment and the duration of the whole examination the patient comfort as well as the work-flow and planning of the scans have to be improved. The overall scan time of the sequence – and therefore the costs of the examination – may be reduced by using dedicated receive coils which improve the signal-to-noise ratio and further enable adjustment of the Field-of-View to the region of interest. Dedicated surface coils developed for dental purposes only, could also improve the positioning of the coil and facilitate the examination for the patient and the operating staff. The timing of the CAPRI sequence

could be further improved by starting the prephasing gradient in front of the excitation pulse and therefore shift the k-space center to higher gradient amplitude without a further manipulation of the echo time. This would also lead to an improvement of image quality due to the related reduction of sampling duration.

Ultra-short echo time imaging methods like UTE and CAPRI have the potential for an earlier diagnosis of initial caries lesions compared to the clinical standard x-ray, provide a more accurate assessment of the lesion dimension compared to the clinical standard x-ray imaging and may enable new applications such as monitoring of re-mineralization therapy. Additionally they provide a quantitative analyses of caries progress using a T_2^* characterisation of the lesions.

8. Bibliography

[1] ATKINSON, I. C., LU, A., AND THULBORN, K. R. Characterization and Correction of System Delays and Eddy Currents for MR Imaging with Ultrashort Echo-Time and Time-Varying Gradients. *Magnetic Resonance in Medicine 62*, 2 (Aug. 2009), 532–537.

[2] BALCOM, B. J., MACGREGOR, R. D., BEYEA, S. D., GREEN, D. P., ARMSTRONG, R. L., AND BREMNER, T. W. Single-Point Ramped Imaging with T1 Enhancement (SPRITE). *Journal of Magnetic Resonance. Series A 123*, 1 (Nov. 1996), 131–134.

[3] BERNSTEIN, M. A., KING, K. F., AND ZHOU, X. J. *Handbook of MRI Pulse Sequences*. Elsevier Academic Press, 2004.

[4] BLOCH, F., HANSEN, W. W., AND PACKARD, M. The Nuclear Induction Experiment. *Physical Review 70*, 7-8 (Oct. 1946), 474–485.

[5] BOUJRAF, S., HOFMANN, C., ULRICI, J., HELL, E., HALLER, B., AND RASCHE, V. Microstructural assessment of dental tissues by quantitative MRI using ultra-short echo time (UTE): initial in-vitro evaluation. In *Proc. ISMRM;* (Honolulu Hawaii USA, 2009), p. 4517.

[6] BRACEWELL, R. N. *The Fourier Transform and Its Applications*. McGraw Hill, 2000.

[7] BRACHER, A.-K., HOFMANN, C., BORNSTEDT, A., BOUJRAF, S., HELL, E., ULRICI, J., SPAHR, A., HALLER, B., AND RASCHE, V. Feasibility of Ultra-Short Echo Time (UTE)

Magnetic Resonance Imaging for Identification of Carious Lesions. *Magnetic Resonance in Medicine 66*, 2 (Aug. 2011), 538–545.

[8] BRACHER, A.-K., HOFMANN, C., BORNSTEDT, A., HELL, E., JANKE, F., ULRICI, J., HALLER, B., GEIBEL, M.-A., AND RASCHE, V. Ultrashort echo time (UTE) MRI for the assessment of caries lesions. *Dento Maxillo Facial Radiology 42*, 6 (2013), 20120321.

[9] BRITTAIN, J. H., SHANKARANARAYANAN, A., RAMANAN, V., SHIMAKAWA, A., CUNNINGHAM, C. H., HINKS, S., FRANCIS, R., TURNER, R., JOHNSON, J. W., NAYAK, K. S., TAN, S., PAULY, J. M., AND BYDDER, G. M. Ultra-Short TE Imaging with Single-Digit (8μs) TE. In *Proc. ISMRM;* (Kyoto, Japan, 2004), p. 629.

[10] BRODSKY, E. K., SAMSONOV, A. A., AND BLOCK, W. F. Characterizing and Correcting Gradient Errors in Non-Cartesian Imaging: Are Gradient Errors Linear Time-Invariant (LTI)? *Magnetic Resonance in Medicine 62*, 6 (Dec. 2009), 1466–1476.

[11] BYDDER, G. M. The Agfa Mayneord lecture: MRI of short and ultrashort T2 and T2* components of tissues, fluids and materials using clinical systems. *The British Journal of Radiology 84*, 1008 (Dec. 2011), 1067–1082.

[12] CONOLLY, S., NISHIMURA, D., MACOVSKI, A., AND GLOVER, G. Variable-Rate Selective Excitation. *Journal of Magnetic Resonance 78*, 3 (July 1988), 440–458.

[13] DUYN, J. H., YANG, Y., FRANK, J. A., AND VAN DER VEEN, J. W. Simple Correction Method for k-Space Trajectory Deviations in MRI. *Journal of Magnetic Resonance 132*, 1 (May 1998), 150–153.

[14] FUNDUK, N., KYDON, D. W., SCHREINER, L. J., PEEMOELLER, H., MILJKOVIĆ, L., AND PINTAR, M. M. Composition and Relaxation of the Proton Magnetization of Human Enamel and Its Contribution to the Tooth NMR Image. *Magnetic Resonance in Medicine 1*, 1 (Mar. 1984), 66–75.

[15] GLOVER, G. H., PAULY, J. M., AND BRADSHAW, K. M. Boron-11 imaging with a Three-dimensional Reconstruction Method. *Journal of Magnetic Resonance Imaging 2*, 1 (1992), 47–52.

[16] GRAVINA, S., AND CORY, D. G. Sensitivity and Resolution of Constant-Time Imaging. *Journal of Magnetic Resonance, Series B 104*, 1 (1994), 53–61.

[17] GRODZKI, D. M., JAKOB, P. M., AND HEISMANN, B. Ultrashort Echo Time Imaging Using Pointwise Encoding Time Reduction With Radial Acquisition (PETRA). *Magnetic Resonance in Medicine 67*, 2 (Feb. 2012), 510–518.

[18] GYROTOOLS. *ReconFrame version 3.0.460*. GyroTools LLC, Zurich, Switzerland, 2014.

[19] HAACKE, E. M., BROWN, R. W., THOMPSON, M. R., AND VENKATESAN, R. *Magnetic Resonance Imaging: Physical Principles and Sequence Design*, 1st ed. John Wiley & Sons Ltd, June 1999.

[20] HENKELMAN, R. M. Measurement of signal intensities in the presence of noise in MR images. *Medical Physics 12*, 2 (Apr. 1985), 232–233.

[21] HOLMES, J. E., AND BYDDER, G. M. MR imaging with ultrashort TE (UTE) pulse sequences: Basic principles. *Radiography 11*, 3 (Aug. 2005), 163–174.

[22] HORCH, R. A., NYMAN, J. S., GOCHBERG, D. F., DORTCH, R. D., AND DOES, M. D. Characterization of 1H NMR Signal in Human Cortical Bone for Magnetic Resonance Imaging. *Magnetic Resonance in Medicine 64*, 3 (Sept. 2010), 680–687.

[23] HOROWITZ, P., AND HILL, W. *The Art of Electronics*, 2nd ed. Cambridge University Press, July 1989.

[24] IDIYATULLIN, D., CORUM, C., PARK, J.-Y., AND GARWOOD, M. Fast and quiet MRI using a swept radiofrequency. *Journal of Magnetic Resonance 181*, 2 (Aug. 2006), 342–349.

[25] INSKO, E. K., ELLIOTT, M. A., SCHOTLAND, J. C., AND LEIGH, J. S. Generalized Reciprocity. *Journal of Magnetic Resonance 131*, 1 (Mar. 1998), 111–117.

[26] JEHENSON, P., WESTPHAL, M., AND SCHUFF, N. Analytical Method for the Compensation of Eddy-Current Effects Induced by Pulsed Magnetic Field Gradients in NMR Systems. *Journal of Magnetic Resonance 90*, 2 (Nov. 1990), 264–278.

[27] KÖHNLEIN, C. *Rekonstruktion von unterabgetasteten MRI Datensätzen, akquiriert auf beliebeigen Abtastgittern*. Diplomarbeit an der Universität Ulm, 2010.

[28] KIDD, E. *Essentials of Dental Caries: The Disease and Its Management*, 3rd ed. Oxford University Press, May 2005.

[29] KRÄMER, M., HERMANN, K.-H., AND REICHENBACH, J. R. Robust estimation of true k-space center position for radial center-out trajectories. In *Proc. ISMRM;* (Utah, USA, 2013), p. 3785.

[30] LEVITT, M. H., FREEMAN, R., AND FRENKIEL, T. Broadband Heteronuclear Decoupling. *Journal of Magnetic Resonance 47*, 2 (Apr. 1982), 328–330.

[31] MADIO, D. P., AND LOWE, I. J. Ultra-Fast Imaging Using Low Flip Angles and FIDs. *Magnetic Resonance in Medicine 34*, 4 (Oct. 1995), 525–529.

[32] MATLAB. *version 7.10.0 (R2012b)*. The MathWorks Inc., Natick, Massachusetts, United States, 2012.

[33] PAULY, J. M., CONOLLY, S. M., NISHIMURA, D., AND MACOVSKI, A. Slice-selective Excitation for Very Short T2 Species. In *Proc. SMRM;* (Amsterdam, The Netherlands, 1989), p. 28.

[34] PRUESSMANN, K. P., WEIGER, M., SCHEIDEGGER, M. B., AND BOESIGER, P. SENSE: sensitivity encoding for fast MRI. *Magnetic Resonance in Medicine 42*, 5 (Nov. 1999), 952–962.

[35] PURCELL, E. M., POUND, R. V., AND BLOEMBERGEN, N. Nuclear Magnetic Resonance Absorption in Hydrogen Gas. *Physical Review 70*, 11-12 (Dec. 1946), 986–987.

[36] PURCELL, E. M., TORREY, H. C., AND POUND, R. V. Resonance Absorption by Nuclear Magnetic Moments in a Solid. *Physical Review 69*, 1-2 (Jan. 1946), 37–38.

[37] RAHMER, J., BÖRNERT, P., GROEN, J., AND BOS, C. Three-Dimensional Radial Ultrashort Echo-Time Imaging with T2 Adapted Sampling. *Magnetic Resonance in Medicine 55*, 5 (May 2006), 1075–1082.

[38] RASCHE, V., HOLZ, D., AND PROKSA, R. MR Fluoroscopy Using Projection Reconstruction Multi-Gradient-Echo (prMGE) MRI. *Magnetic Resonance in Medicine 42*, 2 (Aug. 1999), 324–334.

[39] RASCHE, V., PROKSA, R., SINKUS, R., BÖRNERT, P., AND EGGERS, H. Resampling of Data Between Arbitrary Grids Using Convolution Interpolation. *IEEE Transactions on Medical Imaging 18*, 5 (May 1999), 385–392.

[40] RINCK, P. A. *Magnetic Resonance in Medicine: The Basic Textbook of the European Magnetic Resonance Forum*, 3rd ed. Blackwell Scientific Publications, 1993.

[41] ROBSON, M. D., GATEHOUSE, P. D., BYDDER, M., AND BYDDER, G. M. Magnetic Resonance: An Introduction to Ultrashort TE (UTE) Imaging. *Journal of Computer Assisted Tomography 27*, 6 (Dec. 2003), 825–846.

[42] SCHREINER, L. J., CAMERON, I. G., FUNDUK, N., MILJKOVIĆ, L., PINTAR, M. M., AND KYDON, D. N. Proton NMR spin grouping and exchange in dentin. *Biophysical Journal 59*, 3 (Mar. 1991), 629–639.

[43] SUSSMAN, M. S., PAULY, J. M., AND WRIGHT, G. A. Design of Practical T2-Selective RF Excitation (TELEX) Pulses. *Magnetic Resonance in Medicine 40*, 6 (Dec. 1998), 890–899.

[44] TAKIZAWA, M., HANADA, H., OKA, K., TAKAHASHI, T., YAMAMOTO, E., AND FUJII, M. A Robust Ultrashort TE (UTE) Imaging Method With Corrected k-Space Trajectory by Using Parametric Multiple Function Model of Gradient Waveform. *IEEE Transactions on Medical Imaging 32*, 2 (Feb. 2013), 306–316.

[45] TEN CATE, R. *Oral Histology: Development, Structure and Function*, 5th ed. Mosby Inc., July 1998.

[46] TYLER, D. J., ROBSON, M. D., HENKELMAN, R. M., YOUNG, I. R., AND BYDDER, G. M. Magnetic Resonance Imaging With Ultrashort TE (UTE) PULSE Sequences: Technical Considerations. *Journal of Magnetic Resonance Imaging 25*, 2 (Feb. 2007), 279–289.

[47] WEBER, J. Fluctuation Dissipation Theorem. *Physical Review 101*, 6 (Mar. 1956), 1620–1626.

[48] WEIGER, M., PRUESSMANN, K. P., BRACHER, A.-K., KÖHLER, S., LEHMANN, V., WOLFRAM, U., HENNEL, F., AND RASCHE, V. High-resolution ZTE imaging of human teeth. *NMR in biomedicine 25*, 10 (Oct. 2012), 1144–1151.

[49] WEIGER, M., PRUESSMANN, K. P., AND HENNEL, F. MRI with Zero Echo Time: Hard Versus Sweep Pulse Excitation. *Magnetic Resonance in Medicine 66*, 2 (Aug. 2011), 379–389.

[50] WONG, S. T. S., AND ROOS, M. S. A Strategy for Sampling on a Sphere Applied to 3D Selective RF Pulse Design. *Magnetic Resonance in Medicine 32*, 6 (1994), 778–784.

[51] WU, Y., DAI, G., ACKERMAN, J. L., HROVAT, M. I., GLIMCHER, M. J., SNYDER, B. D., NAZARIAN, A., AND CHESLER, D. A. Water- and Fat-Suppressed Proton Projection MRI (WASPI) of Rat Femur Bone. *Magnetic Resonance in Medicine 57*, 3 (Mar. 2007), 554–567.

A. CAPRI PSF

Due to the 3D centrosymetric sampling scheme of the CAPRI sequence the filter function which describes the non-idealities during acquisition results also in a 3D centrosymetric function and the related PSF can be calculated by using the Hankel transformation (sec. 2.2.2):

$$PSF = 4\pi \int_0^{k_{max}} H_{filter}(k)\ \mathrm{sinc}(2\pi k)\, k^2\, \mathrm{d}k$$

A.1. PSF Related to T_2^* Relaxation During Acquisition

The filter function describing the T_2^* decay during acquisition is given by:

$$H_{T_2^*}(t) \quad = e^{-\left(\frac{|t|}{T_2^*}\right)},$$

and the related PSF can be calculated by using the Hankel transformation:

$$PSF \; = \; 4\pi \int_0^{k_{max}} H_{T_2^*}(k)\, \mathrm{sinc}(2\pi k)\, k^2 \, \mathrm{d}k.$$

A.1.1. Pure Flattop Sampling

$$k(t) \; = \; \frac{\gamma}{2\pi} G_{RO}\, t$$

$$t(k) \; = \; \frac{2\pi k}{\gamma G_{RO}}$$

$$k_{max} \; = \; \frac{\gamma G_{RO}}{2\pi}\, T_{ACQ}$$

Filter function for pure flattop sampling:

$$H_{T_2^*}(k) \; = \; e^{-\left(\frac{2\pi}{\gamma G_{RO} T_2^*} k\right)}$$

$$= \; e^{-\left(\frac{T_{ACQ}}{T_2^*} \frac{k}{k_{max}}\right)}$$

PSF for pure flattop gradient and infinite k-space sampling:

$$PSF_{T_2^*,flat,inf}(k) = 4\pi \int_0^\infty e^{-\left(\frac{T_{ACQ}}{T_2^*}\frac{k}{k_{max}}\right)} \operatorname{sinc}(2\pi kr)\, k^2\, \mathrm{d}k \tag{A.1}$$

$$= \frac{8\pi {k_{max}}^3 \left(\frac{T_2^*}{T_{ACQ}}\right)^3}{\left(\left(2\pi k_{max} r \frac{T_2^*}{T_{ACQ}}\right)^2 + 1\right)^2}$$

Amplitude for pure flattop gradient and infinite k-space sampling:

$$PSF_{T_2^*,flat,inf}(0) = 4\pi \int_0^\infty e^{-\left(\frac{T_{ACQ}}{T_2^*}\frac{k}{k_{max}}\right)} k^2\, \mathrm{d}k \tag{A.2}$$

$$= 8\pi {k_{max}}^3 \left(\frac{T_2^*}{T_{ACQ}}\right)^3$$

PSF for pure flattop gradient and finite k-space sampling:

$$PSF_{T_2^*,flat,k_{max}}(k) = 4\pi \int_0^{k_{max}} e^{-\left(\frac{T_{ACQ}}{T_2^*}\frac{k}{k_{max}}\right)} \operatorname{sinc}(2\pi k r)\, k^2\, \mathrm{d}k \tag{A.3}$$

$$= \frac{8k_{max}^3 \pi \left(\frac{T_2^*}{T_{ACQ}}\right)^3}{\left(\left(2\pi k_{max} r \frac{T_2^*}{T_{ACQ}}\right)^2 + 1\right)^2} \left(1 - e^{-\frac{T_{ACQ}}{T_2^*}} \right.$$

$$\left[\cos(2\pi k_{max} r) \right.$$

$$\left(\frac{1}{2}(2\pi k_{max} r)^2 \left(\frac{T_2^*}{T_{ACQ}}\right) + 1 + \left(\frac{T_{ACQ}}{T_2^*}\right) \right)$$

$$+ \sin(2\pi k_{max} r)$$

$$\left(\left(2\pi k_{max} r\right) \left(-\frac{1}{2}\left(\frac{T_2^*}{T_{ACQ}}\right) + \frac{1}{2} \right) \right.$$

$$\left. \left. \left. - \frac{1}{\left(2\pi k_{max} r\right)} \left(\frac{1}{2}\left(\frac{T_{ACQ}}{T_2^*}\right) + \frac{1}{2}\left(\frac{T_{ACQ}}{T_2^*}\right)^2 \right) \right) \right] \right)$$

Amplitude for pure flattop gradient and finite k-space sampling:

$$PSF_{T_2^*,flat,k_{max}}(0) = 4\pi \int_0^{k_{max}} e^{-\left(\frac{T_{ACQ}}{T_2^*}\frac{k}{k_{max}}\right)} k^2 \, \mathrm{d}k \tag{A.4}$$

$$= 8\pi {k_{max}}^3 \left(\frac{T_2^*}{T_{ACQ}}\right)^3 \left[1 - e^{-\frac{T_{ACQ}}{T_2^*}} \left(1 + \left(\frac{T_{ACQ}}{T_2^*}\right) + 0.5\left(\frac{T_{ACQ}}{T_2^*}\right)^2\right)\right]$$

A.1.2. Pure Ramp Sampling

$$
\begin{aligned}
T_{ACQ} &= T_{slope} \\
k(t) &= 0.5\frac{\gamma}{2\pi}\frac{G_{RO}}{T_{slope}}t^2 = 0.5\frac{\gamma}{2\pi}\frac{G_{RO}}{T_{ACQ}}t^2 \\
t(k) &= \sqrt{\frac{4\pi k}{\gamma G_{RO}}} \\
k_{max} &= 0.5\frac{\gamma G_{RO}}{2\pi}T_{ACQ}
\end{aligned}
$$

Filter function for pure ramp sampling:

$$
\begin{aligned}
H_{T_2^*}(k) &= e^{-\left(\sqrt{\frac{4\pi k}{\gamma G_{RO}}}\frac{1}{T_2^*}\right)} \\
&= e^{-\left(\frac{T_{ACQ}}{T_2^*}\sqrt{\frac{k}{k_{max}}}\right)}
\end{aligned}
$$

PSF for pure ramp gradient and infinite k-space sampling:

$$PSF_{T_2^*,ramp,inf}(k) = \int_0^\infty e^{-\left(\sqrt{\frac{|k|}{k_{max}}}\frac{T_{ACQ}}{T_2^*}\right)} \operatorname{sinc}(2\pi k r)\, k^2 \, \mathrm{d}k \tag{A.5}$$

$$= \frac{k_{max}^3 \left(\frac{T_{ACQ}}{T_2^*}\right).^3}{(64\pi^3\sqrt{\left(r k_{max}\right)^9})}$$

$$\left[-16\frac{T_2^*}{T_{ACQ}}\sqrt{k_{max} r}\ {}_1F_2\left(2; \frac{3}{4}, \frac{5}{4}; -\frac{{T_{ACQ}}^4}{64(2\pi k_{max} r)^2 T_2^{*4}}\right)\right.$$

$$+ \cos\left(\frac{{T_{ACQ}}^2}{8\pi k_{max} r T_2^{*2}}\right)\left(12\pi k_{max} r\left(\frac{T_2^*}{T_{ACQ}}\right)^2 + 1\right)$$

$$\left. + \sin\left(\frac{{T_{ACQ}}^2}{8\pi k_{max} r T_2^{*2}}\right)\left(12\pi k_{max} r\left(\frac{T_2^*}{T_{ACQ}}\right)^2 - 1\right)\right],$$

where the Hypergeometric function ${}_pF_q(a; b; z)$ is defined as:

$${}_pF_q(a; b; z) = \sum_{n=0}^{\infty} \frac{(a1)_n \ldots (a_p)_n}{(b1)_n \ldots (b_q)_n} \frac{z^n}{n!}.$$

Amplitude for pure ramp gradient and infinite k-space sampling:

$$PSF_{T_2^*,ramp,inf}(0) = \int_0^\infty e^{-\left(\sqrt{\frac{|k|}{k_{max}}}\frac{T_{ACQ}}{T_2^*}\right)} k^2 \, \mathrm{d}k \tag{A.6}$$

$$= 960\pi {k_{max}}^3 \left(\frac{T_2^*}{T_{ACQ}}\right)^6$$

PSF for pure ramp gradient and finite k-space sampling:

$$PSF_{T_2^*,ramp,trunc} = 4\pi \int_0^{k_{max}} e^{-\left(\frac{T_{ACQ}}{T_2^*}\sqrt{\frac{k}{k_{max}}}\right)} \operatorname{sinc}(2\pi k)\, k^2 \, \mathrm{d}k \tag{A.7}$$

$$= \frac{(1+\mathrm{i})\, e^{-\frac{iT_{ACQ}^2}{8k_{max}\pi r T_2^{*2}}} \cdot k_{max}^3}{128\pi^3\sqrt{\left(k_{max}r\right)^9}T_2^{*3}}$$

$$\left[T_{ACQ}\left(12\pi k_{max} r T_2^{*2} - iT_{ACQ}^2\right)\operatorname{erf}\left(\frac{(4+4i)\pi k_{max} r T_2^* + (1-i)T_{ACQ}}{4\sqrt{\pi k_{max} r}\, T_2^*}\right)\right.$$

$$- e^{-2ik_{max}\pi r - \frac{T_{ACQ}}{T_2^*}} \cdot e^{\frac{iT_{ACQ}^2}{8\pi k_{max} r T_2^{*2}}}$$

$$\left((2+2i)\sqrt{k_{max} r}\, T_2^* \left(-16i\left(1 + e^{4i\pi k_{max} r}\right) k_{max}^2 \pi^2 r^2 T_2^{*2} \right.\right.$$

$$\left. + 4(-1 + e^{4ik_{max}\pi r})\pi k_{max} r T_2^* (2T_2^* - T_{ACQ}) + i(1 + e^{4i\pi k_{max} r})T_{ACQ}^2 \right)$$

$$+ e^{2i\pi k_{max} r + \frac{T_{ACQ}}{T_2^*} + \frac{iT_{ACQ}^2}{8k_{max}\pi r T_2^{*2}}} T_{ACQ}(12\pi k_{max} r T_2^{*2} + iT_{ACQ}^2)$$

$$\left.\left. \operatorname{erfi}\left(\frac{(4+4i)\pi k_{max} r T_2^* - (1-i)T_{ACQ}}{4\sqrt{\pi k_{max} r}\, T_2^*}\right)\right)\right.$$

$$\left. - T_{ACQ}\left((4-4i) e^{\frac{iT_{ACQ}^2}{8\pi k_{max} r T_2^{*2}}} \sqrt{k_{max} r}\, T_2^* T_{ACQ} \right.\right.$$

$$+ e^{\frac{iT_{ACQ}^2}{4\pi k_{max} r T_2^{*2}}} \left(-12i\pi k_{max} r T_2^{*2} + T_{ACQ}^2\right) \mathrm{erf}\left(\frac{(1+\mathrm{i})\, T_{ACQ}}{4\sqrt{\pi k_{max} r}\, T_2^*}\right)$$

$$+ \left(-12ik_{max}\pi r T_2^{*2} - T_{ACQ}^2\right) \mathrm{erfi}\left(\frac{(1+\mathrm{i}) T_{ACQ}}{4\sqrt{\pi k_{max} r}\, T_2^*}\right)\Bigg)\Bigg]$$

Amplitude for pure ramp gradient and finite k-space sampling:

$$PSF_{T_2^*,ramp,trunc}(0) = \int_0^{k_{max}} e^{-\left(\sqrt{\frac{|k|}{k_{max}}} \frac{T_{ACQ}}{T_2^*}\right)} k^2 \,\mathrm{d}k \tag{A.8}$$

$$= 8\pi k_{max}^3 \left(\frac{T_2^*}{T_{ACQ}}\right)^6 \Bigg[120 - e^{-\frac{T_{ACQ}}{T_2^*}} \Bigg(120 + 120\frac{T_{ACQ}}{T_2^*} + 60\left(\frac{T_{ACQ}}{T_2^*}\right)^2$$

$$+ 20\left(\frac{T_{ACQ}}{T_2^*}\right)^3 + 5\left(\frac{T_{ACQ}}{T_2^*}\right)^4 + \left(\frac{T_{ACQ}}{T_2^*}\right)^5\Bigg)\Bigg]$$

A.2. PSF Related to Off-Center Frequency

The filter function describing the off-resonance induced phase accumulation during acquisition is given by

$$H_{\omega_{off}}(t) = e^{\mathrm{i}\omega_{off}|t|},$$

and the related PSF can be calculated by using the Hankel transformation:

$$PSF = 4\pi \int_0^{k_{max}} H_{\omega_{off}}(k)\,\mathrm{sinc}(2\pi k)\,k^2\,\mathrm{d}k.$$

A.2.1. Pure Flattop Sampling

$$k(t) = \frac{\gamma}{2\pi} G_{RO} t$$

$$t(k) = \frac{2\pi k}{\gamma G_{RO}}$$

$$k_{max} = \frac{\gamma G_{RO}}{2\pi} T_{ACQ}$$

Filter function for pure flattop sampling:

$$H_{\omega_{off}}(k) = e^{\mathrm{i}\left(\frac{2\pi\omega_{off}}{\gamma G_{RO}} k\right)}$$

$$= e^{\mathrm{i}\left(\omega_{off} T_{ACQ} \frac{k}{k_{max}}\right)}$$

PSF for pure flattop gradient and infinite k-space sampling:

$$PSF_{T_2^*,flat,inf}(k) = 4\pi \int_0^\infty e^{\mathrm{i}\left(\omega_{off} T_{ACQ} \frac{k}{k_{max}}\right)} \operatorname{sinc}(2\pi k r)\, k^2 \,\mathrm{d}k \tag{A.9}$$

$$= -\frac{\mathrm{i}8\pi {k_{max}}^3 \left(\frac{1}{T_{ACQ}\omega_{off}}\right)^3}{\left(-\left(2\pi k_{max} r \frac{1}{T_{ACQ}\omega_{off}}\right)^2 + 1\right)^2}$$

Amplitude for pure flattop gradient and infinite k-space sampling

$$PSF_{T_2^*,flat,inf}(0) = 4\pi \int_0^\infty e^{\mathrm{i}\left(\omega_{off} T_{ACQ} \frac{k}{k_{max}}\right)} k^2 \,\mathrm{d}k \tag{A.10}$$

$$= -\mathrm{i}8\pi {k_{max}}^3 \left(\frac{1}{T_{ACQ}\omega_{off}}\right)^3$$

PSF for pure flattop gradient and finite k-space sampling:

$$PSF_{\omega_{off},flat,k_{max}}(k) = 4\pi \int_0^{k_{max}} e^{\mathrm{i}\left(\omega_{off} T_2^* \frac{k}{k_{max}}\right)} \operatorname{sinc}(2\pi k r)\, k^2 \,\mathrm{d}k \tag{A.11}$$

$$= \frac{-\mathrm{i}8\pi k_{max}^3 \left(\frac{1}{T_{ACQ}\omega_{off}}\right)^3}{\left(-\left(2\pi k_{max} r \frac{1}{T_{ACQ}\omega_{off}}\right)^2 + 1\right)^2} \left(1 - e^{\mathrm{i}T_{ACQ}\omega_{off}} \right.$$

$$\left[\cos(2\pi k_{max} r) \right.$$

$$\left(\frac{\mathrm{i}}{1} \left(2\pi k_{max} r\right)^2 \left(\frac{1}{T_{ACQ}\omega_{off}} \right) + 1 - \frac{\mathrm{i}}{2} T_{ACQ}\omega_{off} \right)$$

$$+ \sin(2\pi k_{max} r)$$

$$\left(\left(2\pi k_{max} r\right) \left(-\frac{\mathrm{i}}{2} + \frac{\mathrm{i}}{2} \left(\frac{1}{T_{ACQ}\omega_{off}} \right) \right) \right.$$

$$\left. \left. \left. + \frac{1}{\left(2\pi k_{max} r\right)} \left(-\frac{\mathrm{i}}{2} T_{ACQ}\omega_{off} - \frac{1}{2} \left(T_{ACQ}\omega_{off} \right)^2 \right) \right) \right] \right)$$

Amplitude for pure flattop gradient and finite k-space sampling:

$$PSF_{\omega_{off},flat,k_{max}}(0) = 4\pi \int_0^{k_{max}} e^{\mathrm{i}\left(\omega_{off} T_{ACQ} \frac{k}{k_{max}}\right)} k^2 \,\mathrm{d}k \tag{A.12}$$

$$= -\mathrm{i}8\pi k_{max}^3 \left(\frac{1}{\omega_{off} T_{ACQ}}\right)^3$$

$$\left(1 - e^{\mathrm{i}\omega_{off} T_{ACQ}} \left(1 - \mathrm{i}\left(\omega_{off} T_{ACQ}\right) - 0.5 \cdot \left(\omega_{off} T_{ACQ}\right)^2\right)\right)$$

A.2.2. Pure Ramp Sampling

$$
\begin{aligned}
T_{ACQ} &= T_{slope} \\
k(t) &= 0.5\frac{\gamma}{2\pi}\frac{G_{RO}}{T_{slope}}t^2 = 0.5\frac{\gamma}{2\pi}\frac{G_{RO}}{T_{ACQ}}t^2 \\
t(k) &= \sqrt{\frac{4\pi k}{\gamma G_{RO}}} \\
k_{max} &= 0.5\frac{\gamma G_{RO}}{2\pi}\,T_{ACQ}
\end{aligned}
$$

Filter function for pure ramp sampling:

$$
\begin{aligned}
H_{T_2^*}(k) &= e^{\mathrm{i}\left(\omega_{off}\sqrt{\frac{4\pi T_{ACQ}k}{\gamma G_{RO}}}\right)} \\
&= e^{\mathrm{i}\left(\omega_{off}T_{ACQ}\sqrt{\frac{k}{k_{max}}}\right)}
\end{aligned}
$$

PSF for pure ramp gradient and infinite k-space sampling:

$$PSF_{\omega_{off},ramp,inf}(k) = \int_0^{\infty} e^{\mathrm{i}\left(\omega_{off} T_{ACQ}\sqrt{\frac{k}{k_{max}}}\right)} \operatorname{sinc}(2\pi k r)\, k^2 \,\mathrm{d}k \tag{A.13}$$

$$= \frac{k_{max}^3 \left(T_{ACQ}\omega_{off}\right).^3}{(64\pi^3\sqrt{\left(r k_{max}\right)^9})}$$

$$\left[16\frac{1}{T_{ACQ}\omega_{off}}\sqrt{k_{max} r}\ {}_1F_2\left(2; \frac{3}{4}, \frac{5}{4}; -\frac{\left(T_{ACQ}\omega_{off}\right)^4}{64(2\pi k_{max} r)^2}\right)\right.$$

$$- \mathrm{i}\cos\left(\frac{{T_{ACQ}\omega_{off}}^2}{8\pi k_{max} r}\right)\left(12\pi k_{max} r\left(\frac{1}{T_{ACQ}\omega_{off}}\right)^2 - 1\right)$$

$$\left. + \mathrm{i}\sin\left(\frac{{T_{ACQ}\omega_{off}}^2}{8\pi k_{max} r}\right)\left(12\pi k_{max} r\left(\frac{1}{T_{ACQ}\omega_{off}}\right)^2 + 1\right)\right]$$

where the Hypergeometric function ${}_pF_q(a; b; z)$ is defined as

$${}_pF_q(a; b; z) = \sum_{n=0}^{\infty} \frac{(a1)_n \ldots (a_p)_n}{(b1)_n \ldots (b_q)_n} \frac{z^n}{n!}$$

Amplitude for pure ramp gradient and infinite k-space sampling:

$$PSF_{T_2^*,ramp,inf}(0) = \int_0^\infty e^{\mathrm{i}\left(\omega_{off} T_{ACQ} \sqrt{\frac{k}{k_{max}}}\right)} k^2 \,\mathrm{d}k \tag{A.14}$$

$$= -960\pi {k_{max}}^3 \left(\frac{1}{T_{ACQ}\omega_{off}}\right)^6$$

PSF for pure ramp gradient and finite k-space sampling:

$$PSF_{\omega_{off},ramp,trunc} = 4\pi \int_0^{k_{max}} e^{\mathrm{i}\left(\omega_{off} T_{ACQ} \sqrt{\frac{k}{k_{max}}}\right)} \operatorname{sinc}(2\pi k)\, k^2 \,\mathrm{d}k \tag{A.15}$$

$$= \frac{k_{max}^3}{128\pi^3 \sqrt{\left(k_{max} r\right)^9}} e^{-\frac{\mathrm{i}\left(T_{ACQ}\omega_{off}\right)^2}{8k_{max}\pi r}}$$

$$\left(-(1+\mathrm{i})\, T_{ACQ}\omega_{off} \left[\left(-4+4\mathrm{i} \right) e^{\frac{\mathrm{i}\left(T_{ACQ}\omega_{off}\right)^2}{8k_{max}\pi r}} \sqrt{k_{max} r}\, T_{ACQ}\omega_{off} \right.\right.$$

$$+ \mathrm{i} e^{\frac{\mathrm{i}\left(T_{ACQ}\omega_{off}\right)^2}{4k_{max}\pi r}} \left(12\pi k_{max} r + \mathrm{i}\left(T_{ACQ}\omega_{off}\right)^2 \right) \operatorname{erf}\left(\frac{(1+\mathrm{i}) T_{ACQ}\omega_{off}}{4\sqrt{\pi k_{max} r}} \right)$$

$$\left.\left. + \left(\mathrm{i}12\pi k_{max} r + \left(T_{ACQ}\omega_{off}\right)^2 \right) \operatorname{erfi}\left(\frac{(1+\mathrm{i}) T_{ACQ}\omega_{off}}{4\sqrt{\pi k_{max} r}} \right) \right] \right.$$

$$+ e^{-\mathrm{i}2k_{max}\pi r}$$

$$\left[-4e^{\frac{\mathrm{i} T_{ACQ}\omega_{off}\left(8\pi k_{max} r + T_{ACQ}\omega_{off}\right)}{8k_{max}\pi r}} \sqrt{r k_{max}} \right.$$

$$\left(16\left(1 + e^{\mathrm{i}4\pi k_{max} r}\right)\left(k_{max}\pi r\right)^2 + \left(1 + e^{\mathrm{i}4\pi k_{max} r}\right)\left(T_{ACQ}\omega_{off}\right)^2 \right.$$

$$
\begin{aligned}
&\quad -4\left(-1+e^{\mathrm{i}4\pi k_{max}r}\right)k_{max}\pi r\left(-\mathrm{i}2+T_{ACQ}\omega_{off}\right)\Bigg)\\
&+(1+\mathrm{i})\,e^{\left(2\mathrm{i}k_{max}\pi r+\frac{\mathrm{i}\left(T_{ACQ}\omega_{off}\right)^2}{4\pi k_{max}r}\right)}\left(-12\mathrm{i}\pi k_{max}r+\left(T_{ACQ}\omega_{off}\right)^2\right)\\
&\quad T_{ACQ}\omega_{off}\,\mathrm{erf}\left(\frac{(1+\mathrm{i})\left(4k_{max}\pi r-T_{ACQ}\omega_{off}\right)}{4\sqrt{\pi k_{max}r}}\right)\\
&+(1+\mathrm{i})\,e^{\mathrm{i}2k_{max}\pi r}T_{ACQ}\omega_{off}\left(12\mathrm{i}\pi k_{max}r+\left(T_{ACQ}\omega_{off}\right)^2\right)\\
&\quad \mathrm{erfi}\left(\frac{(1+\mathrm{i})\left(4k_{max}\pi r+T_{ACQ}\omega_{off}\right)}{4\sqrt{\pi k_{max}r}}\right)\Bigg]\Bigg)
\end{aligned}
$$

Amplitude for pure ramp gradient and finite k-space sampling:

$$
\begin{aligned}
PSF_{T_2^*,ramp,trunc}(0) &= \int_0^{k_{max}} e^{\mathrm{i}\left(\omega_{off}T_{ACQ}\sqrt{\frac{k}{k_{max}}}\right)}k^2\,\mathrm{d}k \qquad \text{(A.16)}\\
&= 8\pi k_{max}^3\left(\frac{1}{T_{ACQ}\omega_{off}}\right)^6\\
&\quad\Bigg[-120-e^{\left(\mathrm{i}T_{ACQ}\omega_{off}\right)}\Bigg(-120+\mathrm{i}120T_{ACQ}\omega_{off}+60\left(T_{ACQ}\omega_{off}\right)^2\\
&\qquad -\mathrm{i}20\left(T_{ACQ}\omega_{off}\right)^3-5\left(T_{ACQ}\omega_{off}\right)^4+\mathrm{i}\left(T_{ACQ}\omega_{off}\right)^5\Bigg)\Bigg]
\end{aligned}
$$

Curriculum Vitae

Content from this page was removed due to privacy reasons.

Content from this page was removed due to privacy reasons.

List of Publications

Journal Publications

2015 Geibel MA, Schreiber ES, Bracher AK, Hell E, Ulrici J, Sailer LK, Ozpeynirci Y, Rasche V. Assessment of Apical Periodontitis by MRI: A Feasibility Study. Rofo. 2015 Apr;187(4):269-275

2013 Bracher AK, Hofmann C, Bornstedt A, Hell E, Janke F, Ulrici J, Haller B, Geibel MA, Rasche V. Ultrashort echo time (UTE) MRI for the assessment of caries lesions. DMFR. 2013 Jun; 42(6): 20120321.

2012: Weiger M, Pruessmann KP, Bracher AK, Köhler S, Lehmann V, Wolfram U, Hennel F, Rasche V. High-resolution ZTE imaging of human teeth. NMR Biomed. 2012 Oct;25(10):1144-51

2011: Bracher AK, Hofmann C, Bornstedt A, Boujraf S, Hell E, Ulrici J, Spahr A, Haller B, Rasche V. Feasibility of ultra-short echo time (UTE) magnetic resonance imaging for identification of carious lesions. Magn Reson Med. 2011 Aug;66(2):538-45

Conference Contributions

2014: Bracher AK, Hell E, Ulrici J, Rasche V. Contrast manipulating mixed kspace COMMIX CAPRI / UTE for ultra short T_2^* mapping using multiple echo times within a single k-space data set. In *Proc. ISMRM*, Milano, Italy, 2014: 3198

Bracher AK, Hell E, Ulrici J, Rasche V. Automatic gradient delay correction using center-acquisition-at-partial-ramp imaging (CAPRI). In *Proc. ISMRM*, Milano, Italy, 2014: 4865

Bracher AK, Rasche V,Hell E, Ulrici J, Bornstedt A. Scan time acceleration by using multi-contrast keyhole imaging (McK) for the identification of (acute) apical periodontitis. In *Proc. ISMRM*, Milano, Italy, 2014: 1268

Bracher AK, Hell E, Ulrici J, Rasche V. Center-acquisition-at-ramp imaging (CAPRI) compared to ultra-short echo-time (UTE) imaging for diagnosis of dental demineralization. In *Proc. ISMRM*, Milano, Italy, 2014: 2294

2012: Bracher AK, Kammer D, Hell E, Ulrici J, Rasche V. Center-acquisition-at-partial-ramp-imaging (CAPRI) for the reduction of off-resonance and T_2 induced blurring artifacts. In *Proc. ISMRM*, Melbourne, Australia, 2012: 2294

Schreiber ES, Bracher AK, Hell E, Ulrici J, Geibel MA, Sailer LK, Rasche V. Assessment of apical periodontitis by the size comparison between MRI and CT. In *Proc. ISMRM*, Melbourne, Australia, 2012: 1423

Kammer D, Bracher AK, Horneff A, Hell E, Ulrici J, Bornstedt A, Rasche V. Retrospective Gated MRI for High-Resolution Imaging of the TMJ Dynamics During Active Mastication. In *Proc. ISMRM*, Melbourne, Australia, 2012: 3334

2011: Bracher AK, Hofmann C, Bornstedt A, Hell E, Ulrici J, Haller B, Rasche V. Accurate In Vivo Assessment of Caries Lesion Extent by UTE MRI. In *Proc. ISMRM*, Montreal, Canada, 2011: 2611

Bracher AK, Mess M, Bornstedt A, Hell E, Ulrici J, Haller B, Rasche V. Assessment of Cortical Bone Resorption and Acute Inflammation in Parodontitis. In *Proc. ISMRM*, Montreal, Canada, 2011: 2609

Bracher AK, Bornstedt A, Hell E, Ulrici J, Sailer LK, Rasche V. Assessment of Bone Degradation and Acute Inflammation in Apical Parodontitis. In *Proc. ISMRM*, Montreal, Canada, 2011: 2613

Bracher AK, Bornstedt A, Hell E, Ulrici J, Volker Rasche V. In Vivo and In Vitro T_2^* Quantification of Carious Lesions by Ultra-Short Echo-Time (UTE) MRI. In *Proc. ISMRM*, Montreal, Canada, 2011: 4507

Weiger M, Pruessmann KP, Bracher AK, Köhler S, Lehmann V, Wolfram U, Rasche V. High-Resolution ZTE Imaging of Human Teeth. In *Proc. ISMRM*, Montreal, Canada, 2011: 2612

Bracher AK, Hoffmann C, Ulrici J, Hell E, Haller B, Rasche V. Dentale Diagnostik mittels Magnetresonanztomographie: Identifizierung und dreidimensionale Darstellung kariöser Läsionen. Spitzenforschung in der Zahnheilkunde. Innovationen und Auszeichnungen 2011:30-40

Bracher AK, Hofmann CP, Ulrici J, Hell E, Haller B, Rasche V. MRI for the assessment of acute parodontitis. Int J CARS, 2011:6 (Suppl 1):S225

Bracher AK, Hofmann CP, Ulrici J, Hell E, Haller B, Rasche V. In-vivo assessment of carious lesions by MRI. Int J CARS, 2011:6 (Suppl 1):S223

2010: Bracher AK, Hoffmann C, Boujraf S, Bornstedt A, Hell E, Ulrici J, Spahr A, Rasche V. Ultrashort Echo-Time (UTE) Imaging for Early Diagnosis of Dental Demineralization. In *Proc. ISMRM*, Montreal, Canada, 2010: 2974